



**UNIVERSIDADE ESTADUAL DE CAMPINAS**  
**Faculdade de Engenharia Mecânica**

Luiz Henrique Martinez Antunes

**Efeito do tratamento térmico na  
transformação de fase  $\gamma - \epsilon$  da liga Co-28Cr-  
6Mo produzida por fusão seletiva a laser**

CAMPINAS  
2023

LUIZ HENRIQUE MARTINEZ ANTUNES

# **Efeito do tratamento térmico na transformação de fase $\gamma - \epsilon$ da liga Co-28Cr-6Mo produzida por fusão seletiva a laser**

Tese apresentada à Faculdade de Engenharia Mecânica da Universidade Estadual de Campinas como parte dos requisitos exigidos para obtenção do título de Doutor em Engenharia Mecânica, na Área de Materiais e Processos de Fabricação.

Orientadora: Profa. Dra. Paula Fernanda da Silva Farina

Coorientador: Prof. Dr. Miloslav Béréš

ESTE TRABALHO CORRESPONDE À VERSÃO FINAL DA TESE DEFENDIDA PELO ALUNO LUIZ HENRIQUE MARTINEZ ANTUNES, E ORIENTADA PELA PROFA. DRA PAULA FERNANDA DA SILVA FARINA

CAMPINAS  
2023

Ficha catalográfica  
Universidade Estadual de Campinas  
Biblioteca da Área de Engenharia e Arquitetura  
Rose Meire da Silva - CRB 8/5974

An89e Antunes, Luiz Henrique Martinez, 1986-  
Efeito do tratamento térmico na transformação de fase  $\gamma - \epsilon$  da liga  
Co-28Cr-6Mo produzida por fusão seletiva a laser / Luiz Henrique Martinez  
Antunes. – Campinas, SP : [s.n.], 2023.

Orientador: Paula Fernanda da Silva Farina.

Coorientador: Miloslav Béreš.

Tese (doutorado) – Universidade Estadual de Campinas, Faculdade de  
Engenharia Mecânica.

1. Manufatura aditiva. 2. Cobalto, Ligas de. 3. Caracterização de materiais.  
4. Transformações de fase. I. Farina, Paula Fernanda da Silva, 1978-. II. Béreš,  
Miloslav. III. Universidade Estadual de Campinas. Faculdade de Engenharia  
Mecânica. IV. Título.

#### Informações Complementares

**Título em outro idioma:** Effect of heat treatment on the  $\gamma - \epsilon$  phase transformation of the  
Co-28Cr-6Mo alloy produced by selective laser melting

**Palavras-chave em inglês:**

Additive manufacturing

Cobalt-based alloys

Materials characterization

Phase transformation

**Área de concentração:** Materiais e Processos de Fabricação

**Títuloção:** Doutor em Engenharia Mecânica

**Banca examinadora:**

Paula Fernanda da Silva Farina [Orientador]

Carlos Ângelo Nunes

Hélio Goldenstein

Paulo Roberto Mei

Juliano Soyama

**Data de defesa:** 26-09-2023

**Programa de Pós-Graduação:** Engenharia Mecânica

**Identificação e informações acadêmicas do(a) aluno(a)**

- ORCID do autor: <http://orcid.org/0000-0002-9994-5498>

- Currículo Lattes do autor: <http://lattes.cnpq.br/0389761517968767>

**UNIVERSIDADE ESTADUAL DE CAMPINAS  
FACULDADE DE ENGENHARIA MECÂNICA**

**TESE DE DOUTORADO ACADÊMICO**

**Efeito do tratamento térmico na  
transformação de fase  $\gamma - \epsilon$  da liga Co-28Cr-  
6Mo produzida por fusão seletiva a laser**

Autor: Luiz Henrique Martinez Antunes

Orientadora: Profa. Dra. Paula Fernanda da Silva Farina

Coorientador: Prof. Dr. Miloslav Béréš

A Banca Examinadora composta pelos membros abaixo aprovou esta Tese:

---

**Profa. Dra. Paula Fernanda da Silva Farina, Presidente**  
**DEMM / FEM / Unicamp**

---

**Prof. Dr. Carlos Ângelo Nunes**  
**DEMAR / EEL / USP**

---

**Prof. Dr. Hélio Goldenstein**  
**PMT / Poli / USP**

---

**Prof. Dr. Paulo Roberto Mei**  
**DEMM / FEM / Unicamp**

---

**Prof. Dr. Juliano Soyama**  
**DEMM / FEM / Unicamp**

A Ata De Defesa com as respectivas assinaturas dos membros encontra-se no SIGA/Sistema de Fluxo de Dissertação/Tese e na Secretaria do Programa da Unidade.

Campinas, 26 de setembro de 2023.

## **Dedicatória**

Ao meus pais, Luiz e Suzeti, à minha esposa, Larissa e ao meu filho, Felipe.

## Agradecimentos

Este trabalho não poderia ter sido realizado sem a colaboração das seguintes pessoas e instituições, as quais agradeço por todo apoio e dedicação:

À professora Dra. Paula Fernanda da Silva Farina, pela orientação durante este período e por todas as discussões acerca do trabalho que o tornaram cada vez melhor.

Ao professor Dr. Miloslav Béréš, com quem aprendi como se faz pesquisa de ponta e quem me apresentou às técnicas avançadas de caracterização de materiais que renderam ótimos artigos.

Ao professor Dr. John Jairo Hoyos Hosquin, pela ajuda na execução dos ensaios na linha de luz síncrotron e, principalmente, pela contribuição na análise e discussão dos resultados.

Ao professor Dr. Ronaldo Câmara Cozza, que viabilizou os ensaios de desgaste microabrasivo e auxiliou na análise dos resultados obtidos.

À professora Dra. Cecília Amélia de Carvalho Zavaglia, pelo suporte, especialmente nos momentos iniciais do projeto.

Ao professor Dr. Carmo Pellicciari (*in memoriam*). Pelas ótimas discussões e momentos sempre agradáveis.

Aos técnicos da UNICAMP, Eduardo José Bernardes, pela ajuda com a preparação metalográfica; Claudenete Vieira Leal e Márcia de Oliveira Taipina, pelo auxílio com a caracterização microestrutural; João Eduardo Polis e José Luis Lisboa no preparo e ensaio mecânico das amostras.

Ao Instituto Biofabris, em especial ao Dr. André Luiz Jardini Munhoz, que viabilizou e ao técnico Luis Fernando Bernardes, que executou a fabricação das amostras.

À equipe do LNNano: Msc. Fabiano Emmanuel Montoro e João Marcos da Silva, pelo treinamento e caracterização das amostras no MEV. Dr. Naga Vishnu Vardhan Mogili e Dr. Carlos Alberto Ospina Ramirez pelo treinamento e caracterização das amostras no MET. E ao técnico Joel de Souza Alencar pelo auxílio na preparação das amostras.

À equipe do LNLS, em especial ao Leonardo Wu, pelo suporte na execução dos ensaios na linha de luz síncrotron.

Ao Instituto Nacional de Ciência e Tecnologia em Biofabricação (INCTBiofabris) Pelo fornecimento de matéria prima e fabricação do material de estudo deste projeto.

À Faculdade de Engenharia Mecânica da UNICAMP pelas instalações utilizadas no trabalho e por todo apoio técnico e pessoal.

Aos amigos, Gabriel Shinkawa, Guilherme Longhitano, Guinea Cardoso, Andrei Bavaresco e demais colegas de laboratório.

À minha esposa, Larissa, pela paciência e pelo apoio incondicional. Ao meu filho, Felipe, irmão mais novo desta tese e que agora terá toda a atenção que merece. Aos meus pais, Suzeti e Luiz, por todo carinho e apoio, sempre acreditando em mim e me proporcionando a melhor educação possível. Amo vocês!

O presente trabalho foi realizado com apoio da Coordenação de Aperfeiçoamento de Pessoal de Nível Superior – Brasil (CAPES) – Código de Financiamento 001

## Resumo

A liga Co-28Cr-6Mo é conhecida por sua biocompatibilidade, elevada resistência mecânica e resistência ao desgaste, o que a torna uma ótima opção para aplicações biomédicas. Esta liga apresenta uma transformação polimórfica  $\gamma$ -CFC –  $\epsilon$ -HC, por volta de 970°C, durante o resfriamento em equilíbrio. A fase de alta temperatura,  $\gamma$ -CFC, pode ser facilmente estabilizada em temperatura ambiente quando resfriada rapidamente. Quando o material constituído pela fase  $\gamma$ -CFC metaestável é submetido a uma deformação e/ou a um tratamento térmico de envelhecimento, ocorre a nucleação da fase  $\epsilon$ -HC. Por mais que os mecanismos envolvidos nesta transformação já tenham sido estudados em amostras fundidas, não há registros de análises aprofundadas da transformação de fase em amostras da liga Co-28Cr-6Mo obtidas por manufatura aditiva. Portanto, o presente trabalho objetivou caracterizar extensivamente a transformação de fase  $\gamma$ -CFC –  $\epsilon$ -HC, na liga Co-28Cr-6Mo obtida pela técnica de manufatura aditiva *laser-powder bed fusion*. O trabalho está dividido em dois blocos. No primeiro bloco são apresentadas as caracterizações *in situ* da transformação martensítica induzida por deformação. A primeira parte deste estudo foi realizada em amostras como produzidas e solubilizadas a 1150°C por 1 hora. Observou-se que a realização do tratamento térmico de solubilização aumenta consideravelmente a ductilidade da liga tanto pela redução das tensões residuais como também pela ocorrência do efeito TRIP. Na segunda parte do primeiro bloco, foi realizado o estudo do efeito da transformação induzida por deformação na superfície e no núcleo de amostras como produzidas. Nota-se uma clara diferença e comportamento entre as regiões analisadas. Por fim, no segundo bloco, é apresentada a caracterização *in situ* da transformação de fases isotérmica, por tratamento térmico de envelhecimento a 800°C por 4 horas, em amostras como produzidas e solubilizadas a 1150°C por 1 hora. Nesta etapa verificou-se que a transformação  $\gamma$ -CFC –  $\epsilon$ -HC ocorre mais lentamente na amostra solubilizada, pois esta possui menos parciais de Shockley, que são consumidas durante o início da transformação e atuam como pontos de nucleação da fase  $\epsilon$ -HC, reduzindo assim a cinética de transformação.

## Abstract

The Co-28Cr-6Mo alloy is known for its biocompatibility, high mechanical strength, and wear resistance, making it an excellent choice for biomedical applications. This alloy undergoes a polymorphic transformation from  $\gamma$ -fcc (face-centered cubic) to  $\epsilon$ -hcp (hexagonal close-packed) at around 970°C during equilibrium cooling. The high-temperature phase,  $\gamma$ -fcc, can be easily stabilized at room temperature when rapidly cooled. When the material consisting of metastable  $\gamma$ -fcc phase undergoes deformation and/or aging heat treatment, nucleation of the  $\epsilon$ -hcp phase occurs. Although the mechanisms involved in this transformation have been studied in cast samples, there are no records of in-depth analyses of phase transformation in Co-28Cr-6Mo alloy samples obtained through additive manufacturing. Therefore, the present study aimed to extensively characterize the  $\gamma$ -fcc to  $\epsilon$ -hcp phase transformation in the Co-28Cr-6Mo alloy obtained through laser-powder bed fusion additive manufacturing technique. The study is divided into two sections. The first section presents in situ characterizations of deformation-induced martensitic transformation. The first part of this study was conducted on as-produced samples and samples subjected to a solution treatment at 1150°C for 1 hour. It was observed that the implementation of the solution heat treatment significantly increases the ductility of the alloy, both by reducing residual stresses and by the occurrence of the TRIP effect. In the second part of the first section, the study focused on the effect of deformation-induced transformation on the surface and core regions of as-produced samples. Clear differences in behavior were observed between the analyzed regions. Finally, the second section presents in situ characterization of isothermal phase transformation through aging heat treatment at 800°C for 4 hours, applied to both as-produced and solution-treated samples. It was observed that the  $\gamma$ -fcc to  $\epsilon$ -hcp transformation occurs more slowly in the solution-treated sample due to the presence of fewer Shockley partials, which are consumed during the early stages of transformation and act as nucleation sites for the  $\epsilon$ -hcp phase, thus reducing the transformation kinetics.

## Sumário

1	Introdução.....	11
1.1	Histórico do grupo de trabalho .....	11
1.2	Considerações iniciais .....	12
1.3	Objetivos.....	13
2	Estrutura do Trabalho.....	15
3	Metodologia do processo de manufatura aditiva.....	16
4	Artigos.....	19
4.1	Bloco 1.1 – Effect of phase transformation on ductility of additively manufactured Co-28Cr-6Mo alloy: An <i>in situ</i> synchrotron X-ray diffraction study during mechanical testing 19	
4.2	Bloco 1.2 – Deformation-induced martensitic transformation in Co-28Cr-6Mo alloy produced by laser powder bed fusion: comparison surface <i>vs.</i> bulk .....	40
4.3	Bloco 2 – Kinetics of FCC to HCP transformation during aging heat treatment of Co-28Cr-6Mo alloy fabricated by laser-powder bed fusion.....	66
5	Síntese dos resultados e discussão geral .....	88
6	Conclusões .....	90
7	Sugestões para trabalhos futuros .....	92
8	Publicações.....	93
9	Referências.....	95

# 1 Introdução

## 1.1 Histórico do grupo de trabalho

O trabalho com a manufatura aditiva de ligas metálicas, na Unicamp, teve início em meados dos anos 2000 no Instituto Nacional de Biofabricação (Biofabris) em parceria com a Faculdade de Engenharia Mecânica e a Faculdade de Ciências Médicas. As primeiras ligas estudadas foram as base Ti, em especial a Ti6Al4V. Destas pesquisas resultaram dissertações de mestrado, teses de doutorado e artigos científicos que avaliaram de forma extensiva características mecânicas, microestruturais e o efeito do laser nessas ligas quando produzidas por manufatura aditiva. A partir dos anos 2010 houve maior interação com o grupo de pesquisa liderado pelo professor Juan Damborenea, da Espanha, sobre a funcionalização superficial das ligas de Ti. Complementarmente, foram realizadas cirurgias reparadoras, especialmente de calotas cranianas, em parceria com o Hospital Sobrapar. Foram casos pioneiros que fortaleceram a atuação do Biofabris como centro de excelência da manufatura aditiva aplicada à área médica.

Em 2015, iniciou-se o trabalho com a liga Co-28Cr-6Mo. O mestrado desenvolvido por mim e sob orientação da professora Cecília Zavaglia, caracterizou peças da liga produzida por manufatura aditiva comparando com o processo tradicional de fabricação, por fundição de precisão. Concomitante a isso houve o início das pesquisas com o aço inoxidável austenítico F138 produzido por manufatura aditiva. Ao final deste período e desde então, o Biofabris firmou uma importante parceria com a Universidade Federal do Ceará na figura do professor Miloslav Béréš. Tal parceria proporcionou acesso a centros de excelência no Brasil, como o Centro Nacional de Pesquisa em Energia e Materiais, e no mundo, como o a linha de luz síncrotron DESY, na Alemanha.

No período de desenvolvimento deste doutorado foram firmadas outras parcerias com instituições que buscavam aplicar a tecnologia da manufatura aditiva na área médica e proporcionaram grandes avanços nas caracterizações *in situ* e *in vivo* das ligas metálicas processadas pelo Biofabris. Foram elas, a Faculdade de Medicina de Bauru, a Faculdade de Medicina de Jundiaí e a Faculdade de Odontologia de Piracicaba. Os trabalhos em realizados com tais instituições geraram artigos científicos e estão listados na sessão 8 desta tese.

## 1.2 Considerações iniciais

O desenvolvimento e aprimoramento de biomateriais e de técnicas cirúrgicas ortopédicas, tanto reparadoras quanto de substituição é essencial, não somente para atender à crescente demanda por esse tipo de procedimento, mas também para que os pacientes tenham uma rápida recuperação e maior qualidade de vida no pós-operatório (JARDINI *et al.*, 2014). Materiais biomédicos, sejam de fixação de fraturas ou de implantes ortopédicos, devem possuir propriedades mecânicas adequadas, para desempenharem suas funções e suportarem as cargas aplicadas pelo corpo quando solicitados. Neste contexto, alguns materiais metálicos se destacam por apresentarem não somente resistência mecânica e à corrosão favoráveis, mas também biocompatibilidade. Dentre estes metais estão as ligas à base de cobalto, as quais apresentam elevada resistência mecânica e alta resistência ao desgaste (ANDERSEN, 2011; GURAPPA, 2002; KLARSTROM, 1993a). Estas propriedades conferem às ligas à base de cobalto a indicação para o uso em implantes que são submetidos a solicitações mecânicas e, principalmente, atrito, como ocorre nos joelhos e quadris. O material utilizado neste trabalho foi o MP1, da empresa EOS GmbH (EOS, 2011). Este material atende, dentre outras, a norma ASTM F75. Por questões de praticidade, a liga deste trabalho será denominada, F75.

Uma característica do cobalto e suas ligas é a presença de uma transformação de fases alotrópica que ocorre a 427 °C para o material puro e a 970 °C (polimórfica) para a liga F75 (SALDÍVAR GARCÍA, A. D.J. *et al.*, 1999). Nesta transformação, a fase cúbica de faces centradas (CFC), identificada como  $\gamma$ -CFC, transforma-se em uma fase hexagonal compacta (HC), identificada como  $\varepsilon$ -HC, durante o resfriamento do material. Realizando-se um tratamento térmico de solubilização, acima da temperatura de transformação, seguido de resfriamento rápido, é possível obter a fase  $\gamma$ -CFC em temperatura ambiente. Esta fase apresenta-se em uma condição metaestável e pode se transformar em  $\varepsilon$ -HC após um tratamento térmico de envelhecimento ou pelo fenômeno da transformação martensítica induzida por deformação (SIMT).

Por conta da alta resistência mecânica das ligas à base de cobalto, o processo de usinagem torna-se caro. Desta forma, opta-se pela fundição de precisão como método de produção de peças, diminuindo assim o custo das mesmas (DISEGI; KENNEDY; PILLIAR, 1999). No entanto, as peças fundidas apresentam alta porosidade, inerente ao processo de fundição. Neste contexto, buscando o desenvolvimento de peças personalizadas e otimizadas para cada paciente (LIVERANI *et al.*, 2016), com propriedades iguais ou superiores às das técnicas de produção

tradicionais (BARUCCA *et al.*, 2015b; MENGUCCI *et al.*, 2016), a manufatura aditiva (MA) tornou-se uma alternativa interessante. A MA está cada vez mais presente, com a popularização e avanço da técnica, que hoje permite a fabricação de peças com diversos tipos de materiais, inclusive metais, a partir do processo de Fusão à Laser em Leito de Pó (L-PBF).

O estudo para viabilizar a utilização da manufatura aditiva na produção de peças da liga F75 vem crescendo nos últimos anos (ANTUNES *et al.*, 2019; BARUCCA *et al.*, 2015a; BÉREŠ *et al.*, 2018a; GIRARDIN *et al.*, 2016; TAKAICHI *et al.*, 2013). No entanto, ainda não há na literatura um estudo aprofundado sobre a transformação de fase CFC-HC que ocorre nesta liga. Tal conhecimento é fundamental para otimizar o desempenho da liga F75 por meio de tratamentos térmicos e para prever seu comportamento em trabalho, em especial no caso da resistência ao desgaste, que promove a transformação de fase induzida por deformação durante o uso de um implante ortopédico, por exemplo.

Considerando: i) que a transformação polimórfica ( $\gamma$ -CFC –  $\epsilon$ -HC) ocorre na liga F75; ii) que a transformação de fase pode ser induzida por deformação ou via tratamento térmico de envelhecimento; iii) que a literatura apresenta poucos estudos aprofundados sobre os efeitos da transformação de fase  $\gamma$ -CFC –  $\epsilon$ -HC na liga F75 obtida por manufatura aditiva, verifica-se a necessidade de um estudo mais aprofundado sobre os efeitos da transformação martensítica  $\gamma$ -CFC –  $\epsilon$ -HC no comportamento mecânico desta liga.

### 1.3 Objetivos

O principal objetivo deste trabalho é estudar a transformação martensítica  $\gamma$ -CFC –  $\epsilon$ -HC, característica do cobalto e suas ligas, tanto pelo fenômeno de SIMT quanto pelo mecanismo difusional em amostras da liga ASTM-F75 obtidas pelo método de manufatura aditiva L-PBF.

Para alcançar o objetivo principal foram traçadas as seguintes metas:

1. Revisão bibliográfica atualizada da literatura;
2. Produção de amostras da liga F75 por L-PBF;
3. Tratamentos térmicos de solubilização e envelhecimento em parte das amostras;
4. Caracterização microestrutural das amostras por microscopia eletrônica de varredura com mapas de Difração de Elétrons Retroespalhados (EBSD);
5. Caracterização microestrutural das amostras por microscopia eletrônica de transmissão;

6. Caracterização mecânica do material em tração convencional e também *in-situ*, com a realização simultânea de difração de raios-X, utilizando linhas de luz síncrotron.

## 2 Estrutura do Trabalho

A presente tese está de acordo com o Parágrafo 2º da Informação CCPG 002/2018, que permite a apresentação de teses e dissertações em formato alternativo ao modelo tradicional. Ou seja, o conteúdo desta tese está sumarizado em três artigos publicados em revistas científicas e cada um destes artigos representa um Bloco do trabalho. O Bloco 1 apresenta o estudo realizado sobre a ocorrência da transformação de fase CFC – HC induzida por deformação na liga Co-28Cr-6Mo e o Bloco 2 traz os resultados do estudo sobre a transformação de fase isotérmica CFC – HC na liga Co-28Cr-6Mo.

Os artigos apresentados no Bloco 1 são: i) *Effect of phase transformation on ductility of additively manufactured Co-28Cr-6Mo alloy: An in situ synchrotron X-ray diffraction study during mechanical testing*, publicado em 2019 na revista *Materials Science and Engineering A* e ii) *Deformation-induced martensitic transformation in Co-28Cr-6Mo alloy produced by laser powder bed fusion: comparison surface vs. bulk*, publicado em 2021 na revista *Additive Manufacturing*. Já o artigo referente ao Bloco 2, cujo título é *Kinetics of FCC to HCP transformation during aging heat treatment of Co-28Cr-6Mo alloy fabricated by laser-powder bed fusion*, foi publicado em 2023 na revista *Metallurgical and Materials Transactions A*.

### 3 Metodologia do processo de manufatura aditiva

Pelo fato de a presente tese estar seguindo um modelo alternativo de apresentação, algumas informações elementares do trabalho podem vir a ficar pouco claras. Os artigos científicos que contemplam a estrutura deste trabalho foram publicados em revistas bastante especializadas e, por conta disso, não houve a necessidade de abordar conceitos mais básicos das técnicas utilizadas. Portanto, nesta sessão serão apresentadas algumas informações sobre o processo de manufatura aditiva a fim de esclarecer o processo de obtenção das amostras utilizadas no trabalho.

Para realizar a fabricação por manufatura aditiva é necessário ter um modelo digital tridimensional da peça desejada. Este modelo deve ser transferido para o software do equipamento de manufatura aditiva, onde será “fatiado” em camadas semelhantes a curvas de nível da peça, sendo possível determinar onde deve-se ou não depositar material. Estas camadas são, por fim, processadas em sequência e a fabricação inicia-se pela deposição de material, camada por camada.

Na técnica denominada fusão seletiva a laser em leito de pó, a construção da peça é toda feita dentro de uma câmara com atmosfera controlada de nitrogênio e utiliza um laser do tipo fibra feito de itérbio com potência entre 200 e 400 W, o que garante um feixe mais estreito e maior precisão na construção da peça para fundir parcialmente cada camada de material que é depositada até formar a peça.

A Figura 1 apresenta um esquema do passo a passo do processo que se inicia com o espalhamento de uma fina camada de material sobre uma superfície verticalmente móvel. Um sistema de espelhos controla o movimento do laser que descreve a geometria da camada, obtida do arquivo eletrônico, sobre o material. A incidência do laser promove a fusão do metal, que se une com a camada de material abaixo. Ao final da etapa de fusão, a superfície sobre a qual a peça está sendo montada é baixada o equivalente a espessura da próxima camada que será fundida – o que pode variar de 20 a 100  $\mu\text{m}$  – e o material é novamente espalhado. Este processo se repete até que se obtenha a peça pronta e pode levar algumas horas a velocidades de 7 a 70  $\text{cm}^3/\text{h}$ , dependendo da espessura das camadas. Ao final do processo, o material excedente que envolve a peça pronta é retirado com um aspirador e pode ser reutilizado. Por fim, as amostras construídas devem ser removidas da placa metálica de construção que serve de suporte para as etapas iniciais do processo. Esta etapa costuma ser feita via eletroerosão à fio.

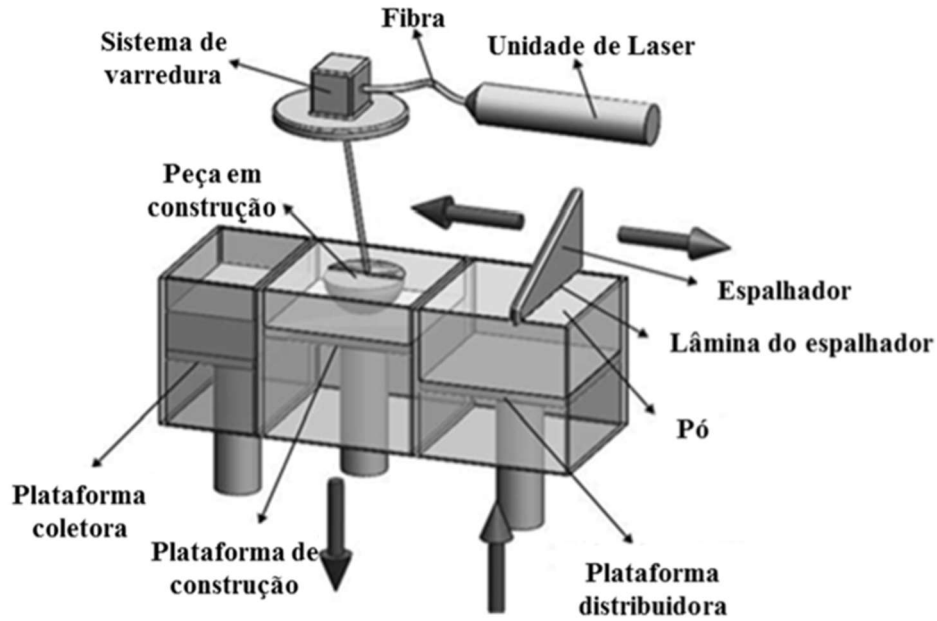


Figura 1 – Esquema do processo de produção por manufatura aditiva do tipo fusão seletiva a laser em leito de pó.

No presente trabalho, a técnica de fusão seletiva a laser em leito de pó foi realizada com o equipamento EOSINT M280, da empresa EOS GmbH. O pó metálico utilizado também foi produzido pela EOS e é denominado CobaltChrome MP1. Os parâmetros utilizados para a fabricação das amostras foram os padrões fornecidos pelo equipamento operando com este tipo de material. Por conta de um bloqueio de software, não foi possível alterá-los, mas sabe-se que são otimizados para a liga em questão e seus valores aproximados estão descritos na Tabela 1.

Tabela 1 – Parâmetros do equipamento EOSINT M280 para operar com a liga CobaltChrome MP1.

<b>Potência do laser</b>	200 W
<b>Diâmetro do feixe de laser</b>	100 – 500 $\mu\text{m}$
<b>Velocidade de varredura</b>	Até 7,0 m/s
<b>Espessura da camada</b>	20 $\mu\text{m}$
<b>Atmosfera</b>	Nitrogênio

As amostras utilizadas nos ensaios de tração *in situ* e convencional seguiram as dimensões apresentadas na Figura 2a e b, respectivamente e foram fabricadas seguindo a orientação indicada na Figura 3.

Figura 2 – Desenhos das amostras produzidas por manufatura aditiva para os ensaios de tração a) *in situ* e b) convencional. Dimensões em milímetros.

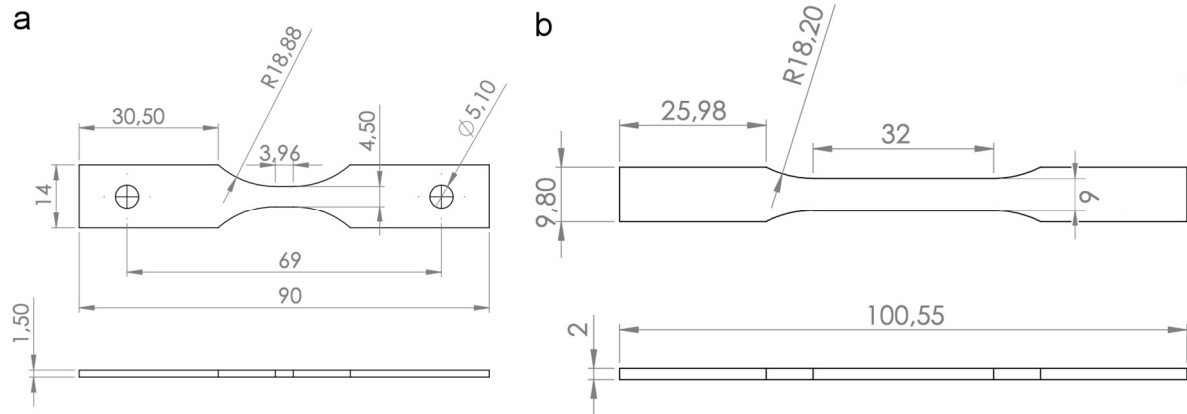
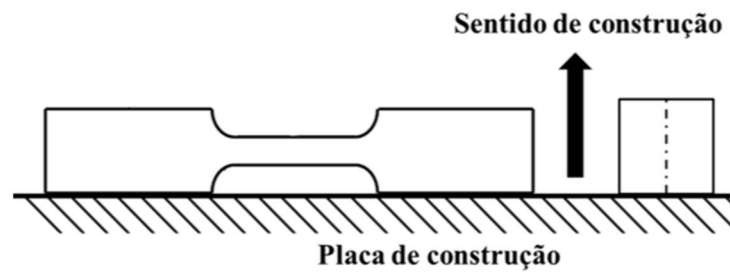


Figura 3 – Sentido de construção das amostras.



## 4 Artigos

### 4.1 Bloco 1.1 – Effect of phase transformation on ductility of additively manufactured Co-28Cr-6Mo alloy: An *in situ* synchrotron X-ray diffraction study during mechanical testing (<https://doi.org/10.1016/j.msea.2019.138262>)

L.H.M. Antunes<sup>a\*</sup>, J.J. Hoyos<sup>b</sup>, E. B. Fonseca<sup>a</sup>, M. Bérés<sup>c,d</sup>, P.F. da Silva Farina<sup>a</sup>, E.S.N. Lopes<sup>a</sup>, A.L. Jardini<sup>c</sup>, R. Maciel Filho<sup>c</sup>

<sup>a</sup> School of Mechanical Engineering, University of Campinas, Rua Mendeleev, 200, 13083-860, Campinas, SP, Brazil

<sup>b</sup> Materials Engineering Department, State University of Ponta Grossa, Av. General Carlos Cavalcanti, 4748, 84030-900, Ponta Grossa, Brazil

<sup>c</sup> National Institute of Biofabrication, Faculty of Chemical Engineering, University of Campinas, Av. Albert Einstein 500, 13083-852, Campinas, SP, Brazil

<sup>d</sup> Department of Metallurgical and Materials Engineering, Federal University of Ceará, Av. Humberto Monte, 60445-554, Fortaleza, CE, Brazil

\*Corresponding author: [lhmantunes@gmail.com](mailto:lhmantunes@gmail.com)

#### Abstract

The influence of strain-induced martensitic transformation on the mechanical properties of a Co-28Cr-6Mo alloy produced using the direct metal laser sintering additive manufacturing technique was analyzed. Both the as-built and solution heat-treated (ST) specimens were subjected to conventional tensile tests. Furthermore, X-ray diffraction spectra were simultaneously acquired using a synchrotron light source. In addition, electron backscatter diffraction analysis was performed on the specimens before and after tensile testing. Both techniques revealed the occurrence of the strain-induced  $\gamma$ -face-centered cubic  $\rightarrow$   $\epsilon$ -hexagonal close-packed phase transformation. The higher microstrain and preferential grain orientation of the as-built specimen favored the onset of the phase transformation. Moreover, the ductility of the ST specimen was significantly higher than that of the as-built specimen. This behavior was

attributed to the isotropic properties of the randomly-oriented and equiaxed grains, increase in resistance to necking, and reduction in internal stresses caused by the solution heat treatment.

## Introduction

The development and improvement of biomaterials and orthopedic surgical techniques is essential for medical, economic, technological, and scientific reasons. This is caused by the growing demand for prosthetic implant procedures, quicker recovery prospects, higher quality of life of patients during the postoperative period, and increase in patient life expectancy [1]. Implant materials for osteosynthesis of fractures or complete knee or hip arthroplasties must exhibit appropriate mechanical properties to resist loads when in use [2]. Therefore, some metallic materials are important, because of their favorable mechanical strength and corrosion resistance as well as adequate biocompatibility. Among them, Co-based alloys outperform other materials owing to their great wear resistance and high mechanical strength. This make them suitable for use for implants that undergo compression and friction stress, such as knee and hip joints [3,4].

Co and Co-based alloys present an allotropic transformation at approximately 970 °C [5]. The low- and high-temperature phases are known as the  $\epsilon$ -hexagonal close-packed (HCP) and  $\gamma$ -face-centered cubic (FCC) phases, respectively. In addition, fast cooling allows to retain the  $\gamma$ -FCC phase as metastable  $\gamma$ -FCC phase at room temperature. Such metastable  $\gamma$ -FCC phase could transform into  $\epsilon$ -HCP phase at room temperature via strain-induced martensitic transformation (SIMT) mechanism [6–8].

The SIMT occurs via the alteration of the atomic sequence from ABC-type for the  $\gamma$ -FCC phase to ABA-type for the  $\epsilon$ -HCP phase, which introduces a stacking fault at every  $\{111\}_{\gamma}$  plane [9]. This transformation is strongly dependent on the stacking fault energy (SFE) of the material. Huang [10] reported that SIMT was the dominant transformation mechanism for Co-Cr-Mo alloys featuring SFE values below 15 mJ/m<sup>2</sup>, while twinning prevailed when SFE was higher *i.e.*, between 15 and 50 mJ/m<sup>2</sup>.

Parts manufactured using Co-based alloys are conventionally produced via powder metallurgy or casting because these alloys present high mechanical strength and low machinability [11]. Such parts, however, commonly present inferior mechanical properties, which are caused by porosity and microsegregation, and are limited in terms of geometries. Recently, additive manufacturing techniques, such as direct metal laser sintering (DMLS), have

been used to produce customized and near-net-shape components for biomedical applications directly from metal powders [1,12–14]. Nevertheless, the microstructural inhomogeneities and microsegregation that could be present in laser sintered materials could negatively affect mechanical properties of the builds [15]. Therefore, to manufacture reliable implants, it is important to elucidate the effects of these features on the performance of such devices.

Columnar  $\gamma$ -FCC grains that are oriented parallel to the build direction usually develop in components manufactured from Co-based alloys using powder bed additive manufacturing technologies [16–18]. Compared with the  $\varepsilon$ -HCP phase, the  $\gamma$ -FCC phase confers some ductility to alloys. Generally, the ductility of the  $\gamma$ -FCC phase is higher than that of the  $\varepsilon$ -HCP phase owing to its larger number of active slip systems. However, the columnar microstructure that develops during the DMLS manufacturing process could cause the anisotropic behavior of the produced parts [19–22]. In the literature, different mechanical properties were determined from tensile tests using specimens that were manufactured between  $0^\circ$  and  $90^\circ$  in respect to the build direction [19–22]. Specimens obtained under the  $0^\circ$  angle, presented columnar grains oriented in the tensile load direction and higher ductility compared with the specimens produced under the  $90^\circ$  angle, which featured grains oriented perpendicularly to the tensile load. This was explained by the ease of dislocation movement in the specimens obtained under the  $0^\circ$  angle compared with that of the specimens obtained under the  $90^\circ$  angle [19,21,22]. Therefore, obtaining specimens with homogenous microstructure is one of the main challenges when using such alloys for artificial joint implants.

Recently, Ti-based alloys have been analyzed *in situ* studies using synchrotron light sources to investigate the melt pool dynamics [23] and phase transformations [24]. In addition, synchrotron light was used to analyze the phase transformations in Fe- and Co-based alloys manufactured via powder metallurgy [25].

In the present study, the mechanical behavior and microstructural evolution of the additively manufactured Co-28Cr-6Mo alloy were analyzed during tensile tests under two conditions: i) as-built; and ii) solution heat-treated (ST) at  $1150^\circ\text{C}$  for 1 h. The microstructural changes during load application were monitored by observing the evolution of strain-induced martensite, microstrain, grain size, and morphology. This was achieved using time-resolved synchrotron X-ray diffraction (XRD) combined with microstructural analysis. The analysis results revealed that higher microstrain values favored the nucleation of the strain-induced  $\gamma$ -FCC  $\rightarrow$   $\varepsilon$ -HCP phase transformation, and the extent of the phase transformation was correlated with the magnitude of the applied strain. Moreover, the solution heat treatment led to the

significant increase in ductility of the samples. This was attributed to the reduction in internal stresses in addition to the increase in resistance to necking and crack propagation delay owing to the transformation-induced plasticity (TRIP) mechanism.

## Experimental Procedure

Specimens were manufactured using an EOSINT 280 DMLS machine (EOS GmbH, Germany) utilizing MP1 Co-Cr-Mo metallic powder feedstock [26], which was supplied by EOS GmbH, Germany. The powder was laser-melted layer by layer using the manufacturer prescribed parameters utilizing an Yb-fiber laser with the nominal power of 200 W, laser spot size of 100  $\mu\text{m}$ , and scan speed of 800 mm/s. The obtained plate was heated to 80  $^{\circ}\text{C}$  while maintaining the oxygen content in the process chamber below 0.1%. Eight tensile tests specimens were produced, and the angle between the manufacturing direction and longitudinal tension axis (related to the tensile test) was 90 $^{\circ}$ . Half of the specimens were ST at 1150  $^{\circ}\text{C}$  for 1 h followed by water quenching and the other half were maintained in as-built condition.

Three samples from each category were prepared for conventional tensile testing and one sample from each category was prepared for *in situ* synchrotron radiation analysis during load application. The cross-section areas of the samples were 6  $\times$  2 and 3.96  $\times$  1.5 mm $^2$ , respectively (see Figure 1). These specimens were extracted from the manufactured plate using wire electro-discharge machining (WEDM). Moreover, the building supports were removed by grinding, which did not significantly affect the surface integrity or mechanical properties of the specimen [27]. Thus, the surface artifacts induced during mechanical fabrication methods (*e.g.*, cutting, grinding) were largely eliminated. No additional machining was performed. Klocke *et al.* [28] reported that samples subjected to modern WEDM techniques and grinding presented similar fatigue behavior, and the former technique allowed to generate samples with superior surface finish.

Conventional tensile tests were conducted on an MTS 810–FlexTest 40 tension/compression servohydraulic testing machine fitted with a 100 kN load cell. Three specimens were used for each set of conditions. A caliper was used to measure the initial cross section dimensions, and the values were input into the MTS 810 software. Tensile tests were performed at the strain rate of 5  $\times$  10 $^{-5}$  s $^{-1}$  at room temperature, and the average strain over 25 mm of gauge length was recorded using an MTS 632.24C-50 extensometer. Engineering stress–strain curves were obtained, and the mechanical properties of the samples were determined.

The yield stress values were calculated from the 0.2% offset. In addition, the strain hardening exponents were calculated using the true deformation at ultimate tensile strength (UTS).

*In situ* analysis tensile tests were carried out at the XRD-1 beamline of the X-ray Scattering and Thermo-Mechanical Simulation installation of the Brazilian Synchrotron Light Laboratory. One specimen was tested for each set of conditions. The experiments were performed at room temperature using the constant cross-head displacement of  $10^{-3}$  mm/s (strain rate of  $10^{-5}$  s $^{-1}$ ) while simultaneously acquiring the XRD patterns of the specimens. The experimental setup for the *in situ* tests consisted of a customized Gleeble thermomechanical simulator integrated with a synchrotron X-ray beam that operated at 12 keV ( $\lambda = 1.033$  Å). The diffraction intensity was recorded at 3 s intervals using two MYTHEN (microstrip system for time-resolved experiments) one-dimensional detectors. The changes in the sample cross-section at the gauge center were monitored during testing using a laser dilatometer.

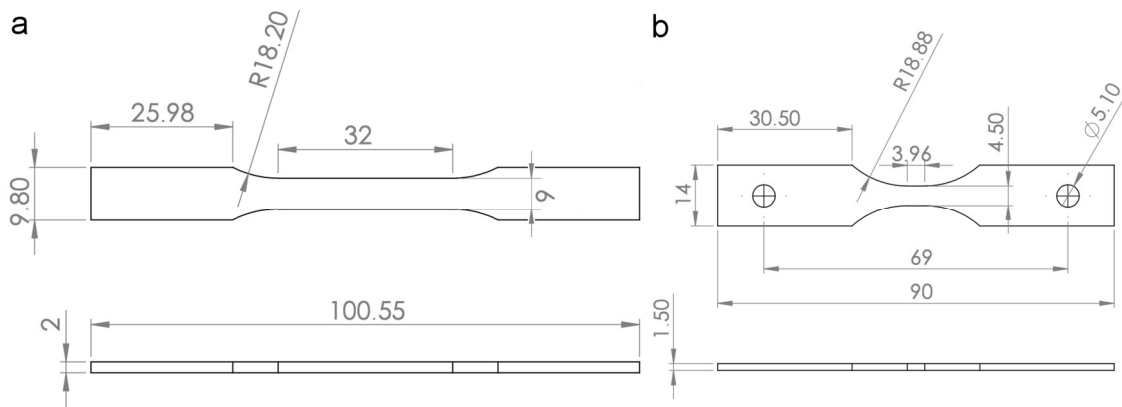


Figure 1 – Dimensions of tensile test specimens (mm) used for a) conventional tensile tests on MTS 810 machine and b) synchrotron *in situ* analysis.

The volume fraction ( $x_i$ ) of each phase was estimated from the integrated and theoretical intensities ( $I_i$  and  $R_i$ , respectively), as described using Equations (1) and (2).

$$x_i = \frac{\frac{1}{N} \sum_{j=1}^N \frac{I_{i,j}^{hkl}}{R_{i,j}^{hkl}}}{\sum_i \frac{1}{N} \sum_{j=1}^N \frac{I_{i,j}^{hkl}}{R_{i,j}^{hkl}}} \quad (1)$$

and

$$R^{hkl} = \frac{p^{hk} |F^{hkl}|^2 \left( e^{-\left(1 + \frac{\sin \omega}{\sin(2\theta - \omega)}\right)} \right)}{v_i^2 (4 \sin^2 \theta \cos \theta)}, \quad (2)$$

where  $p$  is the plane multiplicity factor,  $F$  is the plane structure factor,  $v$  is the volume of the unit cell,  $\omega$  is the angle of incident beam ( $15^\circ$ ), and  $\theta$  is the corrected peak angle [29].

The lattice microstrain values ( $e$ ) of the  $\gamma$ -FCC and  $\epsilon$ -HCP phases were estimated using the Stokes and Wilson Method (Equation (3)).

$$e = \frac{\beta \cos \theta}{4 \sin \theta} \quad (3)$$

where  $\beta$  is the full width at half maximum corrected by the instrument factor and  $\theta$  is the Bragg angle [29].

For microstructural characterization, scanning electron microscopy (SEM) images and electron backscatter diffraction (EBSD) maps were acquired at the reduced sections of the tensile test specimens before and after the *in situ* tests. In addition, micrographs were collected in the vicinity of the fractured surfaces. The specimens for EBSD analysis were polished electrolytically (21 V and  $15^\circ\text{C}$ ) using a solution of 5 vol.% concentrated perchloric acid in acetic acid as base electrolyte. After the tensile test was performed, the fractured region was cut and further polished using colloidal silica on a Buehler VibroMet<sup>TM</sup> 2 vibratory polisher for 48 h. The EBSD maps were acquired using the AZtecHKL software on a FEI Quanta 650 SEM instrument fitted with an HKL Nordlys orientation imaging system (Oxford Instruments, Oxford, UK). The HKL Channel 5 software package (Oxford Instruments, Oxford, UK) was used to process the EBSD data. In addition, elemental mapping using energy dispersive X-ray spectroscopy was performed employing a FEI Quanta 450 SEM instrument.

## Results

The chemical compositions of the as-built and ST specimens were obtained (see Table 1). The analysis was carried out using a PANalytical Axios X-ray fluorescence spectrometer, and the carbon content was determined using the combustion infrared detection technique using a LECO CS844 analyzer. The chemical compositions of both types of specimens were within the limits of the experimental errors for the accuracy of carbon and those of the other elements. Therefore, we concluded that the solution heat treatment did not affect the composition of the

specimens. Furthermore, the chemical compositions of both types of specimens were in accordance with the EOS powder datasheet [26] and ASTM F75 standard [30].

*Table 1 – Chemical composition of as-built and solution heat-treated (ST) specimens.*

Chemical composition (wt.%)								
	Co	Cr	Mo	Mn	Si	C	Fe	Ni
<b>As-built</b>	Balance	27.89	6.27	0.72	0.62	0.14	0.32	0.10
<b>ST</b>	Balance	27.58	6.27	0.68	0.58	0.13	0.36	0.12

The microstructure of the as-built specimens consisted of weld pools that formed fish scale-like structures comprising fine cellular dendrites (see Figure 2a), while the ST specimens presented equiaxed grains and some annealing twins (see Figure 2b). The densities of the as-built and ST specimens were evaluated using the Archimedes method [31], and the values were similar:  $8.28 \pm 0.04$  and  $8.26 \pm 0.07$  g/cm<sup>3</sup>, respectively. Considering that the theoretical density of this alloy system was 8.40 g/cm<sup>3</sup>, we concluded that the heat treatment did not affect its density.

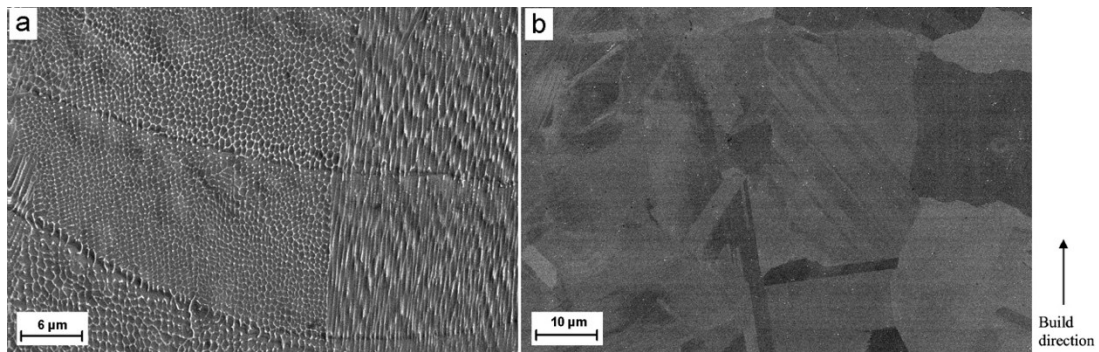


*Figure 2 – Secondary electrons scanning electron microscopy images of a) cellular dendrites inside fish scale-like microstructure of as-built specimen and b) equiaxed grains of solution heat-treated specimen.*

The dendritic structure observed for the as-built specimen could lead to the microsegregation at the interdendritic regions, which could cause the cracking of the material [12]. An inhomogeneity in the distribution of Mo and Co between the dendritic and interdendritic regions of the as-built specimens can be observed in Figure 3a. By contrast, no microsegregation was observed in Figure 3b, which indicated the uniform distribution of alloying elements after solution heat treatment.

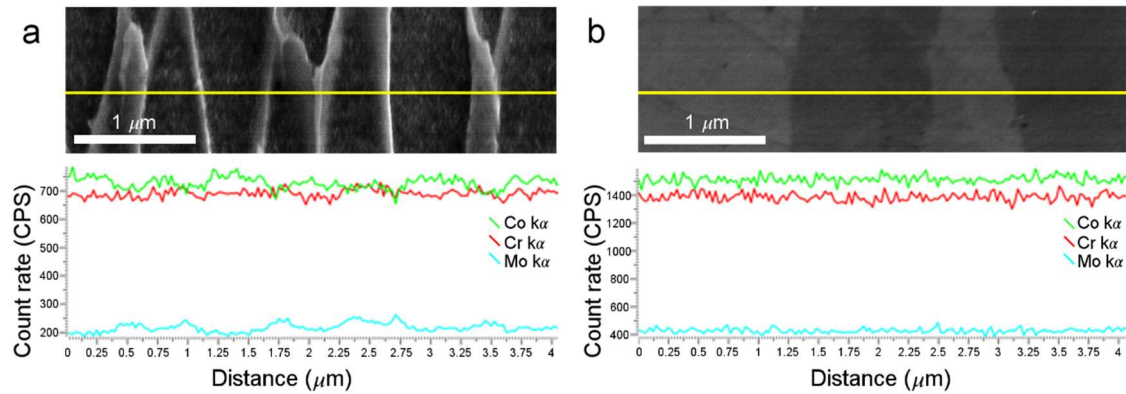


Figure 3 – Back-scattered electron micrographs (top images) and corresponding energy dispersive X-ray spectroscopy line scans (bottom graphs) of a) as-built specimen; and b) solution heat-treated specimen.

The EBSD inverse pole figure (IPF) maps of the as-built specimens revealed the presence of columnar grains (see Figure 4a), while the EBSD phase maps illustrated the  $\gamma$ -FCC structure of the specimens (see Figure 4c). Moreover, the IPF map of the as-built specimen revealed that the  $\{001\}$  planes were approximately 2.5 times more frequent than the random distribution (see Figure 4e). The  $\gamma$ -FCC structure was maintained in the ST specimens (see Figure 4b) and the columnar grains recrystallized into equiaxed grains (see Figure 4d). No preferential texture was observed in the IPF map of the ST specimen (see Figure 4f). Such microstructural features are typical for the DMLS process and are influenced by the fast cooling of the molten metal during the manufacturing process [12,19,32] and orientation of the build direction [18].

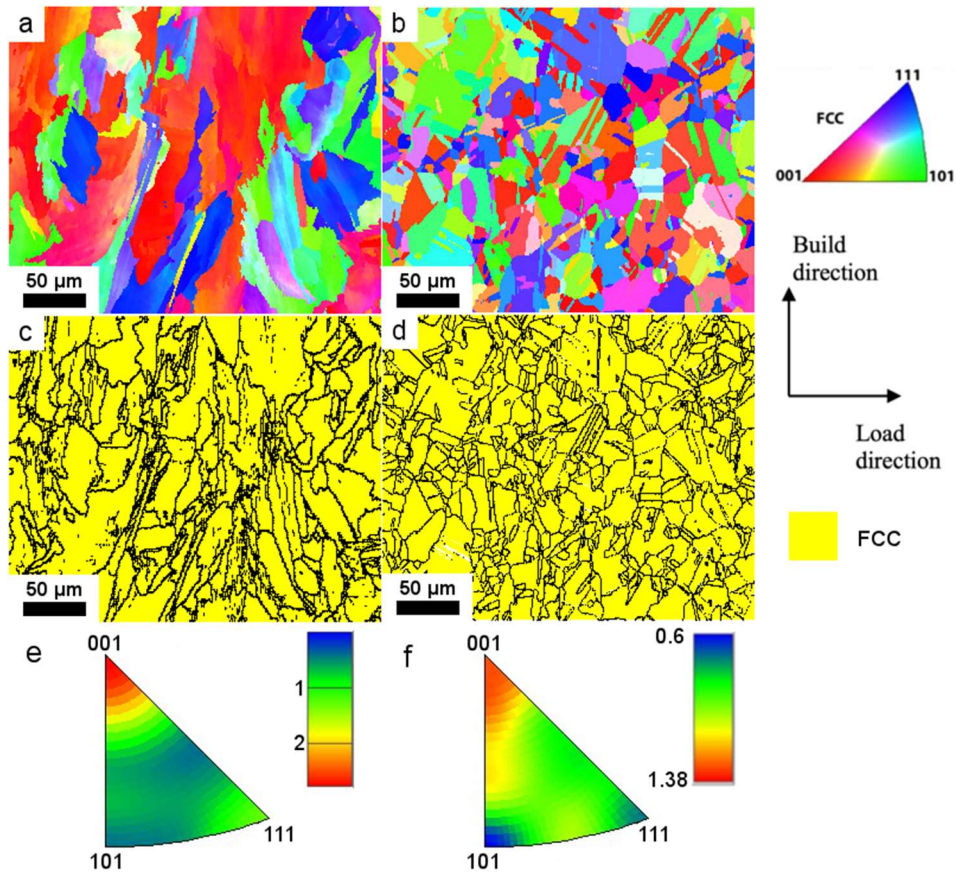


Figure 4 – a) and b) Electron backscatter diffraction (EBSD) inverse pole figure (IPF) maps, c) and d) EBSD phase maps, and e) and f) inverse pole figures of as-built and solution heat-treated specimens, respectively. (FCC is face-centered cubic)

Figure 5 depicts the representative engineering stress–strain curves for the two types of specimens (as-built and ST), which were obtained using the MTS 810 equipment. The mechanical properties of the specimens are summarized in the table in the inset. The solution heat treatment caused the yield stress of the specimens to decrease from 971.7 to 624.7 MPa. However, the ductility of the ST specimens increased from 6.3% to 19.8%. Three samples of each type were tested, and the standard deviations are listed in the table in the inset.

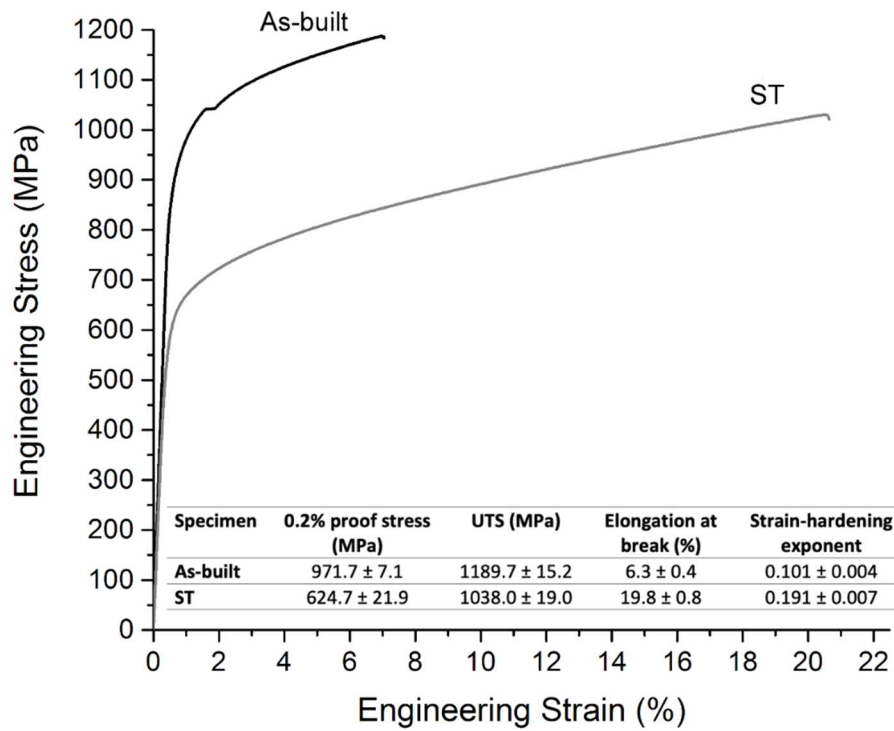


Figure 5 – Representative engineering stress–strain curves of as-built and solution heat-treated (ST) specimens, and their respective mechanical properties (the strain-hardening exponent corresponds to the true deformation at ultimate tensile strength (UTS)).

The formation of the  $\epsilon$ -HCP phase during tensile deformation was observed using the time-resolved synchrotron XRD technique (see Figures 6a and b). At the beginning of loading, a single-phase  $\gamma$ -FCC structure was identified. As the deformation increased, the  $\gamma$ -FCC  $\rightarrow$   $\epsilon$ -HCP phase transformation occurred and the peak intensity of the  $\gamma$ -FCC phase decreased. The quantitative analysis of the phases present (see Figures 6c and d) revealed that as the strain increased, the volumetric fraction of the  $\epsilon$ -HCP phase monotonically increased, and reached approximately 20 and 45 vol.% for the as-built and ST specimens, respectively. The  $\gamma$ -FCC  $\rightarrow$   $\epsilon$ -HCP transformation for the ST specimens was delayed, and occurred at higher strain values compared with those of the as-built specimen.

The lattice microstrain values of both phases are presented in Figures 6e and f. The microstrain value in the  $\gamma$ -FCC phase of the as-built specimen was higher than that of the ST specimen. The highest microstrain values were determined in the  $\{10\bar{1}1\}_\epsilon$  planes, and reached  $10 \times 10^{-3}$  and  $9 \times 10^{-3}$  for the as-built and ST specimens, respectively.

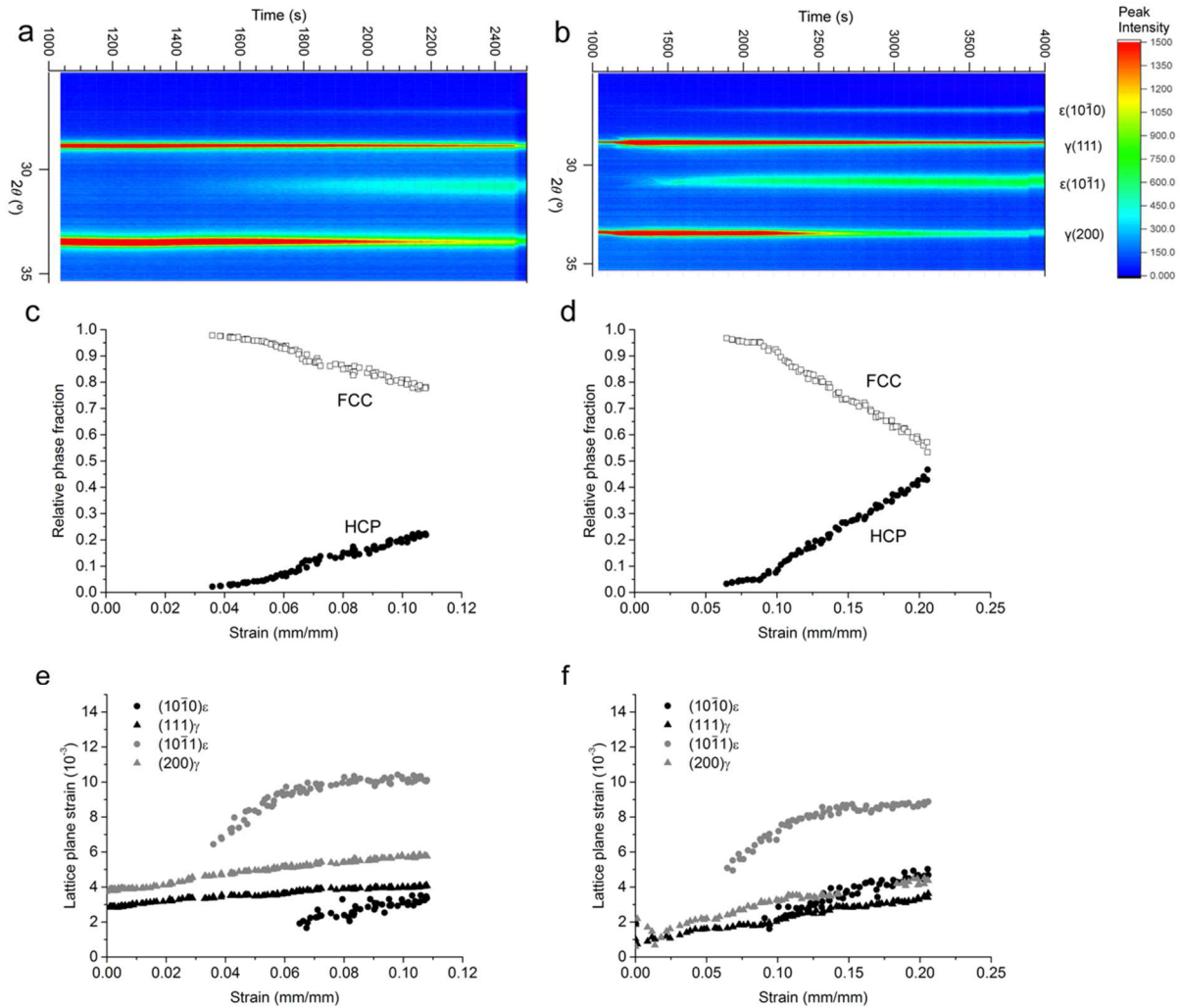


Figure 6 – a) and b) Time-resolved two-dimensional diffraction patterns obtained during in situ deformation of as-built and solution heat-treated (ST) specimens, respectively. c) and d) Relative fractions of  $\epsilon$ -hexagonal close-packed (HCP) and  $\gamma$ -face-centered cubic (FCC) phases present in as-built and ST specimens during tensile loading. e) and f) Lattice microstrain of cubic and hexagonal planes during tensile loading.

The EBSD analysis conducted near the fracture regions of the specimens after deformation, revealed that a high fraction of  $\epsilon$ -HCP phase nucleated via SIMT mechanism (see Figures 7a and b). This was attributed to the analyzed region being the most deformed section of the sample. Moreover, the IPF maps of the areas near the fracture regions of the as-built specimens (see Figure 7c) illustrated the shift in the preferential orientation of the FCC phase from the  $\{001\}$  toward the  $\{111\}$  planes, which were normal to the load direction. For the deformed ST specimen (see Figure 7d) this behavior was noted at smaller scale, since its grains were randomly oriented before the deformation occurred. The IPF maps indicated that both the  $\{111\}$  and  $\{001\}$  planes were preferentially oriented normal to the load direction in the ST specimens after deformation. The HCP phase also displayed preferential orientation, which was

close to the  $\{03\bar{3}2\}$  planes that were normal to the load direction, as indicated by the inverse pole figures in Figures 7e and f.

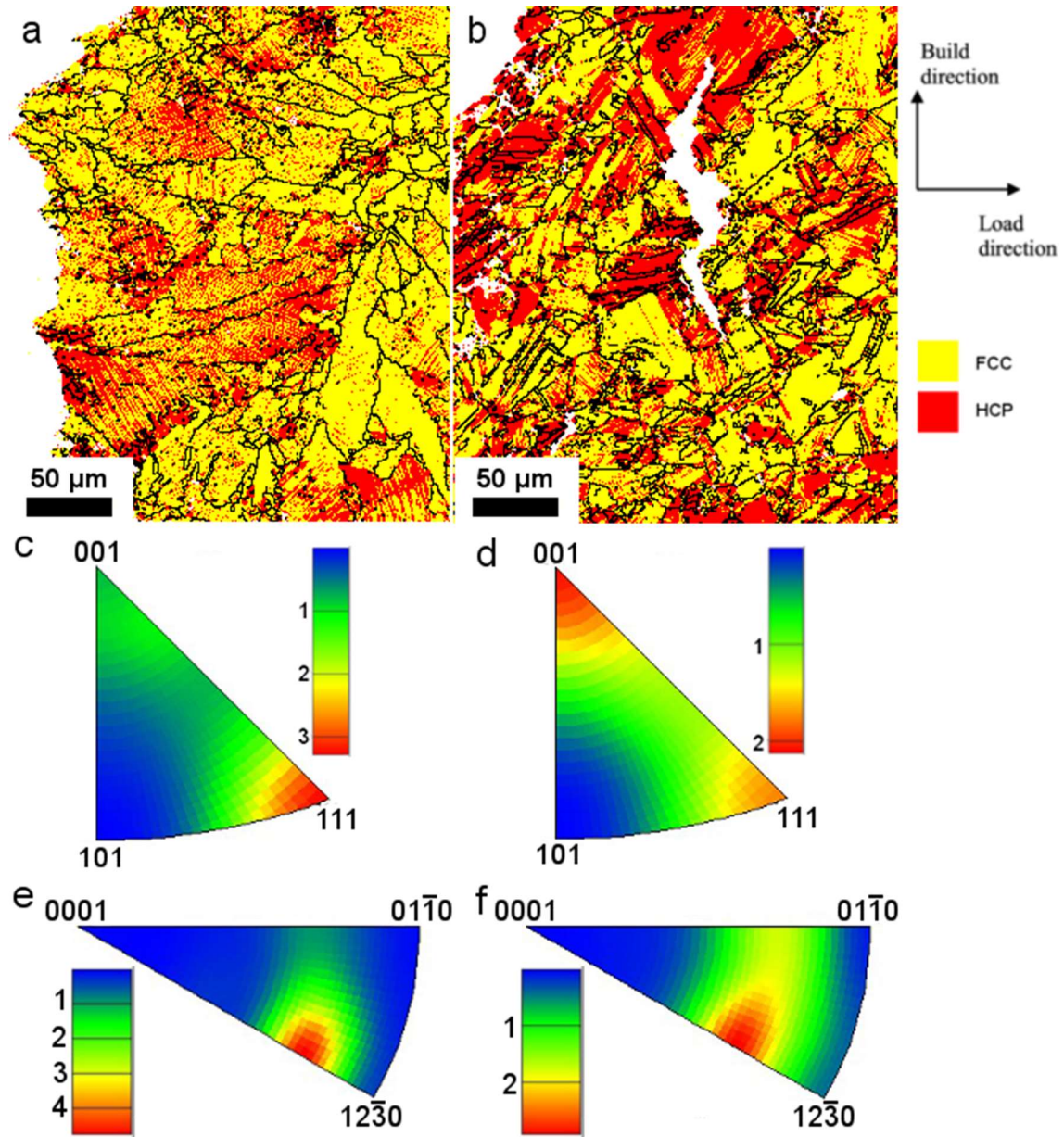


Figure 7 – a) and b) Electron backscatter diffraction phase maps in vicinity of fracture regions (left sides of the images), c) and d) inverse pole figure (IPF) maps of face-centered cubic (FCC) phase in load direction, and e) and f) inverse pole figures of hexagonal close-packed (HCP) phase in load direction of as-built and solution heat-treated specimens, respectively.

## Discussion

The solution heat treatment applied to the Co-Cr-Mo alloy manufactured via DMLS caused the recrystallization of the material (see Figure 4) and efficiently eliminated microsegregation (see Figure 3). High levels of microstrain could promote the recrystallization process owing to the accumulated microstrain providing an additional driving force for recrystallization. The magnitude of the microstrain present in the  $\gamma$ -FCC phase was higher for the as-built specimens than for the ST ones (see Figure 6). As reported in the literature [33–35], DMLS-produced parts exhibited high dislocations density, which was induced by the thermal contraction during the fast solidification of each deposited layer.

The recrystallization process is generally associated with the reduction in mechanical strength and decrease in microstrain, which results in the increase in ductility. The as-built specimens exhibited higher yield stress and UTS values than the ST specimens, which was in agreement with the results reported by Kajima *et al.* [15], who attributed the dissimilarities between these two types of specimens to the differences in grain boundary characteristics, precipitate distribution, and grain sizes, which hindered the movement of dislocations. The temperature of the solution heat treatments reported by Kajima *et al.* [15] was the same as that used in the present study (1150 °C). However, the isothermal dwell time of 6 h reported by Kajima *et al.* [15] was longer than that used in our study (1 h). Because the duration of the solution heat treatment in our study was shorter, both the formation of precipitates and grain coarsening were largely suppressed.

As indicated in previously published papers [19,21,22], the as-built specimens presented inhomogeneous microstructure owing to their elongated grains being aligned in a preferred orientation, in addition to solute segregation. Moreover, Hitzler *et al.* [21] observed an increase of up to 9.1% in ductility when the manufacturing angle was changed from 90° to 0° in respect to the build direction, which indicated the anisotropic behavior of the alloys.

Once the material was subjected to solution heat treatment, grains tended to become randomly oriented and equiaxed. The results of the grain aspect ratio analysis, which was performed using EBSD data, indicated that the aspect ratios of the as-built and ST specimens were  $2.9 \pm 2.32$  and  $1.3 \pm 0.54$ , respectively. Therefore, it was concluded that the as-built specimens were highly heterogeneous. The ductility measured in our study was 19.8%, while that reported in recent articles that evaluated the anisotropic behavior of additively manufactured Co-based alloys was 14.8% [19–21]. This indicated that the solution heat

treatment was more efficient for improving ductility than the selection of the appropriate manufacturing angle.

Moreover, the solution heat treatment could also lead to the decrease in lattice microstrain. The initial microstrain of the  $\gamma$ -FCC phase present in the as-built specimen (see Figure 6c) was higher than that observed for the ST specimen (see Figure 6d). This was the result of the accumulated residual stresses that developed during the thermal cycles of the build process. Therefore, the as-built specimens required lower macroscopic strain values to trigger the SIMT.

The  $\gamma$ -FCC microstrain of the as-built specimens increased by approximately 30% during tensile testing, while the  $\gamma$ -FCC microstrain of the ST specimens increased four times. This contributed to the higher strain-hardening exponent of the ST specimens (see Figure 5) compared with that of the as-built ones. The strain hardening exponent could be interpreted as a measure of the dislocations interactions with obstacles and other dislocations [36]. The higher strain hardening rate observed for the ST specimen could be attributed to the higher fraction of  $\epsilon$ -HCP/ $\gamma$ -FCC interfaces, which increased dislocation pile-up in the ST specimen.

Figures 6c and d reveal that as the strain increased, the volumetric fraction of the  $\epsilon$ -HCP phase increased monotonically, and reached approximately 20 and 45 vol.% for the as-built and ST specimens, respectively. The lower volumetric fraction of the  $\epsilon$ -HCP phase for the as-built specimen could be associated with the lower macroscopic strain levels reached during tensile testing. As depicted in Figure 5, the strain values at break of the as-built and ST specimens were 6.3% and 19.8%, respectively. Since the magnitude of the  $\gamma$ -FCC  $\rightarrow$   $\epsilon$ -HCP strain-induced phase transformation was proportional to the macroscopic strain levels, the extent of phase transformation was lower in the as-built specimen.

Owing to the highest deformation observed in the vicinity of the fracture regions of the tensile test specimens, higher macroscopic strain levels were reached in those regions. Consequently, higher fractions of  $\epsilon$ -HCP phase nucleated via SIMT, which created interfaces (see Figures 7a and b). The  $\gamma$ -FCC/ $\epsilon$ -HCP interfaces can act as barriers for dislocation gliding and other slip systems that had to be overcome during plastic deformation [37]. Therefore, in the high-strained region, higher stress values were required to overcome the newly created interfaces, which could have also contributed to the increase in the tensile strength of the alloy.

The changes in the preferential orientation of the  $\gamma$ -FCC phase from the  $\{001\}$  toward the  $\{111\}$  planes, which were normal to the load direction near the fracture for the as-built specimens (see Figure 7c), caused the slip system to be activated upon deformation. When the

{111} planes became normal to the load direction, the {111}<110> slip system in the  $\gamma$ -FCC phase was suppressed, which also resulted in the increase in strength of the specimens. The orientation of some grains was favorable for the gliding of the {111}<110> slip system; those grains could have undergone martensitic transformation upon deformation at lower strain values. As noted in the previous section, the results of the time-resolved XRD experiments revealed that lower strain values were necessary to trigger the  $\gamma$ -FCC  $\rightarrow$   $\epsilon$ -HCP phase transformation. At the same time, the grains of the ST specimens were more randomly oriented and martensitic transformation started at higher strain values.

The measured ductility of the ST specimens was higher than that of the as-build ones. This could be considered analogous to the phenomenon observed for TRIP steels. Moreover, the strain hardening exponent of the ST specimens was higher than that of the as-built ones. The instability before necking of the ST specimen was delayed owing to the formation of the HCP phase, and subsequently, more material could be deformed before necking. The increase in resistance to necking of the ST specimen indicated that the high work hardening rate was maintained until higher strain was reached, which is the main characteristic of the TRIP effect [38–40]. Consequently, the increase in the volume of the  $\epsilon$ -HCP (martensite) phase maintained the high work hardening rate until higher strain was reached. This led to the increase in uniform elongation. The TRIP effect in Co-based alloys is different than the conventional TRIP effect reported in steels, because for the later, the intensive formation of  $\alpha'$ -martensite caused the increase in tensile strength and decrease in ductility [38–40]. This difference was attributed to the different characteristics of  $\epsilon$ - and  $\alpha'$ -martensites. Furthermore,  $\epsilon$ -martensite exerted a softening effect in metastable austenitic stainless steels [41].

In addition, the strain hardening rate could also be increased by reducing the SFE, which would inhibit the cross-slip of dislocations. Lower SFE levels would cause larger equilibrium spacing between partial dislocations. Therefore, the ability of dislocations to change slip planes could be suppressed, and consequently, dislocations would be restricted to move in the {111} planes in the  $\gamma$ -FCC crystal. Stacking faults are nucleation sites for the  $\epsilon$ -HCP phase [42] and/or twin formation [12,43]. As strain increases, stacking faults are induced more easily. This occurs because the bulk free energy and stacking fault total energy are minimized, which cause higher strain hardening rate [44].

## Conclusions

In this study we have analyzed the microstructure, phase transformation, and mechanical behavior during tensile loading of the additively manufactured Co-28Cr-6Mo alloy before and after solution heat treatment. The following conclusions were drawn:

- The as-built specimens presented elongated  $\gamma$ -FCC phase grains along the manufacturing direction. The solution heat treatment generated randomly-oriented equiaxed  $\gamma$ -FCC grains.
- *In situ* XRD analysis of the tensile-loaded specimens revealed the strain-induced nucleation of the  $\epsilon$ -HCP phase. Moreover, its volume fraction increased with the progressing strain.
- The onset of the  $\gamma$ -FCC  $\rightarrow$   $\epsilon$ -HCP phase transformation was delayed in the ST specimens. That was associated with lower lattice microstrain values at the beginning of loading and randomly oriented grains.
- Solution heat treatment caused the yield stress to decrease and the ductility to increase.
- Solution heat treatment was more efficient at increasing ductility than the change in manufacturing direction reported in the literature.
- The decrease in internal stress after solution heat treatment in addition to the increase in resistance to necking and crack propagation caused by the TRIP mechanism could explain the increase in ductility for the ST specimens.

## Acknowledgments

The authors are grateful for the assistance L. F. Bernardes and D. C. de Araujo provided with the manufacturing of the specimens. The experimental support of F.E. Montoro (project SEM 21795) at the Brazilian Nanotechnology National Laboratory (LNNano) is also acknowledged. This study used the resources of the Brazilian Synchrotron Light Laboratory, an open national facility operated by the Brazilian Centre for Research in Energy and Materials for the Brazilian Ministry for Science, Technology, Innovations and Communications. We would like to thank the X-ray Scattering and Thermo-Mechanical Simulation beamline staff (L. Wu) for the assistance during the synchrotron experiments. The microstructural characterization of the specimens was performed at LNNano and the Analytical Center of

UFC/CT-INFRA/MCTI-SISNANO. This study was financed in part by the Coordenação de Aperfeiçoamento de Pessoal de Nível Superior, Brasil, Finance Code 001, CNPq, and São Paulo Research Foundation FAPESP (grant number 2016/09350-2).

## References

- [1] A.L. Jardini, M.A. Larosa, R.M. Filho, C.A. de C. Zavaglia, L.F. Bernardes, C.S. Lambert, D.R. Calderoni, P. Kharmandayan, Cranial reconstruction: 3D biomodel and custom-built implant created using additive manufacturing, *J. Cranio-Maxillofacial Surg.* 42 (2014) 1877–1884. doi:10.1016/j.jcms.2014.07.006.
- [2] G. Criscenti, C. De Maria, E. Sebastiani, M. Tei, G. Placella, A. Speziali, G. Vozzi, G. Cerulli, Material and structural tensile properties of the human medial patello-femoral ligament, *J. Mech. Behav. Biomed. Mater.* 54 (2016) 141–148. doi:10.1016/j.jmbbm.2015.09.030.
- [3] J. Cawley, J.E.P. Metcalf, A.H. Jones, T.J. Band, D.S. Skupien, A tribological study of cobalt chromium molybdenum alloys used in metal-on-metal resurfacing hip arthroplasty, *Wear.* 255 (2003) 999–1006. doi:10.1016/S0043-1648(03)00046-2.
- [4] J.M. Murnaghan, A.J. Hamer, Hip and knee replacement, *Surgery.* 28 (2010) 508–513. doi:10.1016/j.mpsur.2010.07.003.
- [5] A.D.J. Saldívar García, A.M. Medrano, A.S. Rodríguez, Formation of hcp martensite during the isothermal aging of an fcc Co-27Cr-5Mo-0.05C orthopedic implant alloy, *Metall. Mater. Trans. A.* 30 (1999) 1177–1184. doi:10.1007/s11661-999-0267-6.
- [6] G.B. Olson, M. Cohen, A mechanism for the strain-induced nucleation of martensitic transformations, *J. Less Common Met.* 28 (1972) 107–118. doi:10.1016/0022-5088(72)90173-7.
- [7] X. Wu, N. Tao, Y. Hong, G. Liu, B. Xu, J. Lu, K. Lu, Strain-induced grain refinement of cobalt during surface mechanical attrition treatment, *Acta Mater.* 53 (2005) 681–691. doi:10.1016/j.actamat.2004.10.021.
- [8] K. Yamanaka, M. Mori, A. Chiba, Nanoarchitected Co–Cr–Mo orthopedic implant alloys: Nitrogen-enhanced nanostructural evolution and its effect on phase stability, *Acta Biomater.* 9 (2013) 6259–6267. doi:10.1016/j.actbio.2012.12.013.
- [9] Y. Koizumi, S. Suzuki, K. Yamanaka, B.-S. Lee, K. Sato, Y. Li, S. Kurosu, H. Matsumoto, A. Chiba, Strain-induced martensitic transformation near twin boundaries in a biomedical Co–Cr–Mo alloy with negative stacking fault energy, *Acta Mater.* 61

- (2013) 1648–1661. doi:10.1016/j.actamat.2012.11.041.
- [10] P. Huang, H. López, Strain induced  $\epsilon$ -martensite in a Co–Cr–Mo alloy: grain size effects, *Mater. Lett.* 39 (1999) 244–248. doi:10.1016/S0167-577X(99)00021-X.
- [11] A. Salinas-Rodríguez, The Role of the FCC-HCP Phase Transformation During the Plastic Deformation of Co-Cr-Mo-C Alloys for Biomedical Applications, in: *Cobalt-Base Alloy. Biomed. Appl.*, ASTM International, 100 Barr Harbor Drive, PO Box C700, West Conshohocken, PA 19428-2959, n.d.: pp. 108-108–14. doi:10.1520/STP14267S.
- [12] M. Béréš, C.C. Silva, P.W.C. Sarvezuk, L. Wu, L.H.M. Antunes, A.L. Jardini, A.L.M. Feitosa, J. Žilková, H.F.G. de Abreu, R.M. Filho, Mechanical and phase transformation behaviour of biomedical Co-Cr-Mo alloy fabricated by direct metal laser sintering, *Mater. Sci. Eng. A.* 714 (2018) 36–42. doi:10.1016/j.msea.2017.12.087.
- [13] J.J. de Damborenea, M.A. Larosa, M.A. Arenas, J.M. Hernández-López, A.L. Jardini, M.C.F. Ierardi, C.A. de C. Zavaglia, R.M. Filho, A. Conde, Functionalization of Ti6Al4V scaffolds produced by direct metal laser for biomedical applications, *Mater. Des.* 83 (2015) 6–13. doi:10.1016/j.matdes.2015.05.078.
- [14] G.A. Longhitano, M.A. Larosa, A.L. Jardini, C.A. de C. Zavaglia, M.C.F. Ierardi, Correlation between microstructures and mechanical properties under tensile and compression tests of heat-treated Ti-6Al-4 V ELI alloy produced by additive manufacturing for biomedical applications, *J. Mater. Process. Technol.* 252 (2018) 202–210. doi:10.1016/j.jmatprotec.2017.09.022.
- [15] Y. Kajima, A. Takaichi, N. Kittikundecha, T. Nakamoto, T. Kimura, N. Nomura, A. Kawasaki, T. Hanawa, H. Takahashi, N. Wakabayashi, Effect of heat-treatment temperature on microstructures and mechanical properties of Co–Cr–Mo alloys fabricated by selective laser melting, *Mater. Sci. Eng. A.* 726 (2018) 21–31. doi:10.1016/j.msea.2018.04.048.
- [16] L.E. Murr, E. Martinez, K.N. Amato, S.M. Gaytan, J. Hernandez, D.A. Ramirez, P.W. Shindo, F. Medina, R.B. Wicker, Fabrication of Metal and Alloy Components by Additive Manufacturing: Examples of 3D Materials Science, *J. Mater. Res. Technol.* 1 (2012) 42–54. doi:10.1016/S2238-7854(12)70009-1.
- [17] S.M. Gaytan, L.E. Murr, E. Martinez, J.L. Martinez, B.I. MacHado, D.A. Ramirez, F. Medina, S. Collins, R.B. Wicker, Comparison of microstructures and mechanical properties for solid and mesh cobalt-base alloy prototypes fabricated by electron beam melting, *Metall. Mater. Trans. A Phys. Metall. Mater. Sci.* 41 (2010) 3216–3227. doi:10.1007/s11661-010-0388-y.

- [18] L. Novotný, M. Béreš, H.F.G. de Abreu, J. Zajac, W. Bleck, Thermal analysis and phase transformation behaviour during additive manufacturing of Ti–6Al–4V alloy, *Mater. Sci. Technol.* 35 (2019) 846–855. doi:10.1080/02670836.2019.1593669.
- [19] A. Takaichi, Suyalatu, T. Nakamoto, N. Joko, N. Nomura, Y. Tsutsumi, S. Migita, H. Doi, S. Kurosu, A. Chiba, N. Wakabayashi, Y. Igarashi, T. Hanawa, Microstructures and mechanical properties of Co-29Cr-6Mo alloy fabricated by selective laser melting process for dental applications, *J. Mech. Behav. Biomed. Mater.* 21 (2013) 67–76. doi:10.1016/j.jmbbm.2013.01.021.
- [20] Y. Kajima, A. Takaichi, T. Nakamoto, T. Kimura, Y. Yogo, M. Ashida, H. Doi, N. Nomura, H. Takahashi, T. Hanawa, N. Wakabayashi, Fatigue strength of Co–Cr–Mo alloy clasps prepared by selective laser melting, *J. Mech. Behav. Biomed. Mater.* 59 (2016) 446–458. doi:10.1016/j.jmbbm.2016.02.032.
- [21] L. Hitzler, F. Alifui-Segbaya, P. Williams, B. Heine, M. Heitzmann, W. Hall, M. Merkel, A. Öchsner, Additive Manufacturing of Cobalt-Based Dental Alloys: Analysis of Microstructure and Physicomechanical Properties, *Adv. Mater. Sci. Eng.* 2018 (2018) 1–12. doi:10.1155/2018/8213023.
- [22] H.W. Lee, K.H. Jung, S.K. Hwang, S.H. Kang, D.K. Kim, Microstructure and mechanical anisotropy of CoCrW alloy processed by selective laser melting, *Mater. Sci. Eng. A.* 749 (2019) 65–73. doi:10.1016/j.msea.2019.02.013.
- [23] N.P. Calta, J. Wang, A.M. Kiss, A.A. Martin, P.J. Depond, G.M. Guss, V. Thampy, A.Y. Fong, J.N. Weker, K.H. Stone, C.J. Tassone, M.J. Kramer, M.F. Toney, A. Van Buuren, M.J. Matthews, An instrument for in situ time-resolved X-ray imaging and diffraction of laser powder bed fusion additive manufacturing processes, *Rev. Sci. Instrum.* 89 (2018). doi:10.1063/1.5017236.
- [24] C. Kenel, D. Grolimund, X. Li, E. Panepucci, V.A. Samson, D.F. Sanchez, F. Marone, C. Leinenbach, In situ investigation of phase transformations in Ti-6Al-4V under additive manufacturing conditions combining laser melting and high-speed micro-X-ray diffraction, *Sci. Rep.* 7 (2017) 1–10. doi:10.1038/s41598-017-16760-0.
- [25] R.T. Smith, T. Lolla, D. Gandy, L. Wu, G. Faria, A.J. Ramirez, S.S. Babu, P.M. Anderson, In situ X-ray diffraction analysis of strain-induced transformations in Fe- and Co-base hardfacing alloys, *Scr. Mater.* 98 (2015) 60–63. doi:10.1016/j.scriptamat.2014.11.003.
- [26] EOS, Material data sheet EOS CobaltChrome MP1, Munique, 2011.
- [27] L.C. Zhang, Surface Integrity of Materials Induced by Grinding, in: M.J. Jackson, J.P.

- Davim (Eds.), *Mach. with Abrasives*, Springer US, Boston, MA, 2011: pp. 245–267. doi:10.1007/978-1-4419-7302-3\_5.
- [28] F. Klocke, D. Welling, J. Dieckmann, Comparison of Grinding and Wire EDM Concerning Fatigue Strength and Surface Integrity of Machined Ti6Al4V Components, *Procedia Eng.* 19 (2011) 184–189. doi:10.1016/j.proeng.2011.11.099.
- [29] B.D. Cullity, *Elements of x-ray diffraction*, Second, Addison-Wesley Publishing Company Inc, New York, 1978.
- [30] ASTM F75-12, Standard Specification for Cobalt-28 Chromium-6 Molybdenum Alloy Castings and Casting Alloy for Surgical Implants, *ASTM Int.* (2014) 1–4. doi:10.1520/F0075-12.2.
- [31] ASTM B962-17, Standard Test Methods for Density of Compacted or Sintered Powder Metallurgy (PM) Products Using Archimedes' Principle, *ASTM Int.* (2010) 1–6. doi:10.1520/B0962-17.
- [32] P.C. Collins, D.A. Brice, P. Samimi, I. Ghamarian, H.L. Fraser, Microstructural Control of Additively Manufactured Metallic Materials, *Annu. Rev. Mater. Res.* 46 (2016) 63–91. doi:10.1146/annurev-matsci-070115-031816.
- [33] S. Gorsse, C. Hutchinson, M. Gouné, R. Banerjee, Additive manufacturing of metals: a brief review of the characteristic microstructures and properties of steels, Ti-6Al-4V and high-entropy alloys, *Sci. Technol. Adv. Mater.* 18 (2017) 584–610. doi:10.1080/14686996.2017.1361305.
- [34] K. Yamanaka, M. Mori, S. Sato, A. Chiba, Stacking-fault strengthening of biomedical Co-Cr-Mo alloy via multipass thermomechanical processing, *Sci. Rep.* 7 (2017) 1–13. doi:10.1038/s41598-017-10305-1.
- [35] B. Song, S. Dong, S. Deng, H. Liao, C. Coddet, Microstructure and tensile properties of iron parts fabricated by selective laser melting, *Opt. Laser Technol.* 56 (2014) 451–460. doi:10.1016/j.optlastec.2013.09.017.
- [36] H.K.D.H. Bhadeshia, S.R. Honeycombe, *The Strengthening of Iron and its Alloys*, in: *Steels*, 4th ed., Elsevier, 2006: pp. 17–38. doi:10.1016/B978-075068084-4/50004-2.
- [37] W. Wang, F. Yuan, P. Jiang, X. Wu, Size effects of lamellar twins on the strength and deformation mechanisms of nanocrystalline hcp cobalt, *Sci. Rep.* 7 (2017) 9550. doi:10.1038/s41598-017-09919-2.
- [38] N. Tsuchida, Y. Morimoto, T. Tonan, Y. Shibata, K. Fukaura, R. Ueji, Stress-Induced Martensitic Transformation Behaviors at Various Temperatures and Their TRIP Effects in SUS304 Metastable Austenitic Stainless Steel, *ISIJ Int.* 51 (2011) 124–129.

- doi:10.2355/isijinternational.51.124.
- [39] N. Tsuchida, Y. Yamaguchi, Y. Morimoto, T. Tonan, Y. Takagi, R. Ueji, Effects of Temperature and Strain Rate on TRIP Effect in SUS301L Metastable Austenitic Stainless Steel, *ISIJ Int.* 53 (2013) 1881–1887. doi:10.2355/isijinternational.53.1881.
- [40] W.S. Park, M.S. Chun, M.S. Han, M.H. Kim, J.M. Lee, Comparative study on mechanical behavior of low temperature application materials for ships and offshore structures: Part I-Experimental investigations, *Mater. Sci. Eng. A.* 528 (2011) 5790–5803. doi:10.1016/j.msea.2011.04.032.
- [41] A.A. Lebedev, V.V. Kosarchuk, Influence of phase transformations on the mechanical properties of austenitic stainless steels, *Int. J. Plast.* 16 (2000) 749–767. doi:10.1016/S0749-6419(99)00085-6.
- [42] Z. Li, C.C. Tasan, K.G. Pradeep, D. Raabe, A TRIP-assisted dual-phase high-entropy alloy: Grain size and phase fraction effects on deformation behavior, *Acta Mater.* 131 (2017) 323–335. doi:10.1016/j.actamat.2017.03.069.
- [43] X. Wu, N. Tao, Y. Hong, J. Lu, K. Lu,  $\gamma \rightarrow \epsilon$  martensite transformation and twinning deformation in fcc cobalt during surface mechanical attrition treatment, *Scr. Mater.* 52 (2005) 547–551. doi:10.1016/j.scriptamat.2004.12.004.
- [44] R.T. Smith, Development of a Nitrogen-Modified Stainless-Steel Hardfacing Alloy, The Ohio State University, 2015.

## 4.2 Bloco 1.2 – Deformation-induced martensitic transformation in Co-28Cr-6Mo alloy produced by laser powder bed fusion: comparison surface vs. bulk

(<https://doi.org/10.1016/j.addma.2021.102100>)

L.H.M. Antunes<sup>a</sup>, J.J. Hoyos<sup>b</sup>, T.C. Andrade<sup>c</sup>, P.W.C. Sarvezuk<sup>d</sup>, L. Wu<sup>e</sup>, J.A. Ávila<sup>f</sup>, J.P. Oliveira<sup>g</sup>, N. Schell<sup>j</sup>, A.L. Jardini<sup>h</sup>, J. Žilková<sup>i</sup>, P.F. da Silva Farina<sup>a</sup>, H.F.G. Abreu<sup>c</sup>, M. Bérés<sup>c,h</sup>

<sup>a</sup> School of Mechanical Engineering, University of Campinas, Rua Mendeleev, 200, 13083-860, Campinas, SP, Brazil

<sup>b</sup> Department of Mechanical Engineering, Faculty of Engineering, University of Buenos Aires. Av. Paseo Colón 850, (C1063ACV), CA Buenos Aires, Argentina

<sup>c</sup> Department of Metallurgical and Materials Engineering, Federal University of Ceará, Av. Humberto Monte, 60445-554, Fortaleza, CE, Brazil

<sup>d</sup> Department of Physics, Federal University of Technology - Paraná, Via Rosalina Maria dos Santos, 1233, 87301899 Campo Mourão, Brazil

<sup>e</sup> National Laboratory of Synchrotron Light – LNLS, CNPEM, R. Giuseppe Máximo Scolfaro 10000, 13083-970, Campinas, SP, Brazil

<sup>f</sup> UNESP São Paulo State University, São João da Boa Vista, SP, Brazil

<sup>g</sup> Department of Mechanical and Industrial Engineering, NOVA University of Lisbon, 2829-516 Caparica, Lisbon, Portugal

<sup>h</sup> National Institute of Biofabrication, Faculty of Chemical Engineering, University of Campinas, Av. Albert Einstein 500, 13083-852, Campinas, SP, Brazil

<sup>i</sup> Department of Electrical Engineering and Mechatronics, Technical University of Košice, Letná 9, 042 00 Košice, Slovak Republic

<sup>j</sup> Helmholtz-Zentrum Geesthacht, Institute of Materials Research, Max-Planck-Str. 1, Geesthacht 21502, Germany

Keywords: CoCrMo alloy, martensitic phase transformation, *in-situ* synchrotron X-Ray diffraction, peak broadening, variant selection

<sup>1</sup>**Statement on Conflicts of Interest:** One of the authors of this article is part of the Editorial Board of the journal. To avoid potential conflicts of interest, the responsibility for the editorial and peer-review process of this article lies with the journal's other editors. Furthermore, the authors of this article were removed from the peer review process and had no, and will not have any access to confidential information related to the editorial process of this article.

### **Abstract**

The wear resistance of the biomedical low-carbon Co-28Cr-6Mo (wt.-%) alloy is mostly determined by the onset and magnitude of the face-centered cubic to hexagonal close-packed deformation-induced martensitic phase transformation. In metal-on-metal joint bearings, local plastic deformation occurs on the surface and in the subsurface regions. This can cause deformation-assisted structural changes in the material, such as mechanical twinning and/or martensitic transformation. In the present work, we report the structural transition on the surface and bulk of a laser powder bed fusion additively manufactured Co-28Cr-6Mo alloy in response to externally imposed loading. This study was possible using synchrotron X-ray diffraction at two different energy levels. Our results revealed that from tensile deformation to fracture, the phase transformation kinetics and magnitude were marginally higher on the surface. During transformation,  $\{200\}_{\text{FCC}}$  peak broadening was observed in the bulk and this was attributed to stacking fault accumulation.

## 1. Introduction

Additive manufacturing (AM) techniques, such as electron beam and/or laser powder bed fusion, are increasingly being employed to fabricate biomedical implants and dental components from Co-28Cr-6Mo precursor powders [1–3]. High wear resistance and high mechanical strength are two crucial criteria for alloys used for metal-on-metal joint replacements. When two bearing surfaces slide against each other, the load is carried by several asperities rather than across the entire surface [4,5]. Under high local contact stresses, these asperities can be plastically deformed and eventually torn off, producing particulate wear debris that can lead to wear abrasion [4]. The release of debris can cause adverse reactions, including metal hypersensitivity, inflammation, osteolysis, carcinogenicity, and neuropathy [6]. Owing to its high mechanical strength and wear resistance, the low-carbon Co-28Cr-6Mo (wt.-%) alloy, which complies with the ASTM F-75 standard, is the preferred alloy for articulating surfaces in joint replacements. The high strength and good wear resistance of this alloy system are attributed to the deformation-induced martensitic transformation from face-centered cubic (FCC) to hexagonal close-packed (HCP) [7–10]. Henceforth, the FCC and HCP phases are also referred to  $\gamma$  and  $\epsilon$ , respectively.

The  $\gamma/\epsilon$  interfaces formed during the phase transformation act as barriers for dislocation gliding and suppress strain localization. During displacive martensitic transformation, the applied stress state can bias the crystallographic variant of the product phase from the parent phase [11]. Below 850°C, the Co-28Cr-6Mo alloy has a negative stacking fault energy [12,13] and is therefore susceptible to deformation-induced martensitic transformation that can take place on the surface and in the subsurface layers in addition to the bulk.

Compared to materials fabricated by conventional processing routes, in the laser powder bed fusion (LPBF) process, superior mechanical properties and unique microstructural features are attained. This is mainly attributed to the fast solidification and high cooling rates ( $\sim 10^5$ - $10^6$  K/s) [14] of the melt pool. Such non-equilibrium conditions lead to formation of small grains (10-100  $\mu\text{m}$ ) containing ultrafine solidification cells ( $< 1 \mu\text{m}$ ) which are surrounded by dense dislocation walls contributing to mechanical strengthening [15,16]. In addition, Wang *et al.* [14] reported that in Co-Cr-Mo alloys fabricated via LPBF process, 95 vol.-% of athermal HCP phase was achieved. The high volume fraction of HCP phase was attributed to high density of dislocations and stacking faults formed by non-equilibrium rapid solidification. In contrast, cast material with an identical chemical composition attained such volume fraction of HCP phase after heat treatment conducted. However, the authors did not report on the procedure used for

the sample preparation. Therefore, the high volume fraction of HCP phase observed in their LPBF as-built specimen can be caused by deformation-induced martensitic transformation. For example, conventional metallographic preparation procedure involves grinding and mechanical polishing which causes a plastic deformation of the surface/sub-surface regions. Such deformation can locally promote the FCC  $\rightarrow$  HCP phase transformation. Therefore, the high volume fraction of HCP phase in the as-built specimen reported Wang *et al.* [14] can be caused by deformation-induced martensitic transformation originated from the metallographic preparation of samples.

Lu *et al.* [15] pointed out that the accumulation of the residual stress during the LPBF process resulted in the generation of overlapping stacking faults embryos by dissociating of perfect dislocation into a pair of Shockley partial dislocations promoting formation of the HCP phase. In stainless steel, Freeman *et al.* [16] observed the presence of a highly metastable retained austenite originated from the LPBF process. This was not reported previously in alloys produced by conventional fabrication methods.

The displacive  $\gamma \rightarrow \epsilon$  phase transformation in the Co-28Cr-6Mo alloy follows the Shoji-Nishiyama (S-N) orientation relationship:  $\{111\}_\gamma // \{0001\}_\epsilon$  and  $\langle 1\bar{1}0 \rangle_\gamma // \langle 2\bar{1}\bar{1}0 \rangle_\epsilon$  and during this transformation, the austenitic grain can transform into twelve  $\epsilon$ -martensite variants [17]. These 12 variants originate from the initial parent  $\gamma$ -phase through a shear process. However, depending on the austenitic crystal orientation and its stress state, not all martensitic variants may occur. Bokros and Parker [18] found that favored martensite variants have habit planes that are nearly perpendicular to the active slip plane in  $\gamma$ . In addition, an external stress applied to the bulk specimen increases the lattice strain [19], which increases the driving force of the martensitic transformation. This can be related to the reduction of the Gibbs free energy of the martensitic transformation, contributing to the variant selection [11,20,21].

The extent of the  $\gamma \rightarrow \epsilon$  phase transformation during plastic deformation has recently been analyzed using synchrotron light sources [1,19,22]. In addition, variant selection analyzes were previously carried out on low stacking fault energy alloys [23,24]. However, these studies did not compare characteristics of both the phase transition and the variant selection occurring on the surface and in the bulk. This is unprecedented in obtaining the comprehension of material behavior during service.

Here, we present the results of *in situ* tensile loading experiments using two synchrotron light sources with different energy levels, which allowed us to probe both the surface and bulk microstructural evolution of the as-built parts. We have identified the onset and kinetics of the deformation-induced phase transition in addition to the rate of lattice strain accumulation in

both the bulk and the surface. Moreover, variant selection analysis revealed differences between the bulk and surface regions.

## 2. Material and methods

### 2.1 Material

MP1 alloy powder feedstock (EOS GmbH, Krailling, Germany), in compliance with the ASTM F-75 standard, was used to prepare tensile test specimens using an EOSINT M280 selective laser melting machine (EOS GmbH, Krailling, Germany). The machine was operated in a nitrogen atmosphere using standard process parameters for the MP1 alloy. Two specimens were fabricated for conventional tensile testing, and two samples were produced for *in situ* synchrotron X-ray measurements under load application. The cross-sectional areas of samples for conventional tensile testing and synchrotron X-ray diffraction load experiments were  $6 \times 2 \text{ mm}^2$  and  $3.96 \times 1.50 \text{ mm}^2$ , respectively. Additional experimental details can be found in a previous study [19]. The chemical composition (wt.-%) of the produced samples was 27.89Cr-6.27Mo-0.72Mn-0.62Si-0.32Fe-0.1Ni-0.14C-0.14N, balance Co. The metallic elements were determined by a PANalytical Axios X-ray fluorescence spectrometer, and the carbon and nitrogen contents were determined by the combustion infrared detection technique (LECO CS844 analyzer) and by the inert gas fusion technique (LECO TC400 analyzer), respectively.

Yamanaka et al. [25,26] reported that a nitrogen addition to the Co-28Cr-6Mo alloy plays a crucial role in the athermal and deformation-induced HCP phase nucleation and, consequently contributes to the  $\gamma$  phase stabilization. Due to fact that a nitrogen atmosphere was used in the build process, a nitrogen pickup, *i.e.* 0.14 wt.-%, occurred during the fabrication of the samples. It is to be noted that, the protective nitrogen atmosphere was maintained steady throughout the process.

One could speculate that there is a variation of the nitrogen content from the surface to the inner bulk part. However, the nitrogen diffusivity along the specimen can be neglected. This is because, differently from other powder bed fusion techniques such as electron beam melting, the LPBF process does not use preheating of the powder bed or any kind of heat treatment during the fabrication. Although the build plate was pre-heated to  $80^\circ\text{C}$ , there is no sufficient thermal energy to significantly activate the nitrogen diffusion from one region to another along the sample being produced. Therefore, we have assumed that the nitrogen content at the surface is identical with that in the inner bulk part.

## 2.2 Tensile deformation

Tensile test specimens with a cross section of  $6 \times 2 \text{ mm}^2$  and 32 mm in gauge length, were deformed at room temperature in a strain control mode to 4% plastic strain on an MTS 810–FlexTest 40 servo-hydraulic testing machine. The strain rate used was  $5 \times 10^{-3} \text{ s}^{-1}$ , and the average strain over a gauge length of 25 mm was recorded using an MTS 632.24C-50 extensometer. Mechanical properties including yield stress, ultimate tensile strength, and elongation at break, were obtained from tensile tests using experimental details reported in a previous paper [19].

Because the alloy of concern exhibits work hardening, the side surfaces of the fabricated tensile specimens were electropolished before tensile deformation. Electropolishing was performed using Struers Lectropol-5 equipment at 25 °C under 20 V tension using a solution of 10% perchloric acid in acetic acid. The surfaces of the deformed specimens were then subjected to microstructural characterization without the need for additional metallographic preparation. The bulk microstructure was obtained from the deformed tensile test specimen with 2 mm in thickness that was electropolished to a distance 1 mm from the surface.

## 2.3 Microstructural characterization

The electropolished as-built and deformed tensile test specimens were examined via field emission gun scanning electron microscopy (FEG-SEM) using FEI 650 and FEI 450 microscopes that were both fitted with electron backscattered diffraction (EBSD) detectors (Nordlys, Oxford Instruments). The acceleration voltage used to acquire the EBSD maps was 15 kV and the step size was 0.1  $\mu\text{m}$ .

For the nanoscale characterization, transmission electron microscopy (TEM) was used. Disc specimens that were 3 mm in diameter were cut from  $\sim 100 \mu\text{m}$  thick electrolytically thinned foils taken from both the as-built and 4% deformed tensile test specimens. The disc specimens were then further electropolished to obtain electron transparency using a Struers Tenupol-3 apparatus with the electrolyte and conditions mentioned previously. A JEOL FX2100 transmission electron microscope operated at 200 kV was utilized to acquire bright field micrographs.

## 2.4 Synchrotron X-ray diffraction experiments

Tensile test specimens with cross section of  $3.96 \times 1.5 \text{ mm}^2$  and 4.5 mm in gauge length were used in synchrotron X-ray diffraction systems that can impose mechanical load. The load

was applied perpendicularly to the specimen's build direction at a strain rate of  $10^{-3} \text{ s}^{-1}$  while simultaneously acquiring X-ray diffraction patterns. Two synchrotron X-ray sources were utilized in this study, XRD1/XTMS beamline at the Brazilian Synchrotron Light Laboratory (LNLS) at the National Center for Research in Energy and Materials, Campinas/Brazil and P07/Petra III beamline at the German Electron Synchrotron (DESY), Hamburg/Germany. The beam size at the XRD1/XTMS and at the P07/Petra III beamline was  $2 \times 2 \text{ mm}^2$  and  $1 \times 1 \text{ mm}^2$ , respectively. In both experimental trials, the beam size was larger than the average grain size measured in our specimens (i.e.  $\sim 40 \text{ }\mu\text{m}$ ).

1. The bulk crystal structure evolution was evaluated in transmission mode using high-energy X-ray diffraction at a wavelength of  $0.1423 \text{ \AA}$  (87 kV). This ensures that several layers were captured and therefore, bulk information was obtained. Diffraction data were collected for 60 s using a 2D Mar345 detector, while the load was held constant at  $\sim 2.5\%$  strain increments up to fracture. The strain value was determined from the crosshead displacement.
2. The crystal structures on the surface and in the subsurface regions were measured using X-ray diffraction at a wavelength of  $1.034 \text{ \AA}$  (12 kV). Tensile loading experiments were performed by mounting the samples in a loaded rig of the GLEEBLE 3500 thermomechanical simulator, and the strain was measured using a laser extensometer. The load was held constant for 400 s at  $\sim 2\%$  strain increments up to fracture, and diffraction patterns were simultaneously captured using two 1D Mythen detectors in the reflection mode.

To normalize the different energies from the synchrotron light sources, the full width at half maximum was calculated using the momentum transfer in reciprocal space ( $Q$ ):

$$Q = \frac{4\pi \sin \theta}{\lambda} \quad (1)$$

where  $\theta$  is the Bragg angle and  $\lambda$  is the wavelength, which is equal to  $0.142 \text{ \AA}$  and  $1.033 \text{ \AA}$  at beamlines P07/Petra III and XRD1/XTMS, respectively.

The lattice strain values ( $e$ ) of the  $\gamma_{\text{FCC}}$  were estimated using the Stokes and Wilson methods.

$$e = \frac{\beta}{4 \tan \theta} \quad (2)$$

$\beta$  is the full width at half maximum expressed in radians, and  $\theta$  is the Bragg angle [27].

The volume fractions of the  $\gamma$  and the  $\varepsilon$  phases were determined via Rietveld analysis using the FullProf software package. The space groups used in the refinement were  $Fm\bar{3}m$  for the  $\gamma$ -phase and  $P63/mmc$  for the  $\varepsilon$ -phase, respectively. The only correction of the preferred orientation was performed on  $\{111\}_\gamma$  planes, using the preferential plane parameter for this phase.

## 2.5. Variant selection analysis

The  $\gamma \rightarrow \varepsilon$  transformation takes place in every second  $(111)_\gamma$  plane that is displaced in the  $[11\bar{2}]_\gamma$  direction by  $a_\gamma/\sqrt{6}$  [18], causing the shear planes  $\{111\}_\gamma$  to be parallel to the  $\{0001\}_\gamma$  planes of the  $\varepsilon$ -martensite. Following these criteria, Patel-Cohen [17] developed a model to predict the interaction energy of  $\gamma \rightarrow \alpha$  phase transformation and, consequently, predict variant selection. Later, Humbert [29] described  $\gamma \rightarrow \alpha'$  a transition based on a two-step model with an intermediate phase ( $\varepsilon$ -martensite). Then, the  $\alpha'$ -martensite variant selection can be estimated from the  $\gamma \rightarrow \varepsilon \rightarrow \alpha'$  transformation. The two-step model has been omitted by several authors because the one-step model yielded the same results. However, Humbert's approach can be employed when the  $\varepsilon$ -martensite phase is of interest.

Kundu and Bhadeshia [21] showed that the Patel-Cohen [17] and Humbert [29] models differ by a factor of 0.5 because Humbert [29] assumed that the stress-strain relationship is elastic; however, the transformation strain is plastic. According to Patel-Cohen [17], the interaction energy can be written as

$$W = \sigma \epsilon \quad (3)$$

where  $\sigma$  is the macroscopic stress-imposed tensor and  $\epsilon$  is the transformation strain associated with the phase transformation. We used the Humbert model with a crystal reference frame to describe the phase transformation [30]. Therefore, for uniaxial stress, the interaction energy can be rewritten as:

$$W^{\gamma \rightarrow \varepsilon} = m \sigma_{11} \epsilon_{13} \quad (4)$$

where  $m$  is the Schmid factor for the  $\{111\}_\gamma \langle 112 \rangle_\gamma$  slip system,  $\sigma_{11}$  is the applied uniaxial stress, and  $\epsilon_{13}$  is the pure shear transformation strain associated with the transformation, where

$\epsilon_{13} = \epsilon_{31} = (2\sqrt{2})^{-1}$ . Thus, the selected variants for  $\epsilon$ -martensite are the variants with the highest Schmid factor. Finally, according to Humbert [29], only the variants with the maximum interaction energy were selected. Therefore, the variant with the highest energy was chosen, followed by the others that had energy in the range of 10% of the energy of this variant. This was the severity factor proposed by Humbert *et al.*[29].

### 3. Results and discussion

A typical textured columnar microstructure formed in the as-built sample is shown in EBSD Euler orientation map Figure 1. A single  $\gamma$ -phase was identified in this condition. It is to be noted that this map was collected from the surface of the as-built specimen prior to the plastic deformation. The 4 % plastic deformation applied to the specimens caused the  $\gamma \rightarrow \epsilon$  phase transformation and formation of slip traces aligned within columnar grains, Figure 2a and c. In addition, these figures revealed that the extent of transformation on the surface was greater than that in the bulk. Please note, that the EBSD maps of the bulk specimen were collected from the deformed tensile test specimen (2 mm in thickness) that was electropolished to the distance 1 mm from the surface. Hegele *et al.* [31] pointed out that the extent of martensitic transformation on the surface may be enhanced in the presence of oxides. However, the XRD analysis performed in the current work did not reveal the existence of oxides. Therefore, other factors discussed in the following sections are considered to boost the kinetics of martensitic transformation on the surface.

LPBF specimens present considerable residual stresses owing to the non-equilibrium solidification conditions in which the material experienced after each layer is deposited [32]. When subjected to strain, part of this residual stress is relieved by the deformation-induced martensitic transformation, leaving a residual plastic strain caused by the volume expansion resulting from the  $\gamma \rightarrow \epsilon$  phase transformation [33]. This is manifested by the increased values of kernel average misorientation (KAM), as presented in Figures 2b and d. The KAM values of the  $\epsilon$ -phase are lower and more evenly distributed in the bulk compared to the surface. The lower KAM values and their homogeneous distribution in the bulk (Figure 2d) indicate that the plastic strain occurring from the martensitic transformation is accommodated by more  $\gamma$  grains surrounding the newly nucleated  $\epsilon$ -phase. The higher degree of misorientation and its heterogeneous distribution at the surface (Figure 2b) is an indication that the plastic strain occurring from the martensitic transformation is accommodated by fewer  $\gamma$  grains surrounding the newly nucleated  $\epsilon$ -phase. Here, a heterogeneous stress field is produced near grain

boundaries owing to the grain boundary constraint and the impingement on the  $\epsilon$  plates from the neighboring grains [34].

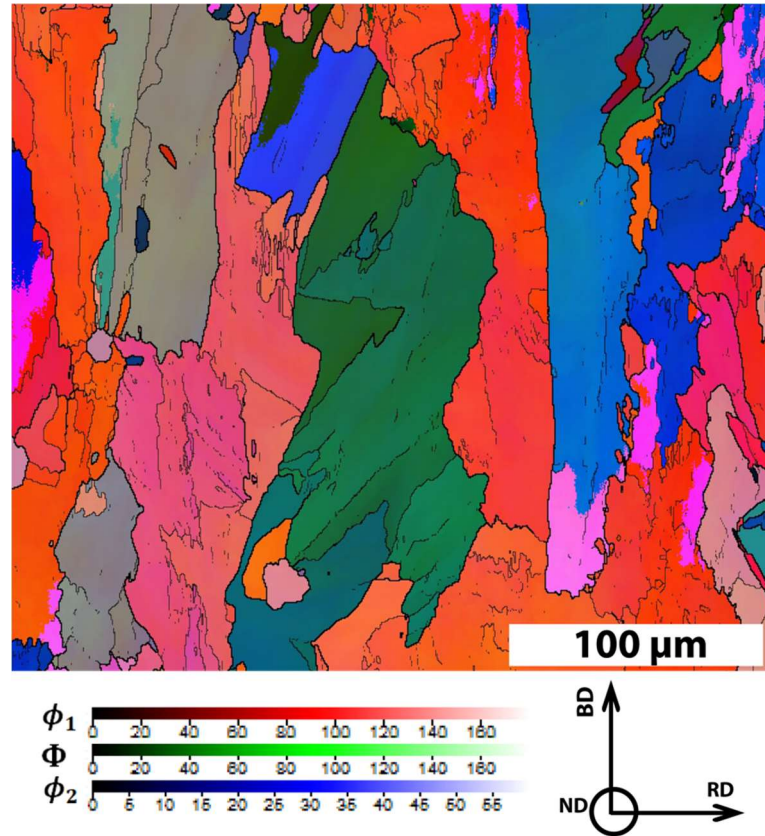


Figure 1 – EBSD Euler map revealing columnar grains in the as-built sample.

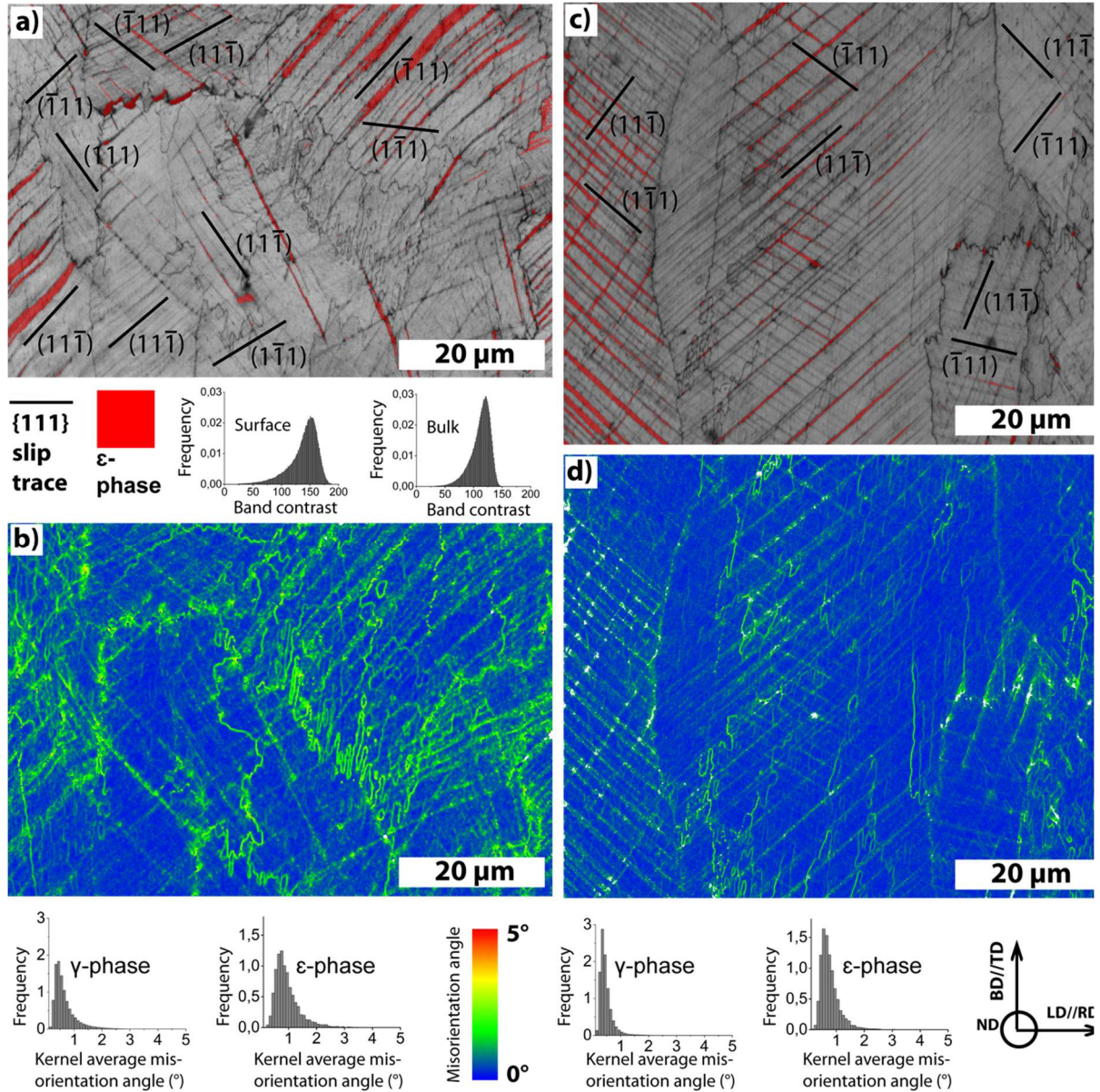


Figure 2 – EBSD phase and band contrast map collected after ~4% plastic deformation revealing the presence of deformation-induced  $\epsilon$  martensite on the surface a) and in bulk, c), respectively. In these figures  $\{111\}$  slip traces are depicted. The corresponding kernel average misorientation maps are shown in b) and d). BD indicates build direction and LD indicates load direction.

Variant selection analysis was carried out using EBSD maps acquired from the bulk and the surface after tensile loading (refer to Figure 3). The orientation maps from the surface and bulk are shown in Figure 3a and d, respectively.

Figure 3b shows the experimentally determined pole figures for  $\epsilon$ -martensite from the subset depicted in Figure 3a. Here, only one  $\epsilon$ -martensite crystallographic variant was observed. Using a set of experimentally determined Euler angles of the  $\gamma$ -phase in the boxed region in Figure 3a,  $\epsilon$ -martensite variants were calculated using the Humbert model presented in Section 2.5. The Euler angles used for the Humbert model were  $[297.8^\circ, 46.0^\circ, 28.9^\circ]$ , and the resulting

pole figures are shown in Figure 3c. One can note a good match between the experimentally determined and simulated pole figures (Figure 3b and c). The same approach was applied to the bulk specimen, revealing good agreement between the experimentally determined and simulated pole figures (Figure 3e and f).

Table A.1 (Appendix A) shows the crystallographic variants for  $\varepsilon$ -martensite with orientation, Schmid factor, and interaction energy for each slip system. The selected variants were those with highest Schmid factors for Shockley partial dislocations. The experimental results of selected crystallographic variants and observed slip traces coincide with calculation results of the interaction energy for the martensitic transformation and Schmid factor values (detailed in Table A1).

Comparing the crystallographic variants present in bulk and surface, it was observed that the latter showed only one variant in the analyzed region, while in the bulk specimen, two variants were present. During the selection of certain crystallographic variants, variant shape deformation relieves the applied external stress.

In general, the deformation-induced martensitic transformation in FCC alloys is governed by the motion of Shockley partial dislocation pairs consisting of leading and trailing partials with different Schmid factors. The calculation of Schmid factors for perfect dislocation ( $m_p$ ) in addition to leading partials ( $m_l$ ) and trailing partials ( $m_t$ ) showed the following: in most grains in which  $\varepsilon$ -martensite was detected, the Schmid factors of the leading partials (dislocations that form the  $\varepsilon$ -martensite) were lower than those of the trailing partials. Our analysis also revealed that the activated slip at the onset of plasticity was limited to the primary slip on one of the slip systems with the highest Schmid factors. Therefore, the  $\gamma \rightarrow \varepsilon$  transformation is governed by the critical resolved shear stress ( $\tau_{CRSS}$ ) to activate the slip. Lee *et al.* [23] attributed this phenomenon to the negative-stacking fault energy in this alloy system. Consequently, isolated partial dislocations are preferred for the motion of the leading-trailing Shockley partial pairs. However, no  $\varepsilon$ -martensite variants were observed to be parallel to the load direction. This is because this orientation would decrease the resolved shear stress and then suppress the formation of  $\varepsilon$ -martensite variants [35].

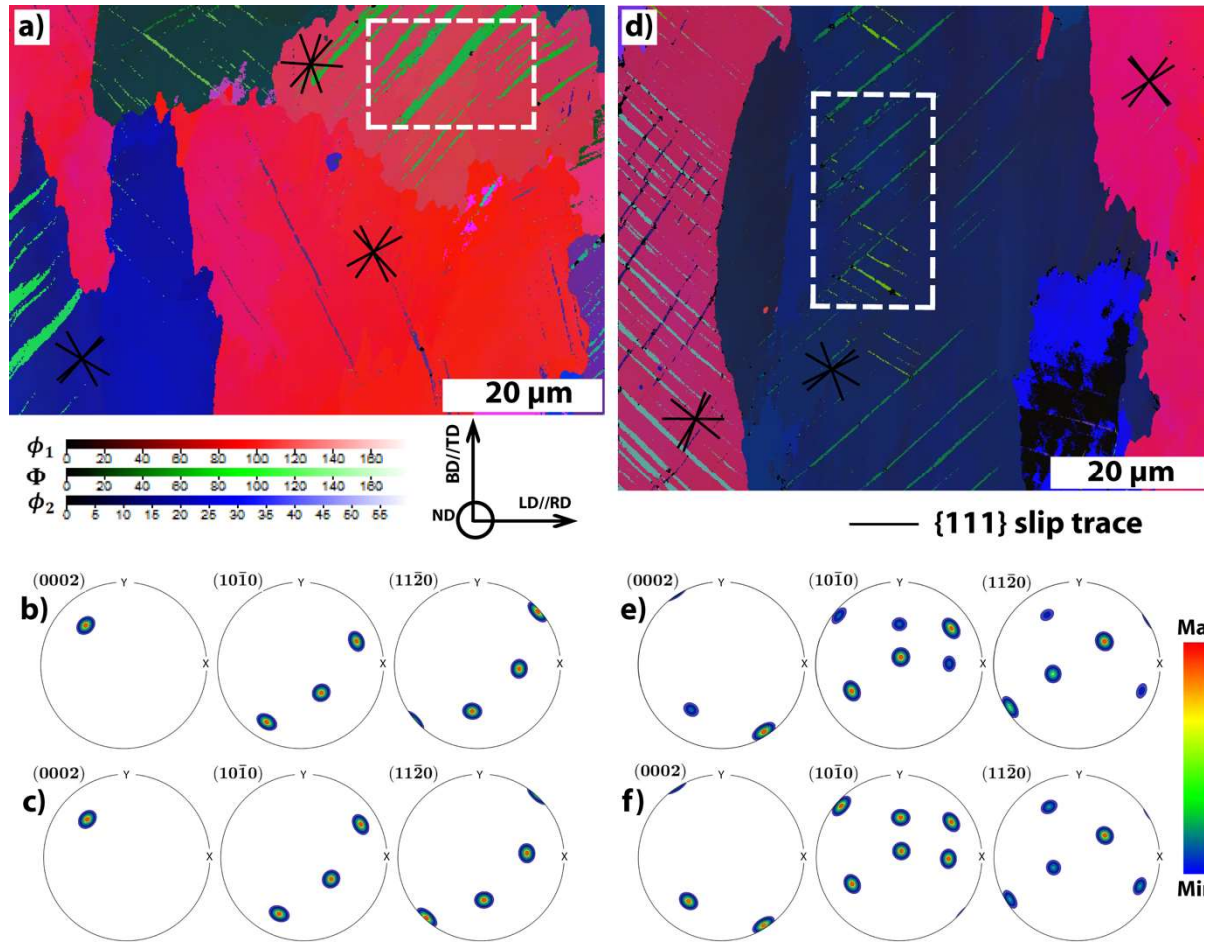


Figure 3 – Euler orientation maps collected from: a) surface and d) bulk. b) and e) are experimentally determined (0002), (10 $\bar{1}$ 0), and (11 $\bar{2}$ 0) pole figures of  $\epsilon$  variants from boxed regions in a) and d) for surface and bulk specimens, respectively. c) and f) are calculated (0002), (10 $\bar{1}$ 0), and (11 $\bar{2}$ 0) pole figures of  $\epsilon$  variants from boxed regions in a) and d) for surface and bulk specimens, respectively. BD indicates build direction and LD indicates load direction.

Zhanget *al.* [34] reported that the formation of variants with lower Schmid factors becomes more prominent as the plastic deformation proceeds. Other factors, such as local stress concentration from martensite plates and inhomogeneous stresses near the boundary (as revealed in Figures 2b and d) may affect the deformation mode and variant selection [36].

A bright-field TEM image of the bulk specimen prior to the deformation is shown in Figure 4a. Fringe contrasts from pre-existing stacking faults and their intersections can be observed. The majority of fringes terminated at the intersections of the  $\{111\}_\gamma$  plane. The alloy of concern has a negative SFE [12] and is, therefore, susceptible to formation of stacking faults formation. Figure 4b shows a bright-field TEM image of a sample subjected to  $\sim 4\%$  plastic deformation. The presence of deformation-induced  $\epsilon$ -martensite (depicted with an arrow) was observed in this condition. Under loading, the dislocation glide is inherently suppressed owing to the low stacking fault energy of the alloy. Consequently, slip is highly localized on pre-

existing and strain-induced stacking faults with different crystallographic orientations. These regions form various variants of deformation-induced  $\varepsilon$ -martensite in the loaded sample, as observed in Figure 3d. The measured misorientation angle between the two crystallographic variants of  $\varepsilon$ -martensite was  $\sim 71^\circ$ . The  $\gamma \rightarrow \varepsilon$  transformation follows the S-N orientation relationship:  $\{111\}_\gamma // \{0001\}_\varepsilon$  and  $\langle 1\bar{1}0 \rangle_\gamma // \langle 2\bar{1}\bar{1}0 \rangle_\varepsilon$ . Therefore, different  $\varepsilon$ -martensite variants formed on one of the  $\{111\}_\gamma$  planes can be obtained through the rotation of the basal plane by  $71^\circ$  in the corresponding  $\langle 011 \rangle_\gamma$  direction [37]. With increasing load, the  $\varepsilon$ -martensite plates deform plastically, leading to deviations in the misorientation angles.

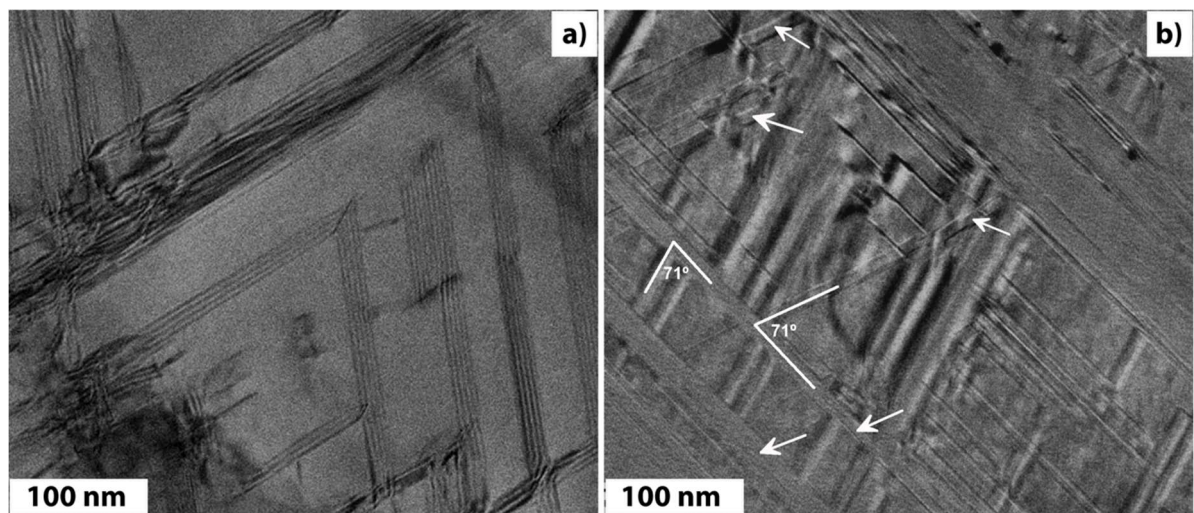


Figure 4 – Bright-field TEM micrographs showing stacking faults in undeformed specimen a) and formation of deformation-induced  $\varepsilon$ -martensite (depicted with arrows) after  $\sim 4\%$  plastic deformation in b).

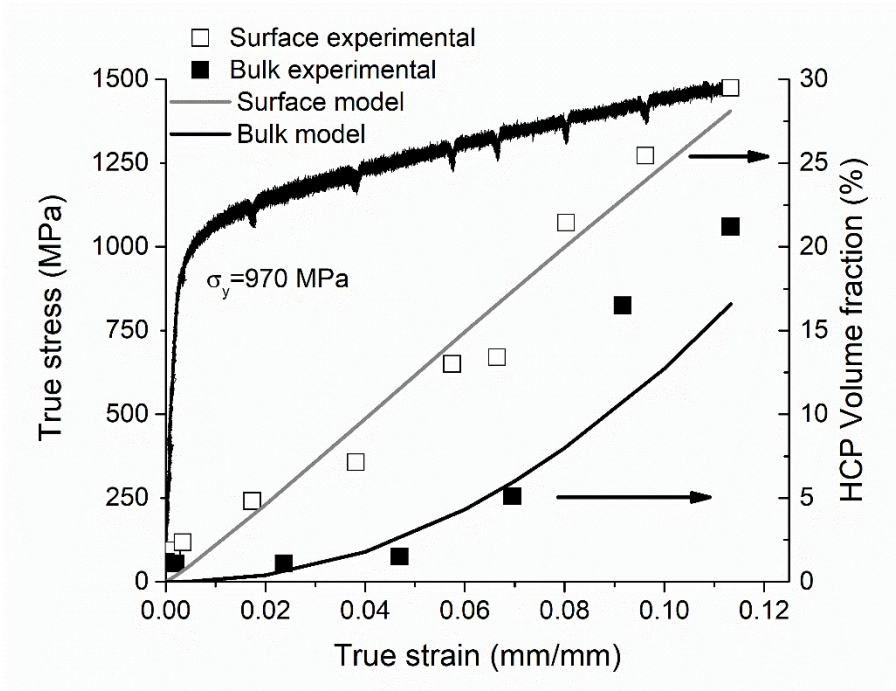


Figure 5 – True stress–true strain curve. Experimental and simulated kinetics of deformation-induced  $\gamma \rightarrow \varepsilon$  phase transformation on the surface and in the bulk during tensile loading (beamline XTMS/LNLS Brazil and Petra III/DESY Germany).

The kinetics of the  $\varepsilon$ -phase during tensile deformation in bulk and on the surface were followed via the time-resolved XRD technique, using two synchrotron light sources, as shown in Figure 5. At the beginning of the loading, a single-phase  $\gamma$ -phase was identified. As the true strain increased, the  $\gamma \rightarrow \varepsilon$  phase transformation started to occur. With increasing strain, the volumetric fraction of the  $\varepsilon$ -phase increased, and at a true strain of 0.115, it reached 21 and 30 vol.-% at the surface and in bulk, respectively.

The kinetics of the  $\gamma \rightarrow \varepsilon$  phase martensitic transformation, presented in Figure 5, was estimated using Equation 5, which was proposed by Choi *et al.* [38]. Thus, the deformation-induced phase transformation acts as an effective relaxation process to relieve the internal strain energy accumulation during inelastic deformation.

$$V_{\varepsilon} = V_s(1 - \exp(-\beta\varepsilon^n)) \quad (5)$$

where  $V_{\varepsilon}$  is the volume fraction of  $\varepsilon$ -martensite,  $V_s$  is the saturation volume fraction of  $\varepsilon$ -martensite,  $\beta$  is a kinetic parameter that characterizes the stability of austenite,  $n$  represents the formation rate of nucleation sites, and  $\varepsilon$  is the strain (true or engineering).

Since the material of concern is composed of grains with average size of 40  $\mu\text{m}$ , low energy X-ray results can be affected by surface effects, whereas high-energy results are not. In

addition, calculation results of kinetics parameter,  $\beta$ , that characterizes the stability of austenite during martensitic transformation using model proposed by Choi *et al.* [38], Table1, revealed that the surface has a lower value of  $\beta$  than that of the bulk. This suggests that the surface has lower austenite stability when compared to the bulk.

With the use of synchrotron X-ray diffraction in transmission mode, bulk information averaged over the thickness of the sample was acquired allowing a volumetric evaluation of the bulk material free from the surface effects. However, this information complements that obtained by surface characterization methods such as low energy X-ray diffraction or electron microscopy methods. Surface effects on martensitic transformation of several engineering alloys are well-know by now [39]. However, bulk residual stresses also play a role in this transformation. The issue is that LPBF process promotes the development of complex residual stresses that are not homogenous along the part. These non-homogenous residual stress patterns can then drastically modify the conditions of the martensitic transformation to occur. However, it is not possible to pin point yet what is the role of such residual stresses in the martensitic transformation. For this to be evaluated, an in-situ measurement during the LPBF process needs to be performed. This, however, is beyond scope of the present paper and such measurement will be subject of further work.

Table 1 – Kinetics parameters of martensitic transformation in the bulk and on the surface using model proposed by Choi *et al.* [38].

<i>Parameter</i>	$V_s$	$n$	$\beta$
<i>Surface</i>	1	1.12	3.77
<i>Bulk</i>	1	2.20	21.55

Figure 6a shows the surface relief after 4% plastic deformation on the polished surface. In addition, surface cracking and melt-pool boundaries are visible. Figure 6b shows the side surface slip traces produced by the intersection of the  $\{111\}$  slip planes with the polished side surface. These closely spaced slip steps produce facets with a lower pile-up height and coarsely spaced slip steps that produce higher pile-up heights. As shown on the left side of Figure 6b, the slip steps on the side surface indicate that unrelaxed pile-ups existed before the fracture. Therefore, the crack initiated at the piled-up dislocations on the surface toward the bulk. Figure 6b shows the fracture surface with the pile-up containing large slip steps, indicating a more ductile region in the bulk, as confirmed by the dimple structure along each slip step. The transformed  $\gamma$ -phase involves dense stacking faults, which effectively prevent dislocation movements in the  $\gamma$ -phase and contribute to the increase in the work-hardening rate [40]. Thus,

at the interface between the  $\gamma$  and  $\varepsilon$  phases, there is strain incompatibility, leading to a stress concentration in this region. This stress concentration acts as a source of nucleation and microcrack growth as the plastic deformation continues. Therefore, it is likely that fractures originated at the surface of the specimen, which is in agreement with the work of Koizumi *et al.* [12]. Figure 6 also revealed formation of micro cracks at columnar grain boundaries. Therefore, in the LPBF material, there is strong texture sensitivity for plastic deformation, fracture initiation and formation of  $\varepsilon$ -martensite compared to that in equiaxed grains commonly observed in conventionally produced alloys (cast, forged and/or heat treated).

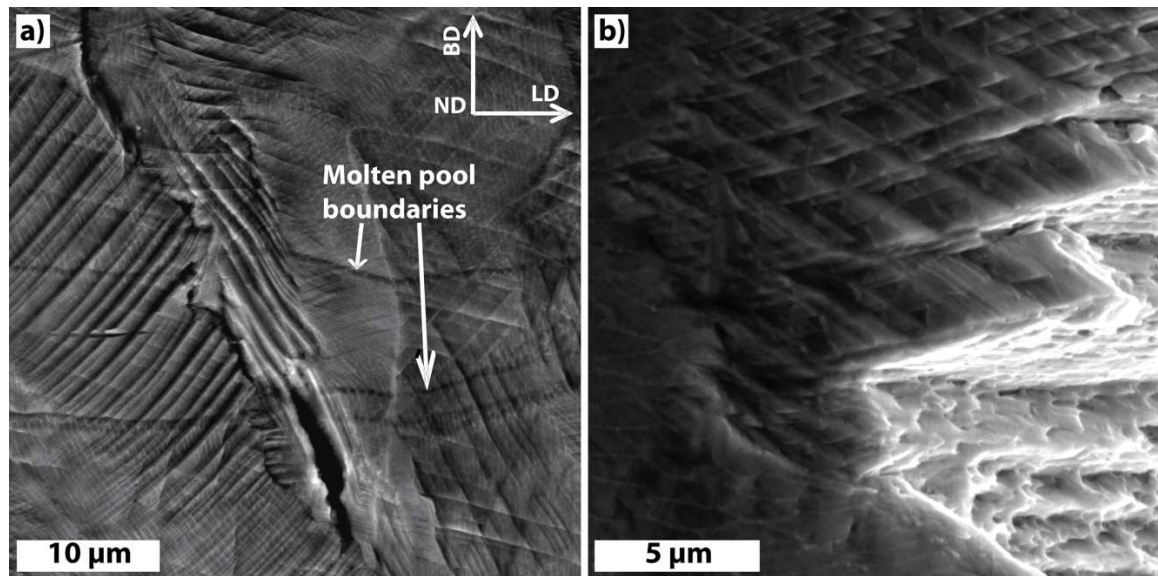


Figure 6 – a) Secondary electron micrographs acquired on the pre-polished side surface of the deformed tensile test specimen at a) distance of  $30\mu\text{m}$  from fracture and b) at the fracture. Please note that the micrograph shown in b) was collected at a  $\sim 15^\circ$  tilt angle. On left side of the image shown in b), pre-polished side surface of deformed tensile test specimen reveals pileups and slip traces produced by intersection of  $\{111\}$  slip planes with previously polished side surface. On right side of the micrograph, slip steps at pile-ups on fracture facets are shown. BD indicates build direction and LD indicates load direction.

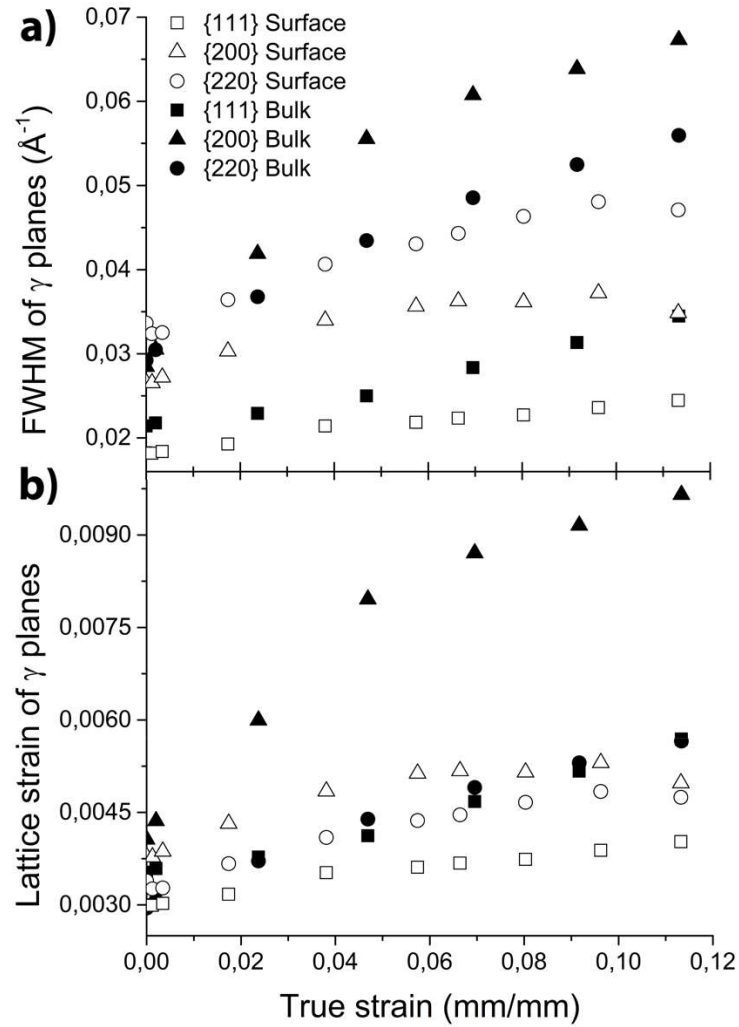


Figure 7 – a) Evolution of full width at half maximum (FWHM) as a function of true strain in tensile loaded specimen. Please note peak broadening in  $\{200\}_{\gamma}$  planes in bulk. b) Evolution of lattice strain in individual  $\gamma$  crystallographic planes as function of true strain in tensile loaded specimen.

On one hand, during tensile loading, significant peak broadening was observed in the  $\{200\}_{\gamma}$  planes of the bulk specimen (refer to Figure 7a). The peak broadening is caused by the accumulation of stacking faults and back stresses in the neighboring grains with increasing strain. Here, large stress fields are produced near the grain boundaries owing to the grain boundary constraint and the impingement of the  $\epsilon$  plates from the neighboring grains. On the other hand, no significant peak broadening was observed at the surface. Another reason for smaller  $\{200\}_{\gamma}$  peak broadening at the surface could be explained in terms of the enhanced martensitic transformation at the surface, Figure 5. In general, the  $\{200\}_{\gamma}$  peak is sensitive to dislocation density, causing more significant broadening. Mori *et al.* [41] argued that the  $\epsilon$ -martensite is formed by consuming dislocations in the  $\gamma$ -matrix. In their work, synchrotron X-ray diffraction line-profile analysis was employed to track formation of  $\epsilon$ -martensite and

evolution of dislocation density during tensile deformation of multi-pass hot rolled Co-Cr-Mo alloy. During initial stages of tensile loading, the increase of the integral breadth of line profile was attributed to the rise of the dislocation density in the  $\gamma$ -matrix. At 0.2% proof stress, the dislocation density reached a maximum and  $\varepsilon$ -martensite started to form. With progressing plastic deformation, the observed reduction in dislocation density was attributed to the consumption of the dislocations in the  $\gamma$ -matrix during formation of  $\varepsilon$ -martensite. Results obtained by Mori *et al.* [41] are consistent with results presented in Figure 7, where one can observe an increase in the FWHM of the plane  $\{200\}_\gamma$  in the initial stages of loading. With progressing loading, the rise in the FWHM can be associated with an increase in dislocation density. At the final stages of the plastic deformation, the FWHM starts to decrease, indicating the reduction of the dislocations density accompanied by formation of  $\varepsilon$ -martensite. One half of the Shockley partial pair marks the  $\varepsilon$ -phase, while the other half disappears at the surface, leaving behind a slip band. Indeed, because the surface of the specimen was polished prior to the plastic deformation, the formation of slip bands (and surface relief) on the deformed sample surface was observed (refer to Figures 2 and 6). Each band consists of a large number of slip steps equal to the Burgers vector  $b = \frac{1}{6} \langle 1\bar{2}1 \rangle$  on  $\{111\}$  closely spaced parallel slip planes. Dislocations near the surface can escape and therefore do not accumulate the same back stresses in neighboring grains. Therefore, no significant peak broadening was observed on the surface. For peak broadening, there is also an orientation dependence on the dislocation type [42,43].

In Figure 7b, it is possible to see the increase in lattice strain with increasing true strain for both the bulk and the surface. When comparing the surface to the bulk, the magnitude of the lattice strain was lower at the surface. The lattice strain is relieved by the formation of slip bands at the surface, as mentioned previously.

The higher lattice strain values contributed to the variant selection. Overall, the Gibb's energy ( $G$ ) in the transformation comprises its chemical ( $\Delta G_c$ ) and mechanical ( $\Delta G_m$ ) contributions. The interaction energy  $U$  (Equation 6) is a significant contributor to  $\Delta G_m$  and is a large fraction of the total  $\Delta G = \Delta G_c + \Delta G_m$ ; variant selection can occur and contribute to  $G$  minimization occurring at equilibrium [11,44].

$$U = \sigma_N \zeta + \tau s \quad (6)$$

Where  $\sigma_N$  is the stress component normal to the habit plane;  $\tau$  is the shear stress resolved on the habit plane in the direction of shear; and  $\zeta$  and  $s$  are, respectively, the normal and shear strains associated with the transformation.

#### 4. Conclusions

The characteristics of deformation-induced  $\gamma_{\text{FCC}} \rightarrow \epsilon_{\text{HCP}}$  phase transformation in a Co-28Cr-6Mo alloy fabricated by selective laser melting were investigated with two *in-situ* loading synchrotron-diffraction experiments. During monotonic tensile loading, different energy levels were employed to follow the phase transformation in the transmission mode (*i.e.*, in bulk) and reflection mode (*i.e.*, on the surface).

The following conclusions were drawn:

- 1- The accumulation rate of the  $\epsilon$ -phase is higher on the surface than in the bulk.
- 2- The formation of the  $\epsilon$ -phase is associated with perfect dislocation slip for isolated partial dislocations rather than by Shockley leading-trailing partials.
- 3- Although the  $\epsilon$ -phase is considered to improve the wear resistance in this alloy system, the  $\gamma/\epsilon$  interfaces are sites for crack initiation and propagation.
- 4- The  $\{200\}_{\gamma}$  peak broadening is associated with the accumulation of stacking faults with progressing strain.

#### Acknowledgments

The authors are grateful to Professor D. Dye from Imperial College London for his helpful discussions. The authors would like to acknowledge the experimental support of F.E. Montoro, Dr. C. Ospina, Dr. O.R. Bagnato, and Dr. A.L. Gobbi (projects SEM-26162, TEM-26161, LMF 20869) at the Brazilian Nanotechnology National Laboratory (LNNano). The assistance of J.L. Lisboa from Unicamp/Campinas with mechanical tests and Dr. J.R. de Barros Neto from Federal University of Piauí/Teresina with EBSD data analysis is also acknowledged.

Microstructural characterization of the specimens was performed at LNNano and the Central Analítica UFC/CT-INFRA-FINEP/Pro-Equipamentos-CAPES/CNPq-SisNano-MCTI 2019(Grant 442577/ 2019-2)-INCT-FUNCAP. This study used the resources of the Brazilian Synchrotron Light Laboratory (LNLS) (project 20170162), an open national facility operated by the Brazilian Center for Research in Energy and Materials for the Brazilian Ministry for Science, Technology, Innovations, and Communications.

This work was financed in part by the Coordenação de Aperfeiçoamento de Pessoal de Nível Superior, Brasil, Finance Code 001, and Fundação para a Ciência e a Tecnologia (FCT - MCTES) via the project UIDB/00667/2020 (UNIDEMI). The research leading to this result has

been supported by the project CALIPSOplus under the Grant Agreement 730872 from the EU Framework Programme for Research and Innovation HORIZON 2020 (proposal I-20160912).

## References

- [1] M. Béréš, C.C. Silva, P.W.C. Sarvezuk, L. Wu, L.H.M. Antunes, A.L. Jardini, A.L.M. Feitosa, J. Žilková, H.F.G. de Abreu, R.M. Filho, Mechanical and phase transformation behaviour of biomedical Co-Cr-Mo alloy fabricated by direct metal laser sintering, *Mater. Sci. Eng. A.* 714 (2018) 36–42. doi:10.1016/j.msea.2017.12.087.
- [2] Y. Okazaki, Effects of fine microstructures and precipitates of laser-sintered Co–28Cr–6Mo alloy femoral components on wear rate of UHMWPE inserts in a knee joint simulator, *J. Mech. Behav. Biomed. Mater.* 112 (2020) 103998. doi:10.1016/j.jmbbm.2020.103998.
- [3] B. Konieczny, A. Szczesio-Włodarczyk, J. Sokolowski, K. Bociong, Challenges of Co–Cr Alloy Additive Manufacturing Methods in Dentistry—The Current State of Knowledge (Systematic Review), *Materials (Basel)*. 13 (2020) 3524. doi:10.3390/ma13163524.
- [4] S.A. Brown, Synthetic Biomaterials for Spinal Applications, in: S.M. Kurtz, A.A.B.T.-S.T.H. Edidin (Eds.), *Spine Technol. Handb.*, Elsevier, Burlington, 2006: pp. 11–33. doi:10.1016/B978-012369390-7/50003-4.
- [5] M.A. Wimmer, J. Loos, R. Nassutt, M. Heitkemper, A. Fischer, The acting wear mechanisms on metal-on-metal hip joint bearings: In vitro results, *Wear*. 250–251 (2001) 129–139. doi:10.1016/S0043-1648(01)00654-8.
- [6] N.J. Hallab, J.J. Jacobs, Biologic effects of implant debris, *Bull. NYU Hosp. Jt. Dis.* 67 (2009) 182–188.
- [7] K. Yamanaka, M. Mori, Y. Koizumi, A. Chiba, Local strain evolution due to athermal  $\gamma \rightarrow \epsilon$  martensitic transformation in biomedical CoCrMo alloys, *J. Mech. Behav. Biomed. Mater.* 32 (2014) 52–61. doi:10.1016/j.jmbbm.2013.12.019.
- [8] H. Kashani, A. Amadeh, A. Ohadizadeh, Effect of temperature on the strain induced  $\gamma \rightarrow \epsilon$  phase transformation in Stellite 21 during wear test, *Mater. Sci. Eng. A.* 435–436 (2006) 474–477. doi:10.1016/j.msea.2006.07.022.
- [9] Y. Chen, Y. Li, S. Kurosu, K. Yamanaka, N. Tang, A. Chiba, Effects of microstructures on the sliding behavior of hot-pressed CoCrMo alloys, *Wear*. 319 (2014) 200–210. doi:10.1016/j.wear.2014.07.022.

- [10] A. Chiba, K. Kumagai, N. Nomura, S. Miyakawa, Pin-on-disk wear behavior in a like-on-like configuration in a biological environment of high carbon cast and low carbon forged Co-29Cr-6Mo alloys, *Acta Mater.* 55 (2007) 1309–1318. doi:10.1016/j.actamat.2006.10.005.
- [11] M. Béreš, H.F.G. Abreu, L.P.M. Santos, C.M. Davies, D. Dye, Effect of variant transformations in fusion zones of gas metal arc welds, *Sci. Technol. Weld. Join.* 20 (2015) 353–360. doi:10.1179/1362171815Y.0000000025.
- [12] Y. Koizumi, S. Suzuki, K. Yamanaka, B. Lee, K. Sato, Y. Li, S. Kurosu, H. Matsumoto, A. Chiba, Strain-induced martensitic transformation near twin boundaries in a biomedical Co–Cr–Mo alloy with negative stacking fault energy, *Acta Mater.* 61 (2013) 1648–1661. doi:10.1016/j.actamat.2012.11.041.
- [13] K. Yamanaka, M. Mori, S. Kurosu, H. Matsumoto, A. Chiba, Ultrafine grain refinement of biomedical Co-29Cr-6Mo alloy during conventional hot-compression deformation, *Metall. Mater. Trans. A Phys. Metall. Mater. Sci.* 40 (2009) 1980–1994. doi:10.1007/s11661-009-9879-0.
- [14] Z. Wang, S.Y. Tang, S. Scudino, Y.P. Ivanov, R.T. Qu, D. Wang, C. Yang, W.W. Zhang, A.L. Greer, J. Eckert, K.G. Prashanth, Additive manufacturing of a martensitic Co–Cr–Mo alloy: Towards circumventing the strength–ductility trade-off, *Addit. Manuf.* 37 (2021) 101725. doi:10.1016/j.addma.2020.101725.
- [15] Y. Lu, C. Yang, Y. Liu, K. Yang, J. Lin, Characterization of lattice defects and tensile deformation of biomedical Co<sub>29</sub>Cr<sub>9</sub>W<sub>3</sub>Cu alloy produced by selective laser melting, *Addit. Manuf.* 30 (2019) 100908. doi:10.1016/j.addma.2019.100908.
- [16] F.S.H.B. Freeman, J. Sharp, J. Xi, I. Todd, Influence of solidification cell structure on the martensitic transformation in additively manufactured steels, *Addit. Manuf.* 30 (2019) 100917. doi:10.1016/j.addma.2019.100917.
- [17] J.R. Patel, M. Cohen, Criterion for the action of applied stress in the martensitic transformation, *Acta Metall.* 1 (1953) 531–538. doi:10.1016/0001-6160(53)90083-2.
- [18] J.. Bokros, E.. Parker, The mechanism of the martensite burst transformation in Fe-Ni single crystals, *Acta Metall.* 11 (1963) 1291–1301. doi:10.1016/0001-6160(63)90024-5.
- [19] L.H.M. Antunes, J.J. Hoyos, E.B. Fonseca, M. Béreš, P.F. da Silva Farina, E.S.N. Lopes, A.L. Jardini, R.M. Filho, Effect of phase transformation on ductility of additively manufactured Co–28Cr–6Mo alloy: An in situ synchrotron X-ray diffraction study during mechanical testing, *Mater. Sci. Eng. A.* 764 (2019) 138262.

- doi:10.1016/j.msea.2019.138262.
- [20] H.K.D.H. Bhadeshia, H. Abreu, S. Kundu, Calculation of crystallographic texture due to displacive transformations, *Int. J. Mater. Res.* 99 (2008) 342–346.  
doi:10.3139/146.101645.
- [21] S. Kundu, H.K.D.H. Bhadeshia, Crystallographic texture and intervening transformations, *Scr. Mater.* 57 (2007) 869–872.  
doi:https://doi.org/10.1016/j.scriptamat.2007.06.056.
- [22] R.T. Smith, T. Lolla, D. Gandy, L. Wu, G. Faria, A.J. Ramirez, S.S. Babu, P.M. Anderson, In situ X-ray diffraction analysis of strain-induced transformations in Fe- and Co-base hardfacing alloys, *Scr. Mater.* 98 (2015) 60–63.  
doi:10.1016/j.scriptamat.2014.11.003.
- [23] B. Lee, Y. Koizumi, H. Matsumoto, A. Chiba, Collective behavior of strain-induced martensitic transformation (SIMT) in biomedical Co–Cr–Mo–N alloy polycrystal: An ex-situ electron backscattering diffraction study, *Mater. Sci. Eng. A.* 611 (2014) 263–273. doi:10.1016/j.msea.2014.05.071.
- [24] I. Weißensteiner, M. Petersmann, P. Erdely, A. Stark, T. Antretter, H. Clemens, V. Maier-Kiener, Deformation-induced phase transformation in a Co-Cr-W-Mo alloy studied by high-energy X-ray diffraction during in-situ compression tests, *Acta Mater.* 164 (2019) 272–282. doi:https://doi.org/10.1016/j.actamat.2018.10.035.
- [25] K. Yamanaka, M. Mori, A. Chiba, Nanoarchitected Co–Cr–Mo orthopedic implant alloys: Nitrogen-enhanced nanostructural evolution and its effect on phase stability, *Acta Biomater.* 9 (2013) 6259–6267. doi:10.1016/j.actbio.2012.12.013.
- [26] K. Yamanaka, M. Mori, A. Chiba, Effects of nitrogen addition on microstructure and mechanical behavior of biomedical Co-Cr-Mo alloys, *J. Mech. Behav. Biomed. Mater.* 29 (2014) 417–426. doi:10.1016/j.jmbbm.2013.10.006.
- [27] B.D.D. Cullity, *Elements of x-ray diffraction*, Second, Addison-Wesley Publishing Company Inc, New York, 1978. doi:978-0201089202.
- [28] Z. Nishiyama, X-ray investigation of the mechanism of the transformation from face centered cubic lattice to body centered cubic, *Sci. Rep. Tohoku Univ.* 23 (1934) 637. <https://ci.nii.ac.jp/naid/10012549836/en/>.
- [29] M. Humbert, B. Petit, B. Bolle, N. Gey, Analysis of the  $\gamma$ - $\epsilon$ - $\alpha'$  variant selection induced by 10% plastic deformation in 304 stainless steel at  $-60^{\circ}\text{C}$ , *Mater. Sci. Eng. A.* 454–455 (2007) 508–517. doi:https://doi.org/10.1016/j.msea.2006.11.112.
- [30] D. Maréchal, Linkage between mechanical properties and phase transformations in a

- 301LN austenitic stainless steel, University of British Columbia, 2011.  
doi:<https://dx.doi.org/10.14288/1.0071814>.
- [31] P. Hegele, J. Von Kobylinski, L. Hitzler, C. Kremaszky, E. Werner, In-situ XRD study of phase transformation kinetics in a co-cr-w-alloy manufactured by laser powder-bed fusion, *Crystals*. 11 (2021) 1–21. doi:10.3390/cryst11020176.
- [32] B. Kemerling, J.C. Lippold, C.M. Fancher, J. Bunn, Residual stress evaluation of components produced via direct metal laser sintering, *Weld. World*. 62 (2018) 663–674. doi:10.1007/s40194-018-0572-z.
- [33] C.C. Tasan, M. Diehl, D. Yan, C. Zambaldi, P. Shanthraj, F. Roters, D. Raabe, Integrated experimental-simulation analysis of stress and strain partitioning in multiphase alloys, *Acta Mater*. 81 (2014) 386–400. doi:10.1016/j.actamat.2014.07.071.
- [34] X. Zhang, T. Sawaguchi, K. Ogawa, F. Yin, X. Zhao, Orientation dependence of variant selection and intersection reactions of  $\epsilon$  martensite in a high-manganese austenitic steel, *Philos. Mag. Lett.* 91 (2011) 563–571.  
doi:10.1080/09500839.2011.596492.
- [35] M.L. Benson, P.K. Liaw, H. Choo, D.W. Brown, M.R. Daymond, D.L. Klarstrom, Strain-induced phase transformation in a cobalt-based superalloy during different loading modes, *Mater. Sci. Eng. A*. 528 (2011) 6051–6058.  
doi:10.1016/j.msea.2011.03.096.
- [36] N. Nakada, T. Tsuchiyama, S. Takaki, S. Hashizume, Variant Selection of Reversed Austenite in Lath Martensite, *ISIJ Int.* 47 (2007) 1527–1532.  
doi:10.2355/isijinternational.47.1527.
- [37] J.H. Yang, C.M. Wayman, On secondary variants formed at intersections of  $\epsilon$  martensite variants, *Acta Metall. Mater.* 40 (1992) 2011–2023. doi:10.1016/0956-7151(92)90187-J.
- [38] H.C. Choi, T.K. Ha, H.C. Shin, Y.W. Chang, The formation kinetics of deformation twin and deformation induced  $\epsilon$ -martensite in an austenitic Fe-C-Mn steel, *Scr. Mater.* 40 (1999) 1171–1177. doi:[https://doi.org/10.1016/S1359-6462\(99\)00017-2](https://doi.org/10.1016/S1359-6462(99)00017-2).
- [39] E. Cakmak, S.C. Vogel, H. Choo, Effect of martensitic phase transformation on the hardening behavior and texture evolution in a 304L stainless steel under compression at liquid nitrogen temperature, *Mater. Sci. Eng. A*. 589 (2014) 235–241.  
doi:10.1016/j.msea.2013.09.093.
- [40] H. Won, K. Jung, S. Hwang, S. Kang, D. Kim, H.W. Lee, K. Jung, S. Hwang, S. Kang, D. Kim, Microstructure and mechanical anisotropy of CoCrW alloy processed by

- selective laser melting, *Mater. Sci. Eng. A.* 749 (2019) 65–73.  
doi:10.1016/j.msea.2019.02.013.
- [41] M. Mori, K. Yamanaka, S. Sato, S. Tsubaki, K. Satoh, M. Kumagai, M. Imafuku, T. Shobu, A. Chiba, Tuning strain-induced  $\gamma$ -to- $\varepsilon$  martensitic transformation of biomedical Co–Cr–Mo alloys by introducing parent phase lattice defects, *J. Mech. Behav. Biomed. Mater.* 90 (2019) 523–529. doi:10.1016/j.jmbbm.2018.10.038.
- [42] T. Ungár, Strain broadening caused by dislocations, *Mater. Sci. Forum.* 278–281 (1998) 151–156. doi:10.4028/www.scientific.net/msf.278-281.151.
- [43] L. Balogh, G. Ribárik, T. Ungár, Stacking faults and twin boundaries in fcc crystals determined by x-ray diffraction profile analysis, *J. Appl. Phys.* 100 (2006) 1–10. doi:10.1063/1.2216195.
- [44] S. Kundu, K. Hase, H.K.D.H. Bhadeshia, Crystallographic texture of stress-affected bainite, *Proc. R. Soc. A Math. Phys. Eng. Sci.* 463 (2007) 2309–2328. doi:10.1098/rspa.2007.1881.

## Appendix A

Table A.1 – Crystallographic variants for  $\epsilon$ -martensite with orientation, interaction energy, and Schmid factor for Shockley partial dislocations from boxed region in Figures 2 a) and d) for surface and bulk specimen, respectively. The bolded numbers indicate the selected variants, which were those with highest Schmid factors for partial dislocations.

Variant	Slip System	Surface					Bulk				
		$[297.8 \ 46.0 \ 28.9]_{\gamma}$					$[40.8 \ 31.4 \ 34.6]_{\gamma}$				
		Euler Angles ( $^{\circ}$ )			Interaction Energy ( $\text{MJ/m}^3$ )	Schmid Factor	Euler Angles ( $^{\circ}$ )			Interaction Energy ( $\text{MJ/m}^3$ )	Schmid Factor
		$\phi_1$	$\Phi$	$\phi_2$			$\phi_1$	$\Phi$	$\phi_2$		
$V_{\epsilon 1}$	$(111)$ $[\bar{2}11]$	57.59	15.12	79.87	-30.33	-0.16	199.83	24.33	43.20	12.89	0.07
	$(111)$ $[\bar{1}21]$	57.59	15.12	199.87	-9.73	-0.05	199.83	24.33	163.20	-26.90	-0.14
	$(111)$ $[\bar{1}1\bar{2}]$	57.59	15.12	319.87	40.05	0.21	199.83	24.33	283.20	14.02	0.07
$V_{\epsilon 2}$	$(\bar{1}11)$ $[\bar{2}11]$	226.01	55.67	93.19	-51.26	-0.26	323.09	55.28	111.43	-2.52	-0.01
	$(\bar{1}11)$ $[\bar{1}21]$	226.01	55.67	333.19	<b>92.76</b>	<b>0.48</b>	323.09	55.28	351.43	-71.00	-0.37
	$(\bar{1}11)$ $[\bar{1}1\bar{2}]$	226.01	55.67	213.19	-41.50	-0.21	323.09	55.28	231.43	<b>73.52</b>	<b>0.38</b>
$V_{\epsilon 3}$	$(\bar{1}\bar{1}1)$ $[\bar{2}\bar{1}1]$	351.67	76.22	195.37	26.34	0.14	102.82	65.42	184.30	43.40	0.22
	$(\bar{1}\bar{1}1)$ $[\bar{1}21]$	351.67	76.22	75.37	-7.75	-0.04	102.82	65.42	64.30	-79.61	-0.41
	$(\bar{1}\bar{1}1)$ $[\bar{1}1\bar{2}]$	351.67	76.22	315.37	-18.59	-0.10	102.82	65.42	304.30	36.21	0.19
$V_{\epsilon 4}$	$(11\bar{1})$ $[\bar{2}1\bar{1}]$	104.53	80.60	341.67	-35.00	-0.18	212.30	94.27	335.41	<b>77.93</b>	<b>0.40</b>
	$(11\bar{1})$ $[\bar{1}2\bar{1}]$	104.53	80.60	221.67	54.32	0.28	212.30	94.27	215.41	-73.77	-0.38
	$(11\bar{1})$ $[\bar{1}1\bar{2}]$	104.53	80.60	101.67	-19.32	-0.10	212.30	94.27	95.41	-4.16	-0.02

### 4.3 Bloco 2 – Kinetics of FCC to HCP transformation during aging heat treatment of Co-28Cr-6Mo alloy fabricated by laser-powder bed fusion (<https://doi.org/10.1007/s11661-023-07016-w>)

L.H.M. Antunes<sup>a\*</sup>, M. Bérés<sup>b</sup>, J.J. Hoyos<sup>c</sup>, L. Novotný<sup>d</sup>, H.F.G. de Abreu<sup>b</sup>, P.F. da Silva Farina<sup>a</sup>

<sup>a</sup> School of Mechanical Engineering, University of Campinas, Rua Mendeleev, 200, 13083-860, Campinas, SP, Brazil

<sup>b</sup> Department of Metallurgical and Materials Engineering, Federal University of Ceará, Av. Humberto Monte, 60445-554, Fortaleza, CE, Brazil

<sup>c</sup> Universidad de Buenos Aires, Facultad de Ingeniería, Departamento de Ingeniería Mecánica, Av. Paseo Colón 850, C1063, Buenos Aires, Argentina

<sup>d</sup> Faculty of Computer Science, Free University of Bozen-Bolzano, Dominikanerplatz / Piazza Domenicani 3, 39100 Bozen-Bolzano (BZ), Italy

\*Corresponding author: [lhmantunes@gmail.com](mailto:lhmantunes@gmail.com)

#### Abstract

Co-based alloys have been used as biomedical materials in the cast or wrought form for more than fifty years. Since then, studies have been performed to better understand the high mechanical strength and wear resistance of these alloys. Recently, additive manufacturing techniques, such as laser-powder bed fusion (L-PBF), are being employed to produce metallic implants directly from metal precursor powder. To achieve a balance between strength and ductility of L-PBF Co-based alloys, a manipulation of phase constituents through heat treatments is essential. In the present work, an in situ analysis of the  $\gamma$ -FCC  $\rightarrow$   $\varepsilon$ -HCP phase transformation occurring during aging heat treatment of the Co-28Cr-6Mo alloy produced by L-PBF was performed. For this, time-resolved synchrotron X-ray diffraction was employed. Our results revealed that a solution heat treatment before aging changes the kinetics of the  $\gamma$ -FCC  $\rightarrow$   $\varepsilon$ -HCP phase transformation as well as the  $\varepsilon$ -HCP phase morphology.

## 1. Introduction

Recently, additive manufacturing techniques, such as electron beam powder bed fusion and laser-powder bed fusion (L-PBF), are increasingly being employed to fabricate customized and near-net-shape components for biomedical applications directly from metal powders [1-3]. In this context, Co-28Cr-6Mo alloys stand out by presenting a good biocompatibility, high mechanical strength and wear resistance [4]. These properties make Co-28Cr-6Mo alloys suitable for fabrication of medical implants, especially for knee and hip joints [4,5].

In this alloy system, the thermodynamically stable phase at room temperature is a hexagonal close-packed ( $\epsilon$ -HCP) structure. At approximately 970 °C [6], such alloys undergo an allotropic transformation resulting in a face-centered cubic structure ( $\gamma$ -FCC). The  $\gamma$ -FCC phase can be easily stabilized at room temperature through fast cooling. The  $\epsilon$ -HCP phase can be obtained from the  $\gamma$ -FCC metastable condition through plastic deformation [7-9] or by means of isothermal heat treatment at around 800 °C [6]. Dahn et al. [10] showed that a Co-based alloy isothermally treated between 550 and 1050 °C presents a martensitic transformation with diffusion kinetics. Therefore, the nucleation of  $\epsilon$ -HCP phase is governed by the thermally activated movement of partial dislocations.

To achieve a balance between strength and ductility of L-PBF Co-based alloys, a manipulation of phase constituents through heat treatments is essential [11]. Recent works analyzed the effect of aging heat treatments on the kinetics of transformation in L-PBF samples. Ramirez-Ledesma et al. [12] performed an aging heat treatment at 750 °C for 1 hour in a rapid solidified Co20Cr alloy. The initial microstructure, constituted mainly by athermal  $\epsilon$ -HCP phase, evolved to an even larger amount of  $\epsilon$ -HCP phase with a gain of elongation and mechanical strength after the aging heat treatment.

Zhang et al. [13] performed a solution heat treatment at 1200 °C for 1 hour then cooled the samples to aging temperature (750 and 900 °C) and treated them for different periods of time. The authors identified that the FCC  $\rightarrow$  HCP transformation is harder to occur at low temperatures. Aging at 900 °C for 10 hours resulted in an almost completely  $\epsilon$ -HCP structure, while aging at 750 °C for 10 hours presented 80% of the transformed  $\epsilon$ -HCP phase. The high volume fraction of  $\epsilon$ -HCP detected by the authors may be attributed to the long period of aging heat treatment. Donkor et al. [14] performed a similar analysis in a high carbon and high nitrogen Co-based alloy. As-built samples were aged at 800°C during different periods of time. The

authors observed that after 10 hours of aging, the samples presented 100% of the transformed  $\epsilon$ -HCP phase.

Gloaguen et al. <sup>[15]</sup> investigated the residual stress distribution in a LPBF sample using neutron diffraction. Their studies revealed that the bottom and top surfaces of the probed parts developed tensile and/or low compression residual stresses while compressive stresses were determined in the internal volume. Residual stresses are of concern because they can cause part delamination, geometrical distortion and can reduce the fatigue life. In addition, residual stresses can be the origin of microstructural changes in materials. For example, in low stacking fault energy alloys, residual stresses exceeding yield stress of the material can promote plasticity-induced martensitic phase transformation.

Residual stress distribution heterogeneity in a volume part was also investigated numerically using the finite element method in our previous work <sup>[16]</sup>. In addition, a comparison of both kinetics of transformation and lattice microstrain evolution on the surface and in the bulk in the same alloys system was performed in <sup>[17]</sup>. In this work, a combination of both the synchrotron X-ray diffraction and EBSD technique was utilized.

Recent study shows that the combination of stress-relieving treatments and subsequent aging heat treatments is an effective method for reducing residual stress, homogenizing microstructure, achieving phase stability, and improving mechanical properties <sup>[18]</sup>. However, the *in situ* kinetics of transformation during aging heat treatment in L-PBF Co-28Cr-6Mo alloys have not yet been studied comprehensively <sup>[7,11,19]</sup>.

In the present work, we studied *in situ*  $\gamma$ -FCC  $\rightarrow$   $\epsilon$ -HCP phase transformation occurring during aging heat treatment of both the as-built and the solution treated Co-28Cr-6Mo sample produced by the L-PBF technique. To obtain time-resolved diffraction patterns during aging heat treatment, a synchrotron light source in conjunction with a Gleeble thermomechanical simulator was used. Microstructures were characterized using electron backscatter diffraction (EBSD) and transmission electron microscopy (TEM). The onset and kinetics of the phase transformation were identified for each initial condition, i.e., as-built and solution treated. In addition, the morphology and nucleation sites for the  $\epsilon$ -HCP phase were revealed.

## 2. Experimental procedure

### 2.1. Material

Specimens were manufactured using an EOSINT M 280 machine (EOS GmbH, Germany) utilizing MP1 Co–Cr–Mo metallic powder feedstock, which was also supplied by EOS GmbH [20]. The grain size analysis was performed using a particle size laser diffraction analyzer Mastersizer 2000E (Malvern Panalytical, Malvern, UK) resulting in particle size distribution of D50 of 25  $\mu\text{m}$ , D90 of 45  $\mu\text{m}$ . Material meets the chemical and mechanical specifications defined in ASTM F75. The powder was laser-melted layer by layer in a nitrogen atmosphere using a Yb-fiber laser with nominal power of 200 W, laser beam diameter of 100  $\mu\text{m}$ , scan speed up to 7 m/s, layer thickness of 20  $\mu\text{m}$  and rotation of 67° between individual layers. The chemical composition (wt.-%) of the produced specimens was determined by X-ray fluorescence and the carbon and nitrogen contents were obtained by combustion infrared detection and inert gas fusion, respectively: 27.89Cr-6.27Mo-0.72Mn-0.62Si-0.32Fe-0.1Ni-0.14C-0.13N, with balance Co.

### 2.2. Heat treatments

Two specimens were used for *in situ* synchrotron X-ray diffraction. One specimen was solution heat treated (ST) at 1150 °C for 1 hour followed by water quenching while the other specimen was kept in its as-built condition. Both specimens were submitted to an aging heat treatment, which was performed in a Gleeble 3500 thermomechanical simulator. This equipment is integrated in the XRD1/XTMS synchrotron beam line located at the Brazilian Synchrotron Light Laboratory (LNLS) at the National Center for Research in Energy and Materials (Campinas/Brazil). The Gleeble thermomechanical simulator was set to 800 °C with a heating rate of 80 °C/s. The temperature was kept for 4 hours and then cooled to room temperature at a rate of 15 °C/s.

### 2.3. Synchrotron X-ray diffraction

The aging heat treatments were performed under simultaneous acquisition of X-ray diffraction patterns at the XRD1/XTMS synchrotron beam line <sup>[21]</sup>. This facility uses two 1D Mythen detectors that cover 20° (2θ) with a gap of 0.9° between them. X-ray patterns were recorded from 24° to 68° (2θ), in four steps with a time of acquisition of 60 s at each step and an X-ray beam energy of 12 KeV ( $\lambda = 1.033 \times 10^{-10}$  m). A scan was acquired every 15 minutes during the 4 hours of heat treatment, when the samples were at 800 °C.

The  $\gamma$ -FCC and  $\epsilon$ -HCP phases were identified comparing the diffraction patterns with the ICSD cards 52934 and 53806, respectively. A pseudo-Voigt function was used for X-ray diffraction profile fitting. The background noise was treated using polynomial functions, which are modeled and refined during the profile fitting. The volume fraction  $x_i$  of each phase was estimated from the integrated intensities, which are directly proportional to the volume fraction of the phases (Equations 1 and 2) <sup>[11,22,23]</sup>

$$x_i = \frac{\frac{1}{N} \sum_{j=1}^N \left( \frac{I_{i,j}^{hkl}}{R_{i,j}^{hkl}} \right)}{\sum_i \left( \frac{1}{N} \sum_{j=1}^N \left( \frac{I_{i,j}^{hkl}}{R_{i,j}^{hkl}} \right) \right)}, \quad (1)$$

$$R^{hkl} = \frac{\rho^{hkl} |F^{hkl}|^2 \left( e^{-\left(1 + \frac{\sin(\omega)}{\sin(2\theta - \omega)} + 2M(\theta)\right)} \right)}{v_i^2 (4\sin^2\theta \cos\theta)}. \quad (2)$$

Where,  $I_{hkl}$  and  $R_{hkl}$  are the integrated and theoretical intensities of the hkl plane, respectively;  $\rho_{hkl}$  the plane multiplicity factor,  $F_{hkl}$  the plane structure factor,  $\omega$  the angle of the incident beam (approximately 15 °),  $\theta$  the Bragg angle and  $v$  the volume of the unit cell. The theoretical intensity of the diffraction pattern of a particular phase depends on several parameters including absorption, Lorentz and polarization factors. Since the distance between the sample and the detectors is constant, the absorption coefficient affects the absolute intensity of the peaks, but not their relative values. Therefore, the absorption coefficient does not enter the calculation of relative intensities.

$$M(\theta) = \frac{6h^2T}{mk} \left( \varphi(x) + \frac{x}{4} \right) \left( \frac{\sin(\theta)}{\lambda} \right)^2. \quad (3)$$

In Equation 3,  $M(\theta)$  is the Debye-Waller factor,  $h$  the Planck constant,  $T$  the absolute temperature (1073 K),  $m$  the mass of the vibrating atom,  $k$  the Boltzmann's constant,  $\Phi$  the Debye characteristic temperature of the alloy (430 K),  $x$  the ratio between the Debye and alloy temperatures,  $\lambda$  the wavelength in Ångström, and  $\varphi(x)$  the Debye function.

The lattice strain during the aging heat treatment, was estimated from the interplanar distance (Equation 4) [24] while the specimens were kept at 800 °C. The shift of the diffraction lines caused by strain reflects the average lattice strain within a particular hkl family of lattice planes. The experimental error, which was estimated from the standard deviation, was lower than  $5 \times 10^{-4}$ .

$$\varepsilon_{hk} = \frac{(d_{hkl} - d_{0,hk})}{d_{0,hk}} \quad (4)$$

where  $\varepsilon_{hkl}$  is the lattice strain,  $d_{hkl}$  and  $d_{0,hkl}$  the interplanar distances of the hkl plane in the stresses and stress-free crystal. The stress-free lattice spacing is estimated from the minimal lattice parameter ( $a_0$ ) and its corresponding Miller indices (Equation 5) [24].

$$d_{0,hkl} = \frac{a_0}{(h^2 + k^2 + l^2)^{1/2}} \quad (5)$$

#### 2.4. Microstructural analysis

To avoid the formation of deformation-induced  $\varepsilon$ -HCP phase during grinding when using a conventional metallographic preparation process, and to remove the oxide layer prevenient from heat treatments, specimens were electropolished. The electropolishing was performed on as-built, solution treated and aged samples using a solution of 10% perchloric acid in acetic acid while the electrolyte was maintained at 25°C. For this, a Struers Lectropol-5 equipment that operated at 20 V was employed. It is to be noted, that the same electropolishing procedure was applied for the preparation of sample's surfaces used in synchrotron X-Ray diffraction experiments. The electropolished specimens were subjected to microstructural characterization using a field emission gun FEI Quanta 450 and FEI Quanta 650 scanning electron microscopes both fitted with a Nordlys/Oxford Instruments EBSD detector. The indexing rate of EBSD scans varied from 96.6% to 99.1% and the mean angular deviation from 0.57 to 0.85, respectively. Zero solutions in the EBSD maps were extrapolated using five neighbors and wild spikes were extrapolated as well.

For nanoscale characterization, transmission electron microscopy (TEM) was used. Disc specimens, 3 mm in diameter, were cut from ~0.1 mm thick electrolytically thinned foils taken from both as-built and ST specimens. The disc specimens were then further electropolished to electron transparency by a Struers Tenupol-3 apparatus using the same solution and conditions of the electropolishing mentioned above. A JEOL JEM 2100F transmission electron microscope, operated at 200 keV was utilized to acquire bright field micrographs.

### 3. Results

The microstructure of both as-built and ST conditions of the Co-28Cr-6Mo alloy presents a single-phase  $\gamma$ -FCC structure, as can be seen in Figure 1. This is attributed to the high cooling rate associated with L-PBF and water quench for the as-built and ST, respectively, but also to the alloy relative high carbon <sup>[25]</sup> and nitrogen <sup>[26]</sup> content (0.14 wt.-% and 0.13 wt.-%, respectively). It is well known that carbon and nitrogen stabilize the  $\gamma$ -FCC phase and suppress the athermal martensitic transformation in this alloy system <sup>[27,28]</sup>, favoring the occurrence of a monophasic  $\gamma$ -FCC microstructure after fast cooling. The as-built condition presents elongated grains oriented parallel with the heat transfer direction (Figure 1a), while the ST specimen shows equiaxed grains and annealing twins (Figure 1b). The Kernel average misorientation (KAM) map of the as-built specimen (Figure 1c) revealed heterogeneously distributed regions with higher KAM angles, varying from zero to two degrees. The detected higher KAM values are located at sub-grain boundaries. This is an indication of a low degree of strain accommodation at sub-grains originated from fast solidification, generating a heterogeneous stress field near sub-grain boundaries. In contrast, the KAM angles of the ST specimen (Figure 1d) are lower, not greater than 1°, and more evenly distributed which can be attributed to strain accommodation caused by cooperative grain rotation during heat treatment. Lower KAM values and their homogenous distribution suggest a reduction of the internal stress in the matrix, resulting in a lower residual stress in samples subjected to the solution heat treatment.

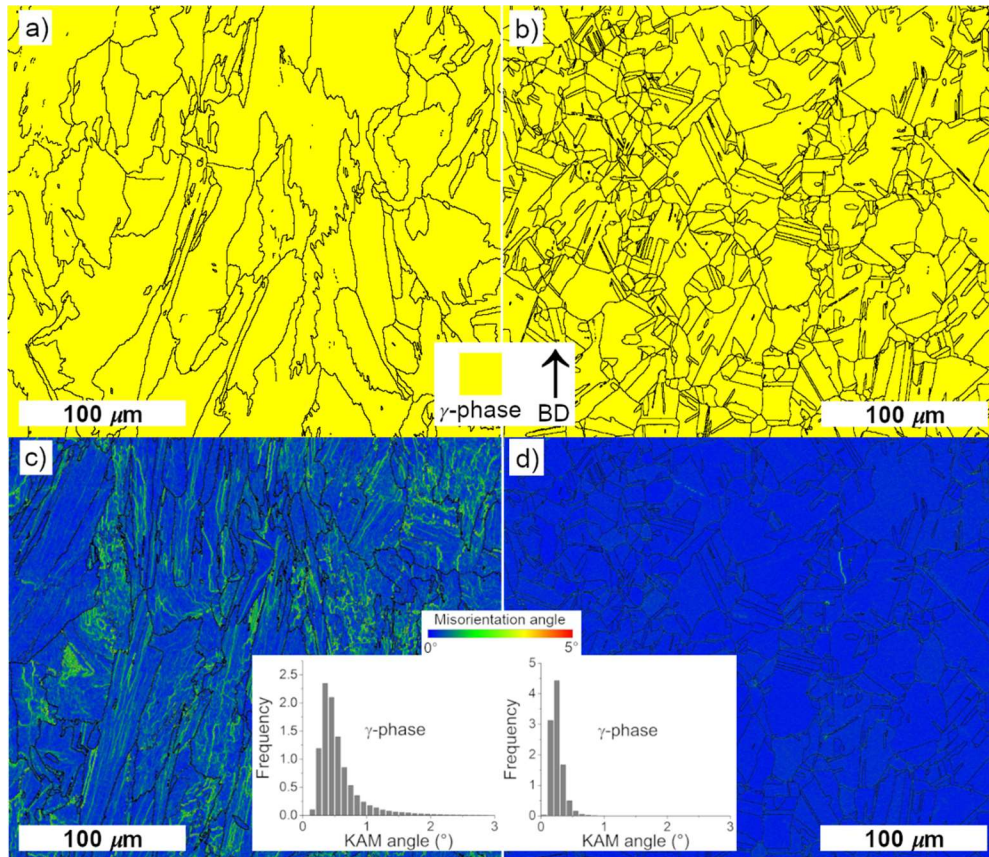


Fig. 1 – EBSD phase maps showing a single-phase  $\gamma$ -FCC structure of the (a) as-built and (b) solution heat treated specimens. The corresponding Kernel average misorientation maps are shown in (c) and (d). BD indicates the build direction and black lines depicts grain boundaries.

Figures 2a and 2b show bright field TEM micrographs of the as built and ST specimens, respectively. The stacking faults density found in ST sample is similar to that observed by Hug et al. [29]. The as-built sample presents a higher density of internal defects including dislocations and stacking-faults. These are generated during the non-equilibrium rapid solidification in the L-PBF process and act as effective nucleation sites of  $\epsilon$ -HCP martensite [30]. The morphology and nucleation sites of the  $\epsilon$ -HCP phase formed during aging in both as-built and ST specimen are illustrated in Figures 3 and 4, respectively. Table I summarizes the area fraction determined from the EBSD phase maps presented in Figures 1, 3 and 4. In the as-built aged specimen, (Figures 3a and 4a), the  $\epsilon$ -HCP phase occupies the interior of some grains and is also present in form of lamellae. Such observations are in accordance with Kurosu et al. [25], who have investigated the isothermal  $\gamma \rightarrow \epsilon$  transformation during aging and reported similar morphologies of the  $\epsilon$ -HCP phase formed in cast Co-Cr-Mo alloy. In contrast, in the ST specimen, the  $\epsilon$ -HCP phase was found to form preferentially at low-energy  $\Sigma 3$  coincidence site lattices (CSL) boundaries of the  $\gamma$ -FCC grains as depicted by the white ellipses in Figure 4d.

These results are in agreement with the work conducted by Béréš et al. [31]. Polygonal  $\gamma$ -FCC grains with annealing twins are maintained in the aged ST specimen. As can be seen in Figures 3b and 3d, the solution heat treatment recrystallizes the microstructure, resulting in equiaxed grains, the formation of annealing twins and reduced stacking faults density (Figure 2b). In our previous work, we have shown that the solution heat treatment is also effective in reducing microsegregation [11]. In addition, in Figure 3c, it is possible to identify deformed grains. Using the HKL Channel 5 Tango software, deformed grains were classified based on the internal average misorientation within each grain. If the average angle in grain is greater than the minimal angle to define a subgrain ( $>0.5^\circ$ ), the grain is classified as being deformed. The strain occurring from the  $\gamma \rightarrow \epsilon$  transformation is accommodated by few non-recrystallized  $\gamma$ -FCC grains surrounding the newly nucleated  $\epsilon$ -HCP phase.

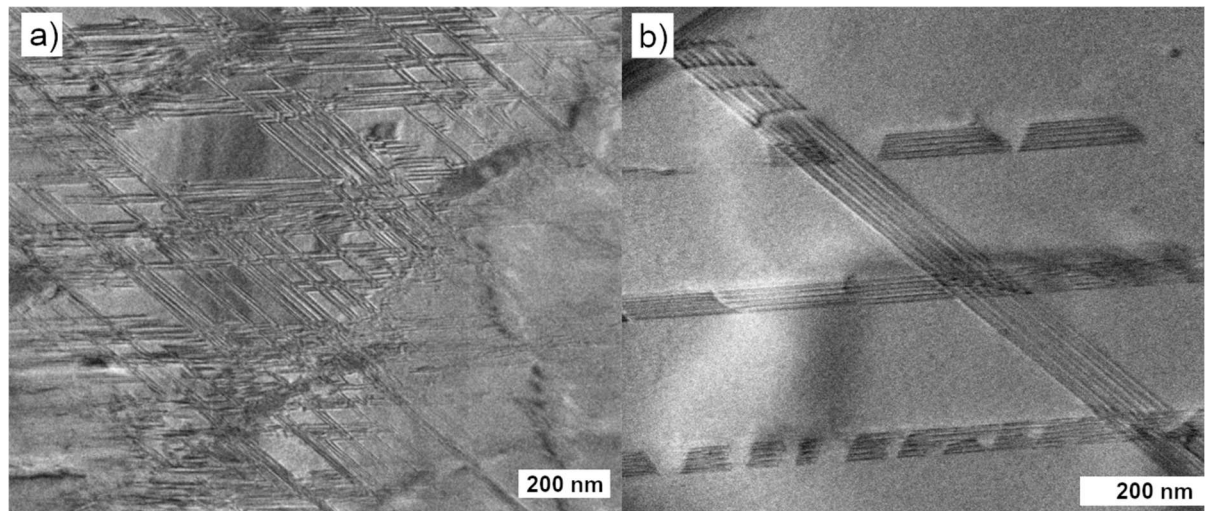


Fig. 2 – Bright-field TEM micrographs revealing stacking faults density in (a) as-built and (b) ST specimens, respectively.

Table I. Area fraction determined from the EBSD analysis.

Figure	$\gamma$ -FCC	$\epsilon$ -HCP
1a	100%	0
1b	100%	0
3a	42,0%	58,0%
3b	99,5%	0,5%
4a	58,7%	41,3%
4b	98,1%	1,9%

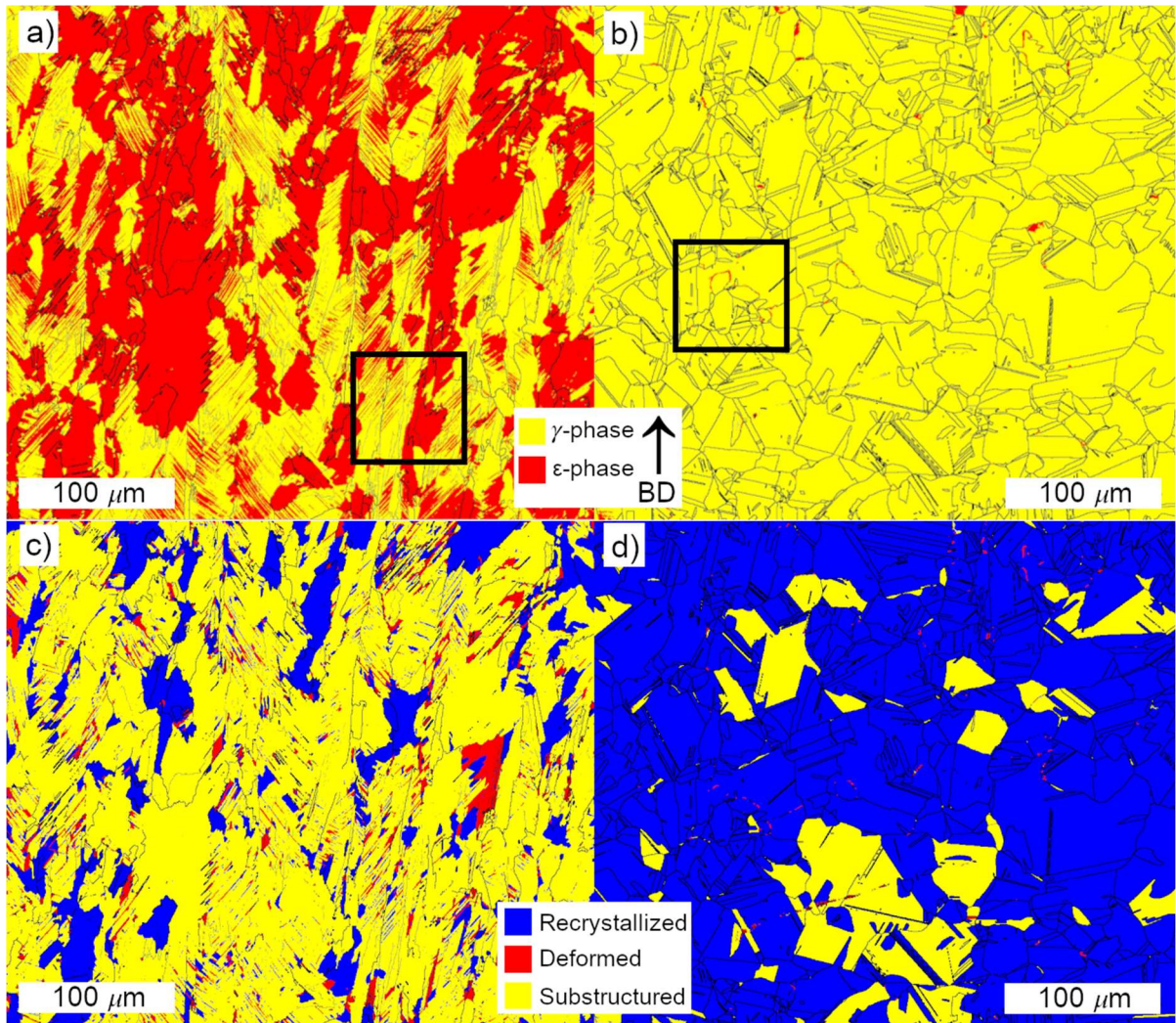


Fig. 3 – EBSD phase map of the (a) as-built and (b) ST specimens subjected to aging heat treatment at 800°C for 4 hours. Corresponding EBSD maps of recrystallized and deformed regions in (c) and (d), respectively. The black squares indicate the magnified region shown in Figure 4.

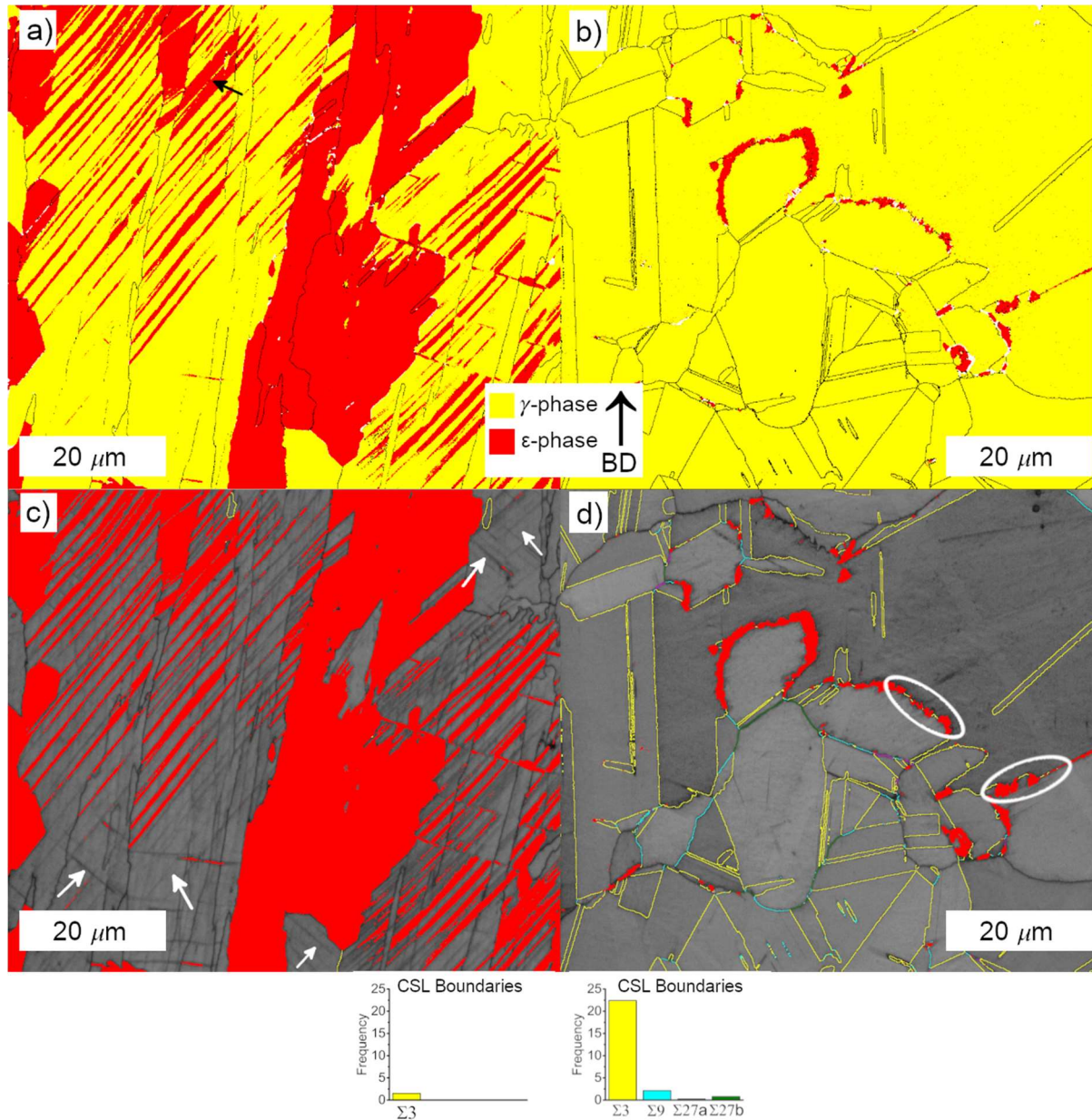


Fig. 4 – EBSD phase maps of the (a) as-built and (b) ST specimens submitted to aging heat treatment at 800 °C for 4 hours. The corresponding EBSD maps composition of band contrast, phase, and coincidence site lattice (CSL) distribution is shown in (c) and (d), respectively.

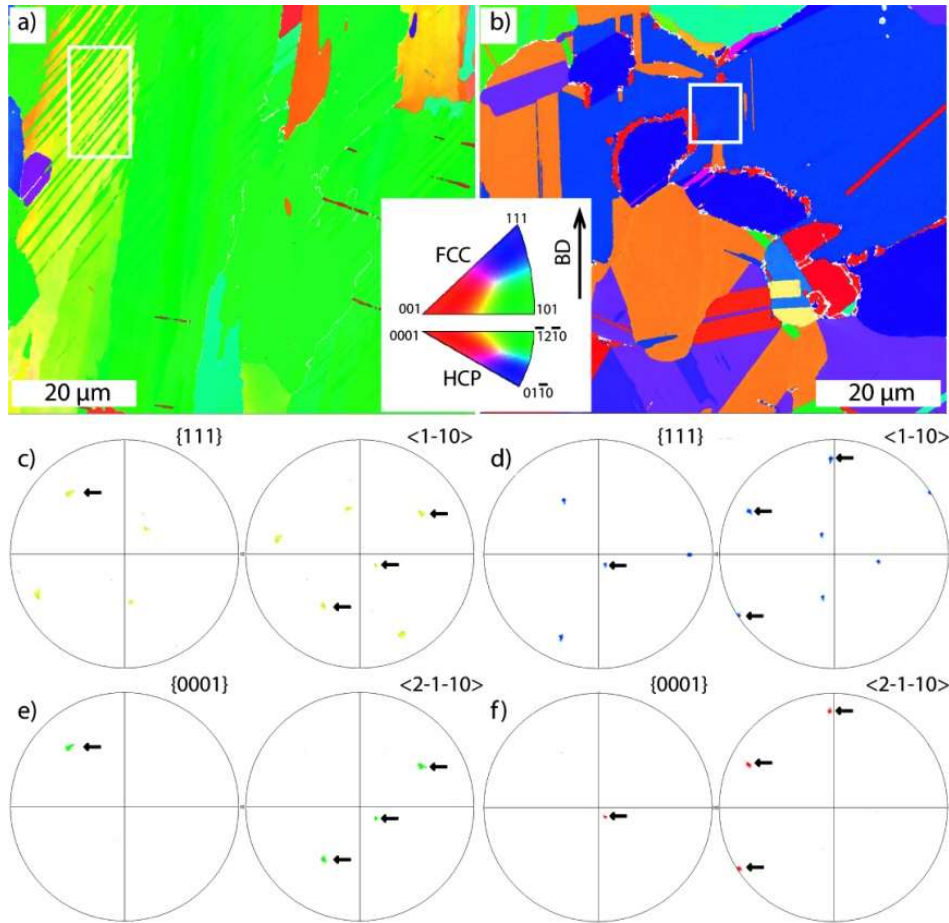


Fig. 5 Inverse pole figure maps of as-built (a) and ST specimens (b) heat treated at 800 °C for 4 hours. Boxed regions were used for the misorientation analysis between nucleated  $\epsilon$ -HCP phase and  $\gamma$ -FCC matrix considering Shoji-Nishiyama orientation relationship. The corresponding FCC and HCP pole figures are shown below the maps for  $\gamma$ -FCC (c), (d) and for  $\epsilon$ -HCP (e), (f) phases, respectively. Horizontal arrows indicate poles obeying the Shoji-Nishiyama orientation relationship. The vertical arrow indicates build direction (BD).

Figure 5 shows results of misorientation analysis between nucleated  $\epsilon$ -HCP phase and  $\gamma$ -FCC matrix. The analysis was conducted in the boxed region of inverse pole figures maps presented in Figures 5a and b. The corresponding pole figures of  $\gamma$ -FCC (c), (d) and that of  $\epsilon$ -HCP (e), (f) are shown below the maps. It is readily observed that some of the  $\epsilon$ -HCP poles in displayed pole figures coincide with  $\gamma$ -FCC poles obeying the Shoji-Nishiyama orientation relationship:  $\{111\}_{\gamma} // \{0001\}_{\epsilon}$  and  $\langle 110 \rangle_{\gamma} // \langle 2110 \rangle_{\epsilon}$ . Therefore, the  $\epsilon$ -HCP phase nucleation that took place during diffusional  $\gamma$ -FCC  $\rightarrow$   $\epsilon$ -HCP phase transition has the same lattice correlation with the  $\gamma$ -FCC matrix as reported previously for displacive  $\gamma$ -FCC  $\rightarrow$   $\epsilon$ -HCP martensitic phase transformation<sup>[17,32]</sup>. This can be attributed to the simultaneous satisfaction of the orientation relationship at the parent phase grain boundary by the product phase which can result in a memory effect<sup>[33]</sup>.

Additional reason can be associated with the suppression of movement of substitutional atoms during diffusional  $\gamma$ -FCC  $\rightarrow$   $\epsilon$ -HCP phase transition as pointed out by Béréš *et al.* [34]. The kinetics of the  $\epsilon$ -HCP phase during aging in as-built and ST conditions were followed via the time-resolved X-ray diffraction technique, using a synchrotron light source with results presented in Figures 6a and b. The *in situ* analysis shows that the  $\gamma \rightarrow \epsilon$  transformation starts after approximately 3000 s in the as-built specimen, while the onset of the phase transition in the ST specimen occurs at around 12000 s. Figure 7a presents the phase fraction evolution during aging heat treatment of the as-built and ST specimens, respectively. In Figure 7a, in the as-built specimen, it is noticeable that the largest amount of  $\epsilon$ -HCP phase nucleates in the first 10000 s of the aging heat treatment. In contrast, in the ST specimen, the onset of nucleation of the  $\epsilon$ -HCP phase is delayed and the gradual slope of the curve indicates a lower kinetics of nucleation, Figure 7a. After 4h of aging, the as-built specimen forms approximately 70% of  $\epsilon$ -HCP phase, while the ST specimen exhibits approximately 20% of  $\epsilon$ -HCP phase. Therefore, the average kinetics of the  $\epsilon$ -HCP phase nucleation during the  $\gamma \rightarrow \epsilon$  phase transformation is approximately 17 %/hour and 3 %/hour for the as-built and ST conditions, respectively. The Full Width at Half Maximum (FWHM) analysis presented in Figure 7b, revealed a broadening of the  $\{200\}_\gamma$  peak in the as-built condition. This can be attributed to the accumulation of dislocations in the  $\gamma$ -FCC matrix during the formation of the  $\epsilon$ -HCP phase. Figure 7c depicts the lattice strain evolution of planes  $\{111\}_\gamma$  and  $\{200\}_\gamma$  during the aging heat treatment. It is noticeable a continuous reduction of lattice strain in the ST specimen, while in the as-built specimen, the lattice strain tends to stop decreasing at approximately 5000s. Planes  $\{111\}_\gamma$  of the as-built specimen even present a lattice strain increase starting at approximately 7000s. The larger  $\epsilon$ -HCP phase fraction nucleated during aging heat treatment in the as-built specimen may be the cause of the increase in lattice strain. As presented previously, the surrounding  $\gamma$ -FCC grains accommodate the strain prevent from the nucleation of the  $\epsilon$ -HCP phase causing localized microstructural strains observed by KAM and lattice strain analysis. On the other hand, the ST specimen does not present sufficient  $\epsilon$ -HCP phase nucleation to promote enough straining in the  $\gamma$ -FCC matrix to be observable both by KAM and lattice strain analysis.

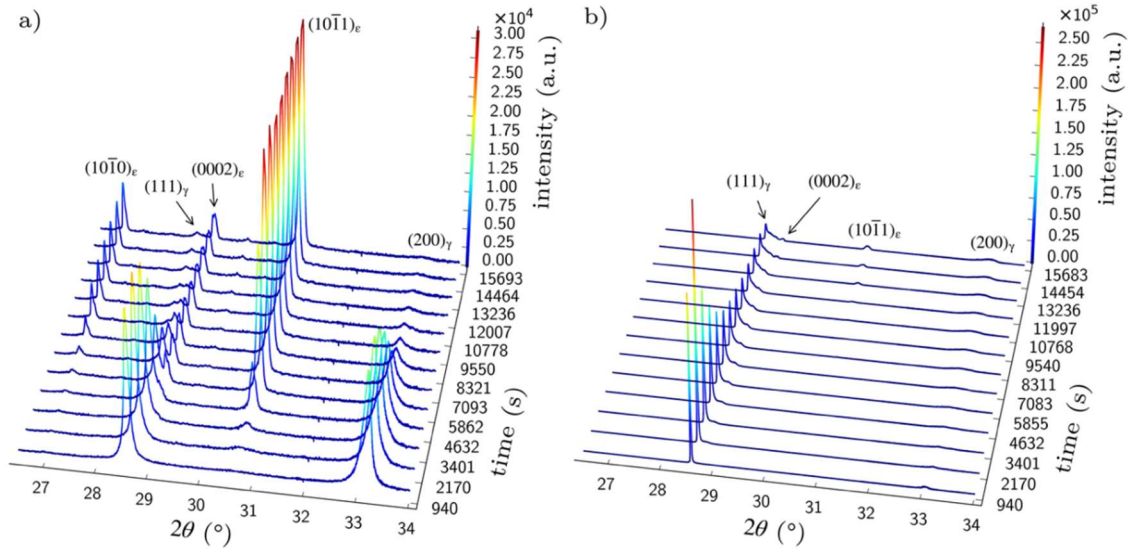


Fig. 6 – Time-resolved X-ray diffraction patterns during aging of the (a) as-built and (b) ST specimen, respectively.

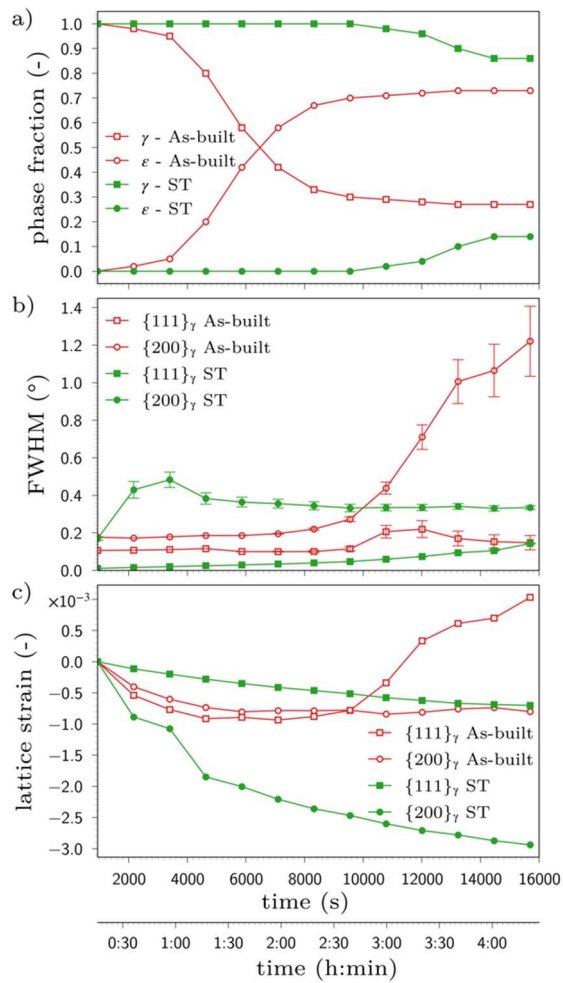


Fig. 7 – Phase fractions of (a)  $\gamma$ -FCC and  $\epsilon$ -HCP phases present in as-built and ST specimens during aging. The Full Width at Half Maximum (FWHM) analysis is shown in (b). And lattice strain of  $\{111\}_{\gamma}$  and  $\{200\}_{\gamma}$  in (c).

#### 4. Discussion

The higher stacking fault density present in the as-built specimen compared to the ST condition was revealed in Figures 2a and 2b. It is known, that the first step in the nucleation process of the  $\varepsilon$ -HCP phase is the creation of stacking faults in the  $\gamma$ -FCC matrix [28,35]. Since the as-built specimen has a higher density of stacking faults, Figure 2a, it has a higher potential to nucleate the  $\varepsilon$ -HCP phase. In the model proposed by Olson and Cohen [35], the intrinsic stacking fault can be formed by the motion of a Shockley partial dislocation on a compact plane, whereas the movement of such a dislocation on every second compact plane  $\{111\}$  of the FCC lattice produces an HCP structure. Thus, an intrinsic stacking fault can be considered as an embryo with an HCP structure of thickness of two compact planes.

In terms of the FCC unit cell, the distance between two consecutive planes of atoms measured parallel to the compact planes is equal to  $a/6\langle 11\bar{2} \rangle$  vector. Therefore, if a dislocation with Burgers vector of  $a/6\langle 11\bar{2} \rangle$  slides between two  $\{111\}$  planes in a FCC crystal, every plane above the sliding position will be displaced in relation to those below the sliding plane by a vector  $a/6\langle 11\bar{2} \rangle$  [36]. This type of dislocation with  $b = a/6\langle 11\bar{2} \rangle$  is known as Shockley partial dislocation. The slip of Shockley partial dislocations disrupts the atomic ordering of the crystalline lattice and causes a stacking fault over the area of the plane swept by the dislocation [37,38]. In thermodynamically stable FCC structures, the stacking fault is a region of high Gibbs free energy. If the FCC phase is metastable with respect to the HCP structure, the stacking fault energy will be negative and the slip of the Shockley partial dislocation will decrease the Gibbs free energy of the system [37].

Figures 3a and 4a revealed that, the  $\varepsilon$ -HCP phase has in initial stages of the  $\gamma$ -FCC  $\rightarrow$   $\varepsilon$ -HCP phase transformation a lamellar morphology. This is because stacking faults are planar defects and  $\varepsilon$ -HCP phase nucleate at intrinsic stacking faults. With progressing heat treatment, the lamellae continue to grow ahead of stacking fault until they reach a grain boundary. At the same time, the lamellae continue to increase in thickness until merging with parallel neighbor lamellae. Since the stacking of FCC and HCP crystal structures is very close, the  $\gamma$ -FCC  $\rightarrow$   $\varepsilon$ -HCP phase transformation requires atoms moving along the  $\{111\}$  plane and the slip of the Shockley partial dislocation will decrease the Gibbs free energy of the system. Therefore, the process of phase transition continues to progress and comes to a standstill once the thermodynamically stable HCP phase occupies the interior of the entire grain.

The sigmoidal shape of the curves for the transformation kinetics showed in Figure 7a, follows the model proposed by Dahn et al. <sup>[10]</sup>, where the rate limiting step is the thermally activated motion of Shockley partial dislocations. The lower density of stacking faults and dislocations in the ST specimen increases the incubation time and reduces the growth rate of the  $\epsilon$ -HCP phase in comparison to the as-built specimen. When the  $\epsilon$ -HCP phase starts to nucleate, then Shockley partial dislocations are consumed, and the kinetics of transformation reduces. Due to the kinetics reduction, the  $\gamma$ -FCC  $\rightarrow$   $\epsilon$ -HCP phase transformation becomes sluggish, as can be seen in Figure 7a after approximately 9000s and 14000s for the as-built and ST specimens, respectively.

Figure 7b shows the evolution of FWHM of selected  $\gamma$ -FCC planes as a function of aging time. As shown in this figure, a peak broadening of the plane  $\{200\}_\gamma$  took place and this was accompanied by a simultaneous decrease in the relative peak intensity. At the same time, an increase in the relative  $\{0002\}_\epsilon$  and  $\{10\bar{1}1\}_\epsilon$  peak intensities was observed, Figures 6a and b. This is confirmed by the phase fraction presented in Figure 7a. The as-built specimen not only exhibits a higher fraction of the  $\epsilon$ -HCP phase, but also the nucleation of the  $\epsilon$ -HCP phase starts earlier when compared to the ST specimen. This difference in time for the nucleation to take place may be attributed to the effect of the solution heat treatment. The diffusion along stacking faults is facilitated due to the presence of microstructural defects, in particular vacancies, in the region of the stacking fault <sup>[39,40]</sup>. Since the solution heat treatment reduces the stacking fault density and microstructural defects, there are fewer regions of facilitated diffusion, resulting in a longer time for nucleation of the  $\epsilon$ -HCP phase. In addition, García et al. <sup>[41]</sup> suggested that the internal stresses generated by twins during quenching after solution heat treatment can be relaxed by the reheating to aging temperature and significantly change the defect structure of the metastable  $\gamma$ -FCC phase. The modified defect structure during reheating may inhibit the growth of martensite embryos by imposing additional obstacles to the motion of partial dislocations. Therefore, when the ST specimen is submitted to aging heat treatment, a longer time is required for the  $\epsilon$ -HCP phase to nucleate.

The phase fraction of the  $\epsilon$ -HCP phase calculated from the time resolved X-ray diffraction analysis (Figure 7a) is higher than the area fraction obtained from the EBSD phase map (Table I). Roudnická et al. <sup>[42]</sup> have shown the formation of nanometric needles of  $\epsilon$ -HCP phase in early stages of aging heat treatment. Similar needle-like structures, depicted in Figure 4c by white arrows, were observed in the as-built aged sample and were not indexed as the  $\epsilon$ -HCP phase. The presence of the  $\epsilon$ -HCP phase in the form of lamellae in the as-built specimen

can be attributed to the orientation of the stacking faults. Moreover,  $\epsilon$ -HCP can easily merge during growth, even if they were nucleated at distinct regions of the original  $\gamma$ -FCC grain <sup>[14]</sup>. The merging process is favored due to the high density of stacking faults in the as-built specimen. Here, the diffusion along stacking faults is facilitated and the  $\epsilon$ -HCP lamellae can freely move until they meet other lamellae, merging into each other. The black arrow in Figure 4a depicts two merging lamellae of the  $\epsilon$ -HCP phase.

Deformation twinning plays a crucial role in plastic deformation of HCP metals. The present study did not evidenced formation of deformation twins in the HCP phase. This can be attributed to negative stacking fault energy of the studied alloy <sup>[43]</sup> and the absence of plastic deformation. Figure 3c revealed that most grains in the as-built sample are substructured indicating a high density of crystal defects and increased stored energy which also enhances the kinetics of  $\gamma$ -FCC  $\rightarrow$   $\epsilon$ -HCP phase transformation. In the as-built sample, most crystal defects are associated with the residual stress accumulated during the fast solidification of the alloy during the L-PBF process. In contrast, in the ST specimens a higher fraction of recrystallized grains was revealed, Figure 3d. The recrystallization process starts with a recovery process during which the stored energy is reduced by the reduction or rearrangement of defects in the crystal structure <sup>[44]</sup>. Kajima et al. <sup>[45]</sup> have shown that, in Co-based alloys that were solution heat treated at 1150°C, the recrystallization process is accompanied by the relief of residual stress and the formation of annealing twins. The presence of many  $\Sigma 3$  twin boundaries, as evidenced in Figure 4d, indicates that such stress relief indeed occurred. Since the solution heat treatment reduces the amount of crystal defects, there are less  $\epsilon$ -HCP nucleation sites available. Rajan <sup>[46]</sup> proposed that twin-twin intersections could provide a source of Shockley partials due to the localized stress concentration. Béréš et al. <sup>[31]</sup> showed that the CSL boundaries, in particular  $\Sigma 3$  twin boundaries, are nucleation sites for the  $\epsilon$ -HCP phase in the solution treated Co-28Cr-6Mo alloy. Therefore, the aging treatment of the solution heat treated sample led to different morphology of the  $\epsilon$ -HCP phase (Figures 4b and d) in comparison to the lamellar structure observed in the as-built specimen (Figures 4a and c).

## 5. Conclusions

The characteristics of the isothermal  $\gamma$ -FCC  $\rightarrow$   $\epsilon$ -HCP phase transformation in a Co-28Cr-6Mo alloy produced by laser-powder bed fusion were investigated via time-resolved X-ray diffraction during aging heat treatment at 800°C for 4 hours. The following conclusions are drawn:

- The as-built specimen presents higher kinetics of phase transformation when compared to the ST condition. When the  $\epsilon$ -HCP phase starts to nucleate, the Shockley partial dislocations are consumed, and the kinetics of transformation reduces.
- The lower density of dislocations in the ST specimen augments the incubation time and reduces the growth rate of the  $\epsilon$ -HCP phase in comparison to the as-built specimen.
- The  $\{200\}_{\gamma}$  peak broadening is associated with the decrease of the relative peak intensity, concurrent with an increase in the relative  $\{0002\}_{\epsilon}$  and  $\{10\bar{1}1\}_{\epsilon}$  peak intensities. The peak broadening is caused by the accumulation of dislocations in the  $\gamma$ -FCC matrix during the formation of the  $\epsilon$ -HCP phase.
- The  $\epsilon$ -HCP phase presents different morphology depending on the initial sample condition. The as-built aged sample presents  $\epsilon$ -HCP phase in the form of lamellae, while the ST aged sample presents granular  $\epsilon$ -HCP morphology. This difference is attributed to the nucleation sites of each condition, i.e. stacking faults in the as-built sample and CSL boundaries in the ST specimen.

## Acknowledgments

The authors would like to acknowledge the experimental support of F.E. Montoro, Dr. O.R. Ospina and Dr. V. Mogili at the Brazilian Nanotechnology National Laboratory. The authors are grateful for the support provided by L. Wu during the synchrotron experiments (project Nr. 20180228) at the Brazilian Synchrotron Light Laboratory, part of the Brazilian Centre for Research in Energy and Materials (CNPEM), a private non-profit organization under the supervision of the Brazilian Ministry for Science, Technology, and Innovations (MCTI). L. Novotný acknowledges financial support provided by Provincia Autonoma di Bolzano/Alto

Adige - Ripartizione Innovazione, Ricerca, Università e Musei - project HI-TECH MANUFACTURING (CUP codex I59C20000040003).

This research used facilities of the Brazilian Nanotechnology National Laboratory (LNNano), part of the CNPEM, projects Nr.: SEM-C1-27387 and TEMM-C1-27373. A portion of the microstructural characterization was performed at the Central Analítica UFC/CT-INFRA-FINEP/Pro-Equipamentos-CAPES/CNPq-SisNano-MCTI 2019 (Grant 442577/2019-2)-INCT-FUNCAP. Authors acknowledge financial support by CRC 2021 project “Integrating Physics-Based and Data-Driven Modelling for Efficient Process Parameters, Material Design and Optimisation in Additive Manufacturing for Industry 4.0”. This work was partially financed by the Coordenação de Aperfeiçoamento de Pessoal de Nível Superior, Brazil, Finance Code 001.

### Conflict of interests

On behalf of all authors, the corresponding author states that there is no conflict of interest.

### References

- 1 A.L. Jardini, M.A. Larosa, R. Maciel Filho, C.A. de C. Zavaglia, L.F. Bernardes, C.S. Lambert, D.R. Calderoni, and P. Kharmandayan: *J. Craniomaxillofac. Surg.*, 2014, vol. 42, pp. 1877–84.
- 2 X. Wang, S. Xu, S. Zhou, W. Xu, M. Leary, P. Choong, M. Qian, M. Brandt, and Y.M. Xie: *Biomaterials*, 2016, vol. 83, pp. 127–41.
- 3 A. Edelmann, L. Riedel, and R. Hellmann: *Materials (Basel)*, 2020, vol. 13, p. 5390.
- 4 B. Patel, G. Favaro, F. Inam, M.J. Reece, A. Angadji, W. Bonfield, J. Huang, and M. Edirisinghe: *Mater. Sci. Eng. C*, 2012, vol. 32, pp. 1222–9.
- 5 M.T. Andani, N. Shayesteh Moghaddam, C. Haberland, D. Dean, M.J. Miller, and M. Elahinia: *Acta Biomater.*, 2014, vol. 10, pp. 4058–70.
- 6 A.D.J. Saldívar García, A.M. Medrano, A.S. Rodríguez, and A. Salinas Rodríguez: *Metall. Mater. Trans. A*, 1999, vol. 30, pp. 1177–84.
- 7 S. Cai, M.R. Daymond, and Y. Ren: *Mater. Sci. Eng. A*, 2013, vol. 580, pp. 209–16.
- 8 N. Iskounen, P.A. Dubos, J. Fajoui, M. Coret, M.J. Moya, B. Girault, N. Barrier, N. Bruzy, E. Hug, and D. Gloaguen: *Metall. Mater. Trans. A Phys. Metall. Mater. Sci.*,

- 2021, vol. 52, pp. 1477–91.
- 9 P.-A. Dubos, J. Fajoui, N. Iskounen, M. Coret, S. Kabra, J. Kelleher, B. Girault, and D. Gloaguen: *Mater. Lett.*, 2020, vol. 281, p. 128812.
  - 10 N.C. Dahn, D. Morphy, and K. Rajan: *Acta Metall.*, 1984, vol. 32, pp. 1317–22.
  - 11 L.H.M. Antunes, J.J. Hoyos, E.B. Fonseca, M. Béreš, P.F. da Silva Farina, E.S.N. Lopes, A.L. Jardini, and R.M. Filho: *Mater. Sci. Eng. A*, 2019, vol. 764, p. 138262.
  - 12 A.L. Ramirez – Ledesma, J.C. Luna – Manuel, H.F. Lopez, and J.A. Juarez – Islas: *Mater. Sci. Eng. A*, 2022, vol. 844, p. 143161.
  - 13 M. Zhang, Y. Yang, C. Song, Y. Bai, and Z. Xiao: *J. Alloys Compd.*, 2018, vol. 750, pp. 878–86.
  - 14 B.T. Donkor, J. Song, Y. Fu, M. Kattoura, S.R. Mannava, M.A. Steiner, and V.K. Vasudevan: *Scr. Mater.*, 2020, vol. 179, pp. 65–9.
  - 15 D. Gloaguen, B. Girault, B. Courant, P.A. Dubos, M.J. Moya, F. Edy, and J. Rebelo Kornmeier: *Metall. Mater. Trans. A Phys. Metall. Mater. Sci.*, 2020, vol. 51, pp. 951–61.
  - 16 L. Novotny, M. Béreš, B. Carpentieri, and H.F.G. Abreu: *ECS Trans.*, 2022, vol. 107, p. 1761.
  - 17 L.H.M. Antunes, J.J. Hoyos, T.C. Andrade, P.W.C. Sarvezuk, L. Wu, J.A. Ávila, J.P. Oliveira, N. Schell, A.L. Jardini, J. Žilková, P.F. da Silva Farina, H.F.G. Abreu, and M. Béreš: *Addit. Manuf.*, 2021, vol. 46, p. 102100.
  - 18 Y. Zhou, Q. Sun, X. Dong, N. Li, Z.J. Shen, Y. Zhong, M. Eriksson, J. Yan, S. Xu, and C. Xin: *J. Alloys Compd.*, 2020, vol. 840, p. 155664.
  - 19 R.T. Smith, T. Lolla, D. Gandy, L. Wu, G. Faria, A.J. Ramirez, S.S. Babu, and P.M. Anderson: *Scr. Mater.*, 2015, vol. 98, pp. 60–3.
  - 20 EOS: *Material Data Sheet EOS CobaltChrome MPI*, 2011, vol. 49, pp. 1–6.
  - 21 G. Faria, L. Wu, T. Alonso, A. Isaac, J. Piton, R. Neuenschwander, and A.J. Ramirez: in *In-situ Studies with Photons, Neutrons and Electrons Scattering II*, T. Kannengiesser, S.S. Babu, Y. Komizo, and A.J. Ramirez, eds., Springer International Publishing, Cham, 2014, pp. 245–59.
  - 22 I. V. Ivanov, K.I. Emurlaev, D. V. Lazurenko, A. Stark, and I.A. Bataev: *Mater. Charact.*, 2020, vol. 166, p. 110403.
  - 23 M.R. Crivoi, J.J. Hoyos, M.T. Izumi, D.J.M. de Aguiar, R.S. Namur, A.L. Terasawa, and O.M. Cintho: *Cryogenics (Guildf.)*, 2020, vol. 105, p. 103020.
  - 24 S.V. Navas, J.J. Hoyos, E.A. Torres, M.T. Izumi, and O.M. Cintho: *Cryogenics*

- (*Guildf.*), 2021, vol. 120, p. 103384.
- 25 S. Kurosu, H. Matsumoto, and A. Chiba: *Metall. Mater. Trans. A Phys. Metall. Mater. Sci.*, 2010, vol. 41, pp. 2613–25.
- 26 K. Yamanaka, M. Mori, and A. Chiba: *Acta Biomater.*, 2013, vol. 9, pp. 6259–67.
- 27 S.H. Lee, E. Takahashi, N. Nomura, and A. Chiba: *Nippon Kinzoku Gakkaishi/Journal Japan Inst. Met.*, 2005, vol. 70, pp. 260–4.
- 28 C. Song, H. Park, H. Seong, and H.F. López: *Metall. Mater. Trans. A Phys. Metall. Mater. Sci.*, 2006, vol. 37, pp. 3197–204.
- 29 E. Hug, C. Keller, P.A. Dubos, and M.M. Celis: *J. Mater. Res. Technol.*, 2021, vol. 11, pp. 1362–77.
- 30 Z. Wang, S.Y. Tang, S. Scudino, Y.P. Ivanov, R.T. Qu, D. Wang, C. Yang, W.W. Zhang, A.L. Greer, J. Eckert, and K.G. Prashanth: *Addit. Manuf.*, 2021, vol. 37, p. 101725.
- 31 M. Béréš, C.C. Silva, P.W.C. Sarvezuk, L. Wu, L.H.M. Antunes, A.L. Jardini, A.L.M. Feitosa, J. Žilková, H.F.G. de Abreu, and R.M. Filho: *Mater. Sci. Eng. A*, 2018, vol. 714, pp. 36–42.
- 32 K. Yamanaka, M. Mori, and A. Chiba: *J. Mech. Behav. Biomed. Mater.*, 2014, vol. 29, pp. 417–26.
- 33 H.-R. Wenk, I. Lonardelli, and D. Williams: *Acta Mater.*, 2004, vol. 52, pp. 1899–907.
- 34 M. Béréš, H.F.G. Abreu, L.P.M. Santos, C.M. Davies, and D. Dye: *Sci. Technol. Weld. Join.*, 2015, vol. 20, pp. 353–60.
- 35 G.B. Olson and M. Cohen: *Metall. Trans. A*, 1976, vol. 7, pp. 1897–904.
- 36 W. Bollmann: in *Crystal Defects and Crystalline Interfaces*, Springer Berlin Heidelberg, Berlin, Heidelberg, 1970, pp. 78–97.
- 37 D.A. Porter and K.E. Easterling: *Phase Transformations in Metals and Alloys (Revised Reprint)*, CRC Press, 2009.
- 38 R. Bauer, E.A. Jägle, W. Baumann, and E.J. Mittemeijer: *Philos. Mag.*, 2011, vol. 91, pp. 437–57.
- 39 R.E. Smallman and P.S. Dobson: *Metall. Trans.*, 1970, vol. 1, pp. 2383–9.
- 40 D.H. Chung, H. Guk, D. Kim, S.S. Han, N. Park, K. Choi, and S.-H. Choi: *RSC Adv.*, 2014, vol. 4, p. 9223.
- 41 A.D.J. Saldívar García, A. Maní Medrano, A. Salinas Rodríguez, A. de J. Saldívar García, A. Maní Medrano, and A. Salinas Rodríguez: *Scr. Mater.*, 1999, vol. 40, pp. 717–22.

- 42 M. Roudnická, O. Molnárová, J. Drahokoupil, J. Kubásek, J. Bigas, V. Šreibr, D. Paloušek, and D. Vojtěch: *Addit. Manuf.*, 2021, vol. 44, p. 102025.
- 43 Y. Koizumi, S. Suzuki, K. Yamanaka, B. Lee, K. Sato, Y. Li, S. Kurosu, H. Matsumoto, and A. Chiba: *Acta Mater.*, 2013, vol. 61, pp. 1648–61.
- 44 R.D. Doherty, D.A. Hughes, F.J. Humphreys, J.J. Jonas, D. Juul Jensen, M.E. Kassner, W.E. King, T.R. McNelley, H.J. McQueen, and A.D. Rollett: *Mater. Today*, 1998, vol. 1, pp. 14–5.
- 45 Y. Kajima, A. Takaichi, N. Kittikundecha, T. Nakamoto, T. Kimura, N. Nomura, A. Kawasaki, T. Hanawa, H. Takahashi, and N. Wakabayashi: *Mater. Sci. Eng. A*, 2018, vol. 726, pp. 21–31.
- 46 K. Rajan: *Metall. Trans. A*, 1984, vol. 15, pp. 1335–8.

## 5 Síntese dos resultados e discussão geral

Na presente tese foi possível verificar detalhes dos processos de transformação de fases CFC – HC que ocorrem na liga Co-28Cr-6Mo, seja essa transformação induzida por deformação ou isotérmica. Estes conceitos se complementam no sentido de entender o comportamento em trabalho da referida liga. Pensando na aplicação médica, pela fabricação de implantes dentais ou ortopédicos, o efeito da fase HC no comportamento em desgaste, por exemplo, da liga Co-28Cr-6Mo é fundamental. Uma vez que a fase HC será induzida durante o processo de desgaste natural do implante, mas também já pode estar presente na microestrutura da peça se esta passar por um tratamento térmico de envelhecimento, por exemplo.

Nota-se que, tanto para o caso da fase induzida por deformação quanto para a fase obtida isotermicamente, os sítios preferenciais de nucleação são as falhas de empilhamento, caracterizadas como parciais de Shockley. A maior quantidade de falhas de empilhamento na amostra como produzida propiciou uma nucleação mais rápida da fase HC tanto no processo induzido por deformação quanto no processo isotérmico. No entanto, a menor plasticidade da amostra como produzida, atribuída à maior quantidade de interfaces CFC/HC, não permite que a transformação CFC – HC ocorra prolongadamente. Por outro lado, a amostra solubilizada apresenta elevada plasticidade e, mesmo possuindo menor quantidade inicial de sítios de nucleação da fase HC, ela apresenta maior fração volumétrica desta fase ao final da deformação. Isso ocorre, principalmente, por conta da microdeformação gerada na fase CFC pela própria transformação martensítica, que leva à formação de novas falhas de empilhamento e, conseqüentemente, novos sítios de nucleação. Esta maior plasticidade observada na amostra solubilizada pode ser atribuída à microestrutura obtida após o tratamento térmico e também ao processo semelhante ao observado em aços TRIP, nos quais ocorre uma supressão da estricção pela transformação martensítica, aqui CFC – HC.

Numa avaliação comparativa entre a superfície e o núcleo das amostras deformadas, verificou-se que a extensão da transformação CFC – HC foi maior na região da superfície. Esta diferença observada pode ser devida a uma menor acomodação, por parte dos grãos CFC, da tensão causada pela transformação CFC – HC na região da superfície em relação ao núcleo ou ainda por conta de diferenças heterogeneidades ao longo da amostra da tensão residual gerada no processo de manufatura aditiva.

Por conta de a transformação CFC – HC envolver falhas de empilhamento, a presença destas em grande quantidade reduz a mobilidade das discordâncias na fase CFC e aumenta a

taxa de encruamento. Portanto, na interface entre as fases  $\gamma$  e  $\epsilon$ , ocorre uma concentração de tensão. E tal concentração de tensão nucleia e propaga trincas. Desta forma, pode-se dizer que as trincas se originam na superfície do material, mais especificamente, nas interfaces CFC/HC.

O processo de transformação de fases isotérmico na amostra como produzida se mostrou bastante semelhante com o processo induzido por deformação, especialmente no que se refere ao efeito da tensão residual e da quantidade de falhas de empilhamento, que favorecem o rápido início da transformação CFC – HC. No entanto, quando não há tensão externa aplicada e o efeito da plasticidade não interfere na progressão da transformação, a amostra como produzida apresenta maior fração volumétrica final da fase HC, justamente por ter maior quantidade de sítios de nucleação que a amostra solubilizada. Esta, por sua vez, apresenta duas morfologias distintas para a fase HC, que foram atribuídas ao processo de nucleação de tal fase. Quando a fase HC é formada a partir de falhas de empilhamento, por se tratar de defeitos planares, ela apresenta morfologia lamelar. E quando nucleia em *coincident site lattices* (CSL) sua morfologia tende à equiaxial.

Pensando na aplicação de implantes da liga Co-28Cr-6Mo obtidos por manufatura aditiva, o controle microestrutural proporcionado por tratamentos térmicos pode ser fundamental para um desempenho adequado do implante. Ficou claro, no trabalho apresentado, que as propriedades mecânicas obtidas variam bastante com a alteração do balanço entre as fases CFC e HC. E, muito provavelmente, o comportamento em desgaste da liga pode ser otimizado dependendo das frações destas fases. Um tratamento termomecânico, aliado a uma etapa de acabamento, pode também atuar nesta otimização de propriedades, inclusive podendo-se induzir a nucleação de fases em regiões específicas da peça.

Por fim, o presente trabalho mostrou que a otimização dos implantes ortopédicos prevista pela introdução da manufatura aditiva pode ir além da busca pela melhor geometria para cada paciente. Aliada à um estudo de otimização topológica, a otimização microestrutural via tratamentos térmicos ou termomecânicos conferirão aos implantes do futuro um desempenho muito superior. Será possível obter níveis de resistência mecânica e ao desgaste adequados para cada aplicação e, conseqüentemente, uma melhor adequação do implante ao corpo do paciente, implicando em uma melhor qualidade de vida deste.

## 6 Conclusões

Amostras da liga Co-28Cr-6Mo foram obtidas pela técnica de manufatura aditiva L-PBF e a caracterização do material como produzido e tratado termicamente foi realizada. As análises *in-situ* da transformação de fases CFC – HC induzida por deformação e isotérmica mostraram uma íntima relação da morfologia e posição de nucleação da fase HC com a microestrutura de partida das amostras. A seguir estão as principais conclusões tiradas desta análise, presente nos Blocos 1 e 2.

- As amostras como produzidas apresentam microestrutura composta por grãos CFC alongados na direção de fabricação. Já as amostras solubilizadas apresentam microestrutura com grãos CFC equiaxiais;
- O início da transformação CFC – HC induzida por deformação ocorre mais rapidamente nas amostras como produzidas. Atribui-se a isso a maior microdeformação desta condição em comparação com a condição solubilizada;
- O tratamento térmico de solubilização levou a uma diminuição do limite de escoamento e aumento da ductilidade do material. Esta maior ductilidade pode ser explicada pela diminuição da tensão residual após o tratamento térmico e também à supressão da estricção por um mecanismo do tipo TRIP. Por conta disso, as amostras solubilizadas apresentaram maior fração volumétrica da fase HC ao final da deformação;
- Observou-se que a taxa de formação da fase HC induzida por deformação é maior na superfície do que no núcleo das amostras;
- As interfaces CFC/HC são regiões de nucleação e propagação de trincas quando o material é submetido a tensão;
- As amostras como produzidas apresentam maior cinética de transformação de fase isotérmica quando comparadas com as amostras solubilizadas. Quando a fase HC começa a nuclear, as discordâncias parciais de Shockley são consumidas e a cinética de transformação diminui. A menor densidade de discordâncias nas amostras solubilizadas aumenta o tempo de incubação e reduz a taxa de crescimento da fase HC em comparação com as amostras como produzidas;

- A fase HC apresenta diferentes morfologias dependendo da condição inicial da amostra e dos sítios de nucleação onde ela ocorre. As amostras como produzidas envelhecidas apresentam fase HC lamelar nucleando em falhas de empilhamento. Já nas amostras solubilizadas, a fase HC apresenta morfologia equiaxial nucleando em *coincident site lattices*.

## 7 Sugestões para trabalhos futuros

As ligas à base de cobalto são sabidamente resistentes ao desgaste. A maior parte dos trabalhos que correlacionam características microestruturais ao comportamento em desgaste da liga Co-28Cr-6Mo utilizam o material microfundido e não L-PBF (BALAGNA; SPRIANO; FAGA, 2012; KHAIMANEE; CHOUNGTHONG; UTHAISANGSUK, 2017; MARTINEZ-NOGUES *et al.*, 2016; PATEL *et al.*, 2012). Destes, poucos relacionam a presença da fase  $\epsilon$ -HC com o comportamento em desgaste dessa liga (CHIBA *et al.*, 2007; KOIZUMI *et al.*, 2013). Portanto, uma continuidade interessante para o presente trabalho seria uma caracterização aprofundada apresentando o efeito da fase  $\epsilon$ -HC sobre o comportamento em desgaste de peças da liga Co-28Cr-6Mo obtidas por L-PBF. Adicionalmente, um estudo do comportamento em corrosão em fluido corpóreo simulado ou ainda uma avaliação do material sob tribocorrosão seriam bastante valiosos quando pensamos na aplicação médica da liga Co-28Cr-6Mo.

## 8 Publicações

Além dos artigos contemplados nesta tese, durante o período do doutorado foram publicados outros artigos provenientes de estudos paralelos e parcerias envolvendo a liga Co-28Cr-6Mo. A seguir estão listadas todas as publicações geradas até aqui, ao longo do desenvolvimento desta tese:

BÉREŠ, M.; SILVA, C.C.; SARVEZUK, P.W.C.; WU, L.; ANTUNES, L.H.M.; JARDINI, A.L.; FEITOSA, A.L.M.; ŽILKOVÁ, J.; DE ABREU, H.F.G.; FILHO, R.M. Mechanical and phase transformation behaviour of biomedical Co-Cr-Mo alloy fabricated by direct metal laser sintering. **Materials Science and Engineering: A**, vol. 714, no. September 2017, p. 36–42, Jan. 2018

ANTUNES, L.H.M.; HOYOS, J.J.; FONSECA, E.B.; BÉREŠ, M.; DA SILVA FARINA, P.F.; LOPES, E.S.N.; JARDINI, A.L.; FILHO, R. Maciel. Effect of phase transformation on ductility of additively manufactured Co–28Cr–6Mo alloy: An in situ synchrotron X-ray diffraction study during mechanical testing. **Materials Science and Engineering: A**, vol. 764, no. August, p. 138262, 2019. DOI 10.1016/j.msea.2019.138262

IATECOLA, Amilton; LONGHITANO, Guilherme Arthur; ANTUNES, Luiz Henrique Martinez; JARDINI, André Luiz; MIGUEL, Emilio de Castro; BÉREŠ, Miloslav; LAMBERT, Carlos Salles; ANDRADE, Tiago Neves; BUCHAIM, Rogério Leone; BUCHAIM, Daniela Vieira; POMINI, Karina Torres; DIAS, Jefferson Aparecido; SPRESSÃO, Daniele Raineri Mesquita Serva; FELIX, Marcílio; CARDOSO, Guínea Brasil Camargo; DA CUNHA, Marcelo Rodrigues. Osseointegration Improvement of Co-Cr-Mo Alloy Produced by Additive Manufacturing. **Pharmaceutics**, vol. 13, no. 5, p. 724, 14 May 2021. DOI 10.3390/pharmaceutics13050724

ANTUNES, L.H.M.; HOYOS, J.J.; ANDRADE, T.C.; SARVEZUK, P.W.C.; WU, L.; ÁVILA, J.A.; OLIVEIRA, J.P.; SCHELL, N.; JARDINI, A.L.; ŽILKOVÁ, J.; DA SILVA FARINA, P.F.; ABREU, H.F.G.; BÉREŠ, M. Deformation-induced martensitic transformation in Co-28Cr-6Mo alloy produced by laser powder bed fusion: Comparison surface vs. bulk. **Additive Manufacturing**, vol. 46, no. May, p. 102100, Oct. 2021. DOI 10.1016/j.addma.2021.102100

DOLFINI ALEXANDRINO L, MARTINEZ ANTUNES LH, JARDINI MUNHOZ AL, RICOMINI FILHO AP, DA SILVA WJ. Mechanical and surface properties of Co–Cr alloy

produced by additive manufacturing for removable partial denture frameworks. **Journal of Prosthetic Dentistry** 2022:1–6. DOI <https://doi.org/10.1016/j.prosdent.2021.12.019>

ANTUNES, L. H. M., BÉREŠ, M., HOYOS, J. J., NOVOTNÝ, L., DE ABREU, H. F. G., DA SILVA FARINA, P. F. Kinetics of FCC to HCP Transformation During Aging Heat Treatment of Co–28Cr–6Mo Alloy Fabricated by Laser-Powder Bed Fusion. **Metallurgical and Materials Transactions A**, vol. 54, no. 6, p. 2329–2339, Mar 2023. DOI <https://doi.org/10.1007/s11661-023-07016-w>

CESARIN, I. S., ANTUNES, L. H. M., DARIN FILHO, G., ULSEN, C., FARINA, P. F. S. Alternative Sample Preparation of Co-28Cr-6Mo to Avoid Strain-induced Phase Transformation. **Materials Research**, vol. 26, no. 1.1, p. e20230080, 2023. DOI <https://doi.org/10.1590/1980-5373-MR-2023-0080>

COUTINHO SARAIVA, BRENO RABELO; NOVOTNÝ, LADISLAV; CARPENTIERI, BRUNO; KELLER, THOMAS FLORIAN; FÁBEROVÁ, MÁRIA; BUREŠ, RADOVAN ; RODRIGUES, SAMUEL FILGUEIRAS; RODRIGUES DE BARROS NETO, JOÃO; MARTINEZ ANTUNES, LUIZ HENRIQUE; MASOUMI, MOHAMMAD; GOMES DE ABREU, HAMILTON FERREIRA; BÉREŠ, MILOSLAV. Effect of cyclic loading on microstructure and crack propagation in additively manufactured biomaterial Co-Cr-Mo alloy. **Journal of Materials Research and Technology**, v. 26, p. 3905-3916, 2023.

## 9 Referências

As referências utilizadas na Introdução desta tese estão listadas a seguir. As demais referências, utilizadas nos artigos, estão listadas ao final destes em suas respectivas seções.

- ANDERSEN, P.J. Metals for Use in Medicine. In: DUCHEYNE, Paul (ed.). *Comprehensive Biomaterials*. [S. l.]: Elsevier, 2011. p. 5–20. <https://doi.org/10.1016/B978-0-08-055294-1.00012-X>.
- ANTUNES, L.H.M.; HOYOS, J.J.; FONSECA, E.B.; BÉREŠ, M.; DA SILVA FARINA, P.F.; LOPES, E.S.N.; JARDINI, A.L.; FILHO, R. Maciel. Effect of phase transformation on ductility of additively manufactured Co–28Cr–6Mo alloy: An in situ synchrotron X-ray diffraction study during mechanical testing. *Materials Science and Engineering: A*, vol. 764, no. August, p. 138262, 2019. DOI 10.1016/j.msea.2019.138262.
- BALAGNA, C.; SPRIANO, S.; FAGA, M. G. Characterization of Co-Cr-Mo alloys after a thermal treatment for high wear resistance. *Materials Science and Engineering C*, vol. 32, no. 7, p. 1868–1877, 2012. DOI 10.1016/j.msec.2012.05.003.
- BARUCCA, G.; SANTECCHIA, E.; MAJNI, G.; GIRARDIN, E.; BASSOLI, E.; DENTI, L.; GATTO, A.; IULIANO, L.; MOSKALEWICZ, T.; MENGUCCI, P. Structural characterization of biomedical Co–Cr–Mo components produced by direct metal laser sintering. *Materials Science and Engineering: C*, vol. 48, p. 263–269, 2015a. DOI 10.1016/j.msec.2014.12.009.
- BARUCCA, G.; SANTECCHIA, E.; MAJNI, G.; GIRARDIN, E.; BASSOLI, E.; DENTI, L.; GATTO, A.; IULIANO, L.; MOSKALEWICZ, T.; MENGUCCI, P. Structural characterization of biomedical Co–Cr–Mo components produced by direct metal laser sintering. *Materials Science and Engineering: C*, vol. 48, p. 263–269, 2015b. <https://doi.org/10.1016/j.msec.2014.12.009>.
- BÉREŠ, M.; SILVA, C.C.; SARVEZUK, P.W.C.; WU, L.; ANTUNES, L.H.M.; JARDINI, A.L.; FEITOSA, A.L.M.; ŽILKOVÁ, J.; DE ABREU, H.F.G.; FILHO, R.M. Mechanical and phase transformation behaviour of biomedical Co-Cr-Mo alloy fabricated by direct metal laser sintering. *Materials Science and Engineering: A*, vol. 714, no. September 2017, p. 36–42, Jan. 2018. DOI 10.1016/j.msea.2017.12.087.
- CHIBA, Akihiko; KUMAGAI, Kazushige; NOMURA, Naoyuki; MIYAKAWA, Satoru. Pin-

- on-disk wear behavior in a like-on-like configuration in a biological environment of high carbon cast and low carbon forged Co-29Cr-6Mo alloys. *Acta Materialia*, vol. 55, no. 4, p. 1309–1318, 2007. <https://doi.org/10.1016/j.actamat.2006.10.005>.
- DISEGI, John A.; KENNEDY, Richard L.; PILLIAR, Robert. *Cobalt-Base Alloys for Biomedical Applications*. 100 Barr Harbor Drive, PO Box C700, West Conshohocken, PA 19428-2959: ASTM International, 1999. vol. 53, . DOI 10.1520/STP1365-EB.
- EOS. Material data sheet EOS CobaltChrome MP1. Munique: [s. n.], 2011.
- GIRARDIN, E.; BARUCCA, G.; MENGUCCI, P.; FIORI, F.; BASSOLI, E.; GATTO, A.; IULIANO, L.; RUTKOWSKI, B. Biomedical Co-Cr-Mo Components Produced by Direct Metal Laser Sintering1. *Materials Today: Proceedings*, vol. 3, no. 3, p. 889–897, 2016. DOI 10.1016/j.matpr.2016.02.022.
- GURAPPA, I. Characterization of different materials for corrosion resistance under simulated body fluid conditions. *Materials Characterization*, vol. 49, no. 1, p. 73–79, 2002. [https://doi.org/10.1016/S1044-5803\(02\)00320-0](https://doi.org/10.1016/S1044-5803(02)00320-0).
- JARDINI, André Luiz; LAROSA, Maria Aparecida; MACIEL FILHO, Rubens; ZAVAGLIA, Cecília Amélia de Carvalho; BERNARDES, Luis Fernando; LAMBERT, Carlos Salles; CALDERONI, Davi Reis; KHARMANDAYAN, Paulo. Cranial reconstruction: 3D biomodel and custom-built implant created using additive manufacturing. *Journal of cranio-maxillo-facial surgery : official publication of the European Association for Cranio-Maxillo-Facial Surgery*, vol. 42, no. 8, p. 1877–84, 2014. DOI 10.1016/j.jcms.2014.07.006.
- KHAIMANEE, P.; CHOUNGTHONG, P.; UTHAISANGSUK, V. Effects of Isothermal Aging on Microstructure Evolution, Hardness and Wear Properties of Wrought Co-Cr-Mo Alloy. *Journal of Materials Engineering and Performance*, vol. 26, no. 3, p. 955–968, 6 Mar. 2017. DOI 10.1007/s11665-017-2525-x.
- KLARSTROM, D L. Wrought Cobalt-Base Superalloys. *Journal of materials engineering and performance*, vol. 2, no. August, p. 523–530, 1993. <https://doi.org/10.1007/BF02661736>.
- KOIZUMI, Yuichiro; SUZUKI, Sho; YAMANAKA, Kenta; LEE, Byoung-soo; SATO, Kazuhisa; LI, Yunping; KUROSU, Shingo; MATSUMOTO, Hiroaki; CHIBA, Akihiko. Strain-induced martensitic transformation near twin boundaries in a biomedical Co–Cr–Mo alloy with negative stacking fault energy. *Acta Materialia*, vol. 61, no. 5, p. 1648–1661, Mar. 2013. DOI 10.1016/j.actamat.2012.11.041.
- LIVERANI, E.; FORTUNATO, A.; LEARDINI, A.; BELVEDERE, C.; SIEGLER, S.;

- CESCHINI, L.; ASCARI, A. Fabrication of Co–Cr–Mo endoprosthetic ankle devices by means of Selective Laser Melting (SLM). *Materials & Design*, vol. 106, p. 60–68, 2016. DOI 10.1016/j.matdes.2016.05.083.
- MARTINEZ-NOGUES, V.; NESBITT, J. M.; WOOD, R. J K; COOK, R. B. Nano-scale wear characterization of CoCrMo biomedical alloys. *Tribology International*, vol. 93, p. 563–572, 2016. DOI 10.1016/j.triboint.2015.03.037.
- MENGUCCI, P.; BARUCCA, G.; GATTO, A.; BASSOLI, E.; DENTI, L.; FIORI, F.; GIRARDIN, E.; BASTIANONI, P.; RUTKOWSKI, B.; CZYRSKA-FILEMONOWICZ, A. Effects of thermal treatments on microstructure and mechanical properties of a Co-Cr-Mo-W biomedical alloy produced by laser sintering. *Journal of the Mechanical Behavior of Biomedical Materials*, vol. 60, p. 106–117, 2016. DOI 10.1016/j.jmbbm.2015.12.045.
- PATEL, Bhairav; FAVARO, Gregory; INAM, Fawad; REECE, Michael J.; ANGADJI, Arash; BONFIELD, William; HUANG, Jie; EDIRISINGHE, Mohan. Cobalt-based orthopaedic alloys: Relationship between forming route, microstructure and tribological performance. *Materials Science and Engineering C*, vol. 32, no. 5, p. 1222–1229, 2012. <https://doi.org/10.1016/j.msec.2012.03.012>.
- SALDÍVAR GARCÍA, A. D.J.; MANÍ MEDRANO, A.; SALINAS RODRÍGUEZ, A.; DE J. SALDÍVAR GARCÍA, A; MANÍ MEDRANO, A; SALINAS RODRÍGUEZ, A. Effect of solution treatments on the FCC/HCP isothermal martensitic transformation in Co-27Cr-5Mo-0.05C aged at 800°C. *Scripta Materialia*, vol. 40, no. 6, p. 717–722, Feb. 1999. DOI 10.1016/S1359-6462(98)00489-8.
- TAKAICHI, Atsushi; SUYALATU; NAKAMOTO, Takayuki; JOKO, Natsuka; NOMURA, Naoyuki; TSUTSUMI, Yusuke; MIGITA, Satoshi; DOI, Hisashi; KUROSU, Shingo; CHIBA, Akihiko; WAKABAYASHI, Noriyuki; IGARASHI, Yoshimasa; HANAWA, Takao. Microstructures and mechanical properties of Co-29Cr-6Mo alloy fabricated by selective laser melting process for dental applications. *Journal of the Mechanical Behavior of Biomedical Materials*, vol. 21, p. 67–76, 2013. DOI 10.1016/j.jmbbm.2013.01.021.